

Measurement of atmospheric carbon dioxide abundance on board unmanned aircraft – challenges and applications

Dissertation

zur Erlangung des akademischen Grades doctor rerum naturalium

(Dr. rer. nat.)

vorgelegt dem Rat der Chemisch-Geowissenschaftlichen Fakultät der
Friedrich-Schiller-Universität Jena

von M.Sc. Martin Kunz

geboren am 28.02.1987 in Jena

Gutachter:

1. Prof. Dr. Wolfgang Weigand, Friedrich-Schiller-Universität Jena
2. Dr. habil. Christoph Gerbig, Max-Planck-Institut für Biogeochemie, Jena

Tag der Verteidigung: 23. Oktober 2019

Dedicated to Hans-Günther

Abstract

Quantifying and understanding the global carbon cycle is essential for the analysis and prediction of climate change. Observations of greenhouse gases in the atmosphere of the Earth have come a long way since Dave Keeling started the first continuous measurements of carbon dioxide (CO₂) on Mauna Loa, Hawaii, in 1958. Nevertheless, our picture of the global carbon cycle is far from complete. One observational gap lies between the measurements taken at surface stations and those carried out on manned aircraft. A versatile and cost-effective tool that could fill this gap is presented by small unmanned aircraft systems (UASs) or “drones”. However, the lack of small and light, yet accurate gas analysers has prevented practical realisation of this idea in the past.

In this dissertation the COmpact Carbon dioxide analyser for Airborne Platforms (COCAP) is presented. COCAP measures the abundance of carbon dioxide in ambient air as well as air temperature, humidity and pressure, and is specifically designed for the use on board small UASs. Accurate CO₂ measurements are ensured by extensive calibration in an environmental chamber, by regular calibration in the field and by chemical drying of sampled air. In addition, the analyser is equipped with a custom-built, lightweight thermal stabilisation system that reduces the influence of ambient temperature changes on the CO₂ sensor by two orders of magnitude. The robustness of COCAP under varying environmental conditions has been verified through a series of tests both in the lab and in the field.

As a first application of the newly developed instrument, COCAP was used to constrain the nocturnal carbon dioxide emission of an ecosystem based on the nocturnal boundary layer (NBL) budget method. The NBL budgets were calculated from a series of CO₂ profiles measured by COCAP on board a UAS during the course of two nights. The fluxes obtained in the pilot study are plausible and insensitive to experimental uncertainties. Given the versatility and moderate cost of UASs and their minimal infrastructure requirements, this innovative sampling technique makes the NBL budget method for the quantification of surface fluxes more accessible and cost-effective.

This work demonstrates how the potential of UASs for measuring trace gases in the atmosphere can be exploited, thus opening up new possibilities for atmospheric research.

Zusammenfassung

Die Quantifizierung und das Verständnis des globalen Kohlenstoffkreislaufs sind entscheidend für die Analyse und Vorhersage des Klimawandels. Die Beobachtung von Treibhausgasen in der Erdatmosphäre hat sich stetig weiter entwickelt, seit Dave Keeling 1958 die erste kontinuierliche Messung von Kohlenstoffdioxid (CO₂) auf dem Mauna Loa in Hawaii etablierte. Dennoch ist unser Bild vom globalen Kohlenstoffkreislauf noch längst nicht vollständig. Es klafft eine Beobachtungslücke zwischen den Daten von Messstationen am Erdboden und jenen, die mithilfe von bemannten Forschungsflugzeugen gesammelt werden. Ein vielseitiges und kostengünstiges Werkzeug, das diese Lücke füllen könnte, sind unbemannte Luftfahrtsysteme ("Drohnen"). In Ermangelung kleiner, leichter und dennoch genauer Gasanalysatoren konnte diese Idee in der Vergangenheit allerdings nicht realisiert werden.

In dieser Dissertation wird ein kompakter Kohlendioxidanalysator für Flugsysteme (COmpact Carbon dioxide analyser for Airborne Platforms, COCAP) vorgestellt. COCAP misst den Kohlendioxidanteil, die Temperatur, die Feuchte und den Druck der Umgebungsluft und ist speziell für den Einsatz auf kleinen unbemannten Luftfahrtsystemen ausgelegt. Genaue Kohlendioxidmessungen werden durch umfangreiche Kalibrierungen in einer Klimakammer, regelmäßige Kalibrierungen während des Feld-einsatzes und durch chemische Trocknung der Probenluft sichergestellt. Darüber hinaus enthält das Messsystem einen speziell entwickelten Temperaturregler mit geringer Masse, der den störenden Einfluss äußerer Temperaturänderungen auf den CO₂-Sensor um zwei Größenordnungen verringert. COCAPs Robustheit gegenüber wechselnden Umgebungsbedingungen wurde in einer Reihe von Tests im Labor und im Feld nachgewiesen.

COCAPs erster wissenschaftliche Einsatz diente der Abschätzung nächtlicher Kohlendioxidflüsse mithilfe von Budgets der nächtlichen Grenzschicht (nocturnal boundary layer, NBL). Diese NBL-Budgets wurden aus CO₂-Profilen errechnet, welche COCAP während einer Reihe von Flügen mit einem unbemannten Luftfahrtsystem im Verlauf zweier Nächte aufzeichnete. Die in dieser Pilotstudie ermittelten Flüsse sind plausibel und robust gegenüber experimentellen Unsicherheiten. Angesichts der Vielseitigkeit und der moderaten Kosten unbemannter Luftfahrtsysteme sowie ihrer minimalen Ansprüche an die Infrastruktur im Feld eröffnet diese innovative Messstrategie eine vergleichsweise einfache und günstige Möglichkeit, Flüsse durch NBL-Budgets zu bestimmen.

Diese Arbeit zeigt auf, wie das Potenzial unbemannter Luftfahrtsysteme für Spurengasmessungen genutzt werden kann, wodurch sich neue Perspektiven für die Atmosphärenforschung ergeben.

Contents

List of Figures	ix
List of Tables	xi
List of Abbreviations	xiii
List of Symbols	xv
Foreword	xvii
1 Introduction	1
1.1 The global carbon cycle	1
1.2 The greenhouse effect	3
1.3 Observation of the carbon cycle	5
1.4 Unmanned aircraft systems	7
1.5 Aim and structure of this work	7
2 A compact carbon dioxide analyser for airborne platforms	9
2.1 Literature review	9
2.2 COCAP	10
2.2.1 System overview	10
2.2.2 Carbon dioxide sensor	11
2.2.3 Other components in the gas sampling line	13
2.2.4 Ambient sensors	14
2.2.5 Data logger	14
2.2.6 Temperature stabilisation	16
2.2.7 Battery	22
2.3 Field calibration device	22
2.4 Unmanned aircraft	22
2.4.1 Requirements of COCAP	22
2.4.2 Multicopters	24
2.4.3 Fixed-wing aircraft	24
2.4.4 Other platforms	24
2.5 Cost estimation	26

Contents

2.6	Calibration	26
2.6.1	Calibration curve of the CO ₂ sensor	26
2.6.2	Calibration of ambient sensors	30
2.6.3	Field calibration	32
2.7	Summary of Chapter 2	33
3	Tests and validation	35
3.1	Overview	35
3.2	Measurements with an instrumented van	36
3.2.1	Experimental setup	36
3.2.2	Compensating for different flushing time of two analysers	37
3.2.3	Results and discussion	39
3.3	Simulated flights	39
3.3.1	Experimental setup	39
3.3.2	Results and discussion	42
3.4	Lannemezan flights	44
3.5	Allan deviation of CO ₂ dry air mole fraction	44
3.6	Comparison to the ICOS station Lindenberg	47
3.6.1	Measurement site and flight pattern	47
3.6.2	Results and discussion	48
3.7	Summary of Chapter 3	52
4	Using COCAP to estimate nocturnal fluxes	53
4.1	Nocturnal boundary layer budgets	53
4.2	Site and instrumentation	55
4.2.1	Fendt site	55
4.2.2	Ground-based instrumentation	56
4.2.3	Airborne payload	57
4.2.4	Unmanned aircraft	58
4.3	Methods	58
4.3.1	Disturbance by the UAS	58
4.3.2	Correction for response time of sensors	59
4.3.3	Calculation of the NBL budget	62
4.3.4	Footprint calculation	64
4.4	Results and discussion	66
4.4.1	Uncertainty of x_{CO_2} measurements	66
4.4.2	Meteorological conditions	67
4.4.3	Profiles	67
4.4.4	Disturbance by the UAS	73

Contents

4.4.5	Carbon dioxide fluxes	76
4.4.6	Sensitivity of fluxes	82
4.4.7	Flux footprint	85
4.5	Summary of Chapter 4	86
5	Conclusions and outlook	89
	Bibliography	93
	Selbstständigkeitserklärung	105

List of Figures

1.1	Schematic view of the global carbon cycle	2
1.2	Abundance of CO ₂ and CH ₄ over the past 2 000 years	4
2.1	Flow of air, electrical power and data inside COCAP	10
2.2	COCAP's carbon dioxide sensor	11
2.3	Cartridges for drying agent	12
2.4	Sensor board for measuring pressure in the gas line	14
2.5	Detail of the outlet temperature sensor	15
2.6	PCB for measuring temperature and relative humidity	16
2.7	Temperature stabilisation of COCAP	18
2.8	Fan and heating element for temperature stabilisation	19
2.9	Internal temperature sensor	20
2.10	Temperature control board, front side	21
2.11	Temperature control board, back side	21
2.12	Field calibration device	23
2.13	COCAP mounted under a custom-built multicopter	25
2.14	Ambient conditions during calibration	28
2.15	Setup used to determine a calibration curve	29
2.16	Raw and corrected signal of COCAP's CO ₂ sensor	31
3.1	Observed signals during a car drive	40
3.2	Stability test in an environmental chamber	41
3.3	Temperatures during simulated flight	43
3.4	Stability of COCAP's internal temperatures during flight	45
3.5	Allan deviation during simulated flight	46
3.6	Comparison between COCAP and LIN (time series)	49
3.7	Comparison between COCAP and LIN (averages)	50
4.1	Location of the Fendt site	56
4.2	COCAP carried by a multicopter during ScaleX 2016	57
4.3	Response of COCAP to a step change in x_{CO_2}	61
4.4	Allan deviation in the field	66
4.5	Meteorological conditions during NBL soundings	68

List of Figures

4.6	Profiles from flights 4–10	70
4.7	Profiles from flights 19–23	71
4.8	Comparison of measurements by COCAP, HPB and 9 m mast	72
4.9	Disturbance at different ground speeds	75
4.10	Comparison of fluxes from NBL budget and EC method	79
4.11	Comparison of fluxes from NBL budget and chambers	80
4.12	Sensitivity of flux to changes in calculation procedure	84
4.13	Footprint of an NBL budget on 6 July	85
4.14	Footprint of an NBL budget on 9 July	86

List of Tables

2.1	Calibration of ambient sensors	30
3.1	Temperatures during simulated flight	43
3.2	Mean difference between COCAP and LIN	51
3.3	Statistical tests for bias	51
4.1	Fluxes calculated from NBL budgets	77
4.2	Nighttime fluxes observed in other studies	81
4.3	Sensitivity of calculated fluxes	83

List of Abbreviations

Chap.	chapter
COCAP	COmpact Carbon dioxide analyser for Airborne Platforms
EC	eddy covariance
ECMWF IFS	European Centre for Medium-Range Weather Forecasts Integrated Forecast System
Fig.	figure
FWHM	full width at half maximum
GAW	Global Atmosphere Watch
GPS	Global Positioning System
HPB	ICOS station Hohenpeißenberg
HYSPLIT	Hybrid Single-Particle Lagrangian Integrated Trajectory model
ICOS	Integrated Carbon Observation System
LIN	ICOS station Lindenberg
NBL	nocturnal boundary layer
NEE	net ecosystem exchange
PCB	printed circuit board
Sect.	section
STILT	Stochastic Time-Inverted Lagrangian Transport model
UAS	unmanned aircraft system
WMO	World Meteorological Organization

List of Symbols

δ	Dirac delta function
σ	Allan deviation
τ	period of time or time constant
a	parameter in a model
b	constant representing sensor offset
c	concentration (amount per volume)
d	standard deviation
e	Euler's number, $e \approx 2.718$
E	strength of a volume source or sink (amount per volume and time)
$f(t)$	instrument function of a measurement device
$F(\dots)$	footprint of a measurement
$k(\dots)$	calibration curve of a measurement device
l_1, l_2	coordinates defining a geographic location
l_{G1}, l_{G2}	indices of a grid cell in the STILT model
p	pressure
R	ideal gas constant, $R = 8.314 \text{ J} \cdot \text{mol}^{-1} \cdot \text{K}^{-1}$
s	raw signal of COCAP's infrared gas sensor
S	net ecosystem exchange
\bar{S}	net ecosystem exchange averaged over the period $t_F - t_0$
t	time
t_0	time when the surface radiation balance becomes negative
t_F	time of a flight
T	temperature
\vec{u}	wind vector
u	eastward component of wind vector
U	relative humidity
v	northward component of wind vector
w	upward component of wind vector
x	dry air mole fraction
Δy	difference between two consecutive arithmetic means of measurements
z	height, i.e. vertical distance from ground

Foreword

This dissertation is the result of my work at the Max Planck Institute for Biogeochemistry in Jena between 2012 and 2019. My main goal throughout this period of time was to enable the accurate measurement of CO₂ content in the atmosphere using small unmanned aircraft. The most important considerations, experimental results and conclusions from this project are presented in the following chapters.

During writing I had to make the fundamental choice of how to report on my work: (1) exclusively in the passive voice, (2) using the active voice in the singular form “I” or (3) using the active voice in the plural for “we”. I was determined not to restrict my writing to the passive voice for two reasons. Firstly, the passive voice makes any longer text dull and unpleasant to read – and this text is a really long one. Secondly, the objectivity that many attribute to the passive voice is in my eyes quite often abused. Constructs like “the analysis was carried out” might imply that the analysis was a completely objective process, but if a human did it, it certainly was not. Instead of creating the appearance of objectivity through grammatical tricks, I aim to convince the reader of the fidelity of my work by precisely describing what I did and by explicitly stating any data selection.

This left me with the choice between “I” and “we”. Certainly I had a major part in the design and building of our analyser’s custom-made parts detailed in Chapter 2, in designing and carrying out both the validation experiments described in Chapter 3 and the pilot study covered in Chapter 4. I prepared most of the data presented, produced the figures and interpreted the results. However, none of these I could have done without the practical help, important ideas or moral support of others. I feel that reporting in the singular form would not do their contributions justice. “My results” conveys the message that all the work was carried out by a single person. In contrast, “our results” indicates that several people contributed, without stating that the quantity of contribution was necessarily equal. The plural form most faithfully captures how the results presented here were obtained, and therefore I decided to use the plural pronouns throughout this dissertation. Excluding the Foreword, as the reader may have noticed.

Large parts of the work presented here relied on Free and Open Source Software (FOSS), i.e. software that anyone can freely use, copy, study and modify and that is available not only in binary form, but also as source code. The long list of FOSS projects I am indebted to includes (in alphabetic order) ArduPilot, Bib_TE_X, GIMP, GNU/Linux, GNU Octave, gnuplot, Inkscape, KiCad, L^AT_EX, LyX, Mozilla Firefox, Mozilla Thunder-

Foreword

bird, Paparazzi UAV, QGIS and Zotero. The colours in diagrams and maps are based on the work of Cynthia A. Brewer (Brewer, 2017), Peter Kovesi (Kovesi, 2015) and on the Wikicarto 2.0 colour map (Wikipedia contributors, 2012).

The world wide web is full of valuable resources, and during my PhD I have taken advantage of a good number of them. However, would I be denied access to all websites but one that I could pick, my choice would be clear: the free encyclopedia Wikipedia. Countless times Wikipedia has provided me with a concise overview of a new topic, with a clear definition for a concept I had only a fuzzy idea of, or with a helpful clarification of a set of linked terms that were used seemingly randomly in literature. Nothing is perfect, but the selection and quality of information on Wikipedia surprisingly often comes close. And just in case I am totally without internet access, I carry an offline version of Wikipedia on the smartphone in my pocket.

First of all I thank Jošt Lavrič, my main supervisor. He supported me and my PhD project with knowledge, ideas and with the funds I needed to buy equipment and to finance trips to international conferences. Jošt's courage to take risks when justified by the potential benefits inspired me. I am grateful for the large freedom he gave me in pursuing my project, allowing me to unleash my creativity and to do things (what I thought was) right instead of quick and dirty. The possibility to follow my own ideas with very few limits was a strong source of motivation and satisfaction. With his friendly attitude and good humour it was always a pleasure to work in Jošt's group.

Invaluable support for my PhD project was provided by my three co-supervisors. I thank Christoph Gerbig for always being open for discussion of questions or ideas, for generously sharing his extensive knowledge about trace gas measurements, atmospheric transport and meteorology and for his motivating appreciation of my work. I am indebted to Pieter Tans for openly sharing his enthusiasm for my project and his recognition, for his thoughtful comments and for hosting me at the NOAA Earth System Research Laboratory for two months in 2015. The time in Boulder has definitely been one of the highlights of my PhD and Pieter's generous support had a large part in that. I offer my gratitude to Prof. Wolfgang Weigand for his interest in my project and his important hints on the promotion process at the Friedrich Schiller University Jena. Special thanks are due to Christoph and Prof. Wolfgang Weigand for reviewing the proposal that gained me a stipend for my research stay in Boulder.

During my PhD I benefited from several lucky coincidences. Of those, meeting Henrik Rödjegård of SenseAir at a workshop of the COST action TD1105 was probably the most important one. Following Henrik's presentation of a new gas sensor prototype in 2013, a very fruitful collaboration developed between the MPI for Biogeochemistry in Jena and SenseAir. I thank Hans Martin for inviting me to Delsbo, Sweden, for a one month research stay. I owe my deepest gratitude to Maksym Bryzgalov, who granted me deep insight into the HPP family of gas sensors, was full of good advice and made my

time at SenseAir most enjoyable. I extend my appreciation to Christine Hummelgård, Ingrid Bryntse, Erik Wilhemsson, Jan Wigg and Jan-Åke Henning for scientific input, technical support and for providing me with the sensors and accessories I needed for the development of COCAP. Thanks to all the staff at SenseAir for the warmth and friendliness they showed me during my stay.

I acknowledge Høk Instruments AB (Sweden) for kindly providing software for COCAP's data logger.

I thank Hartmut Müller, chairman of the Jena aeromodelling club, for teaching me how to fly remotely controlled aircraft and for supporting our project

I am indebted to Jens Dünnermann and Burkhard Wrenger for providing their multi-copters and piloting skills during several flight campaigns. Special thanks to Burkhard for a memorable van drive to the Centre de Recherche Atmospheriques in Lannemezan near Toulouse and back.

My research stay in Boulder was highly productive, insightful and enjoyable due to the kind support I received from the staff at NOAA. I am particularly grateful to Don Neff, who spent hours driving COCAP and me up and down mountains, to Stephen Conley, Gabrielle Pétron and Stefan Schwietzke for stimulating discussions of airborne measurements and for giving COCAP a ride on a manned aircraft. Thanks to Anne Thorne for valuable assistance in the organisational aspects of my stay and to Ed Dlugokencky for a camping stove and pot that served me very well during a one week road trip at the end of my visit to the US.

Special thanks are due to Richard Grant for providing his multicopter for the flights during the ScaleX 2016 campaign, as well as to Evan Flatt for piloting it. In addition I thank Richard for help in the data analysis and interpretation. The ScaleX 2016 campaign at the TERENO site Fendt was only possible thanks to the staff of the KIT IMK-IFU in Garmisch-Partenkirchen, who went through large efforts by organising a campaign with more than 60 participants. In particular I acknowledge Matthias Zeeman, who did an amazing job as coordinator of ScaleX 2016 and who also helped me a lot by sharing his data and discussing our results. I am thankful to Klaus Schäfer for making me aware of the ScaleX campaign, for coordinating work package 2 and for providing us with magnesium perchlorate when I had forgotten ours in Jena. I thank Rainer Gasche and Benjamin Wolf for sharing and discussion of data. Special thanks to Andreas Philipp for lending us his fixed-wing UAS and teaching me how to fly it. I thank Andreas Angerer, Claire Brenner, Caroline Brosy and all the other ScaleX participants for making the campaign and the associated workshops a fruitful and fun experience. The TERrestrial Environmental Observatory (TERENO) pre-Alpine infrastructure is funded by the Helmholtz Association and the Federal Ministry of Education and Research.

Foreword

I thank Frank Beyrich, Matthias Lindauer, Udo Rummel and Marcus Schumacher of the German Weather Service (DWD) for access to the ICOS station Lindenberg, technical support and data sharing.

This work has been enabled by generous financial support from the Max Planck Society. I acknowledge COST (European cooperation in science and technology) and the German Academic Exchange Service (DAAD) for funding my stays at SenseAir and NOAA, respectively.

I am grateful for the manifold support I received at the MPI for Biogeochemistry Jena. Thanks to Martin Heimann, who has fostered the idea of utilising unmanned aircraft for atmospheric research for years, contributed valuable ideas and provided the funds for the project. I thank Bernd Schlöffel, Reimo Leppert, Harald Schmalwasser, Martin Strube and Frank Voigt for their various contributions to COCAP. To Wieland Jeschag and Till Fastnacht I am indebted for adapting and extending the firmware of COCAP's data logger. I gratefully acknowledge Jürgen Kaulfuß for designing and building the field calibration device. I thank the staff of the gas lab for preparing the gas standards we used for calibration in the lab and in the field. I greatly appreciated the help of Field Experiments and Instrumentation group, from whom I borrowed on several occasions equipment that made my work in the field much easier. I thank Julia Marshall for providing free English language consultancy a number of times. A big thank you is due to Ulrike Schleier for relieving me of administrative and organisational burdens, especially in connection with business trips, and for making the workaday life in our department so comfortable. I thank Anna Görner and Steffi Rothhardt for their help in navigating through my PhD project and for engaging top-notch speakers for the many brilliant courses that I had the privilege to attend. Frank-Thomas Koch made an important contribution to my project by running the STILT model for Fendt, which I gratefully acknowledge. To Fanny Kittler I am thankful for illuminating discussions about the EC method. Thanks Nora Adam, Fabio Boschetti, Sven Böse, Chirag Dhara, Thomas Fabisch, Annette Filges, Iulia Ilie, Min Jung Kwon, Talie Musavi, Sandra Raab, Tea Thum and all my other fellow PhD students for making my PhD time so much more fun and colourful. I extend my special thanks to all my colleagues who make the institute a warm and welcoming place.

I thank Philipp Lucas and Paul Roßmann for being great friends and for proofreading the manuscript of this thesis. Their comments certainly made this dissertation better.

I acknowledge R (Chandra) Chandrasekhar, who wrote "How to Write a Thesis: A Working Guide" (Chandrasekhar, 2008). I found this guide extremely helpful during the writing of this dissertation (even though I respectfully disagree with the advice to use the singular pronoun "I").

I thank my parents for their love and care, for fostering my curiosity and my interest in science and technology and for always believing in me.

The year 2017 brought an ordeal that I had hoped to never go through and I do not know what I would have done without the sympathy and support I received from my family, friends and colleagues. I am deeply grateful for their help.

To my mind, the last position in a thesis acknowledgement is the most prominent one. I reserve it for my wife Ina, who contributed to this work in many different ways. She was always open for discussion about my work, giving me opportunities to reflect on my lines of thought and providing me with valuable ideas. She proofread the manuscript of this thesis and helped me to make it clearer and more consistent. Without pushing, she constantly encouraged and supported me in going through the final (and arguably hardest) phase of my PhD project. Thank you, Ina, for your love and affection, which are an irreplaceable source of energy for me.

Foreword

This work is also reflected in two scientific articles:

- Kunz, M., Lavric, J. V., Gerbig, C., Tans, P., Neff, D., Hummelgård, C., Martin, H., Rödjegård, H., Wrenger, B., and Heimann, M.: COCAP: A Carbon Dioxide Analyser for Small Unmanned Aircraft Systems, *Atmos. Meas. Tech.*, 11, 1833–1849, doi:10.5194/amt-11-1833-2018, 2018.
- Kunz, M., Lavric, J. V., Gasche, R., Gerbig, C., Grant, R. H., Koch, F.-T., Schumacher, M., Wolf, B. and Zeeman, M.: Surface flux estimates derived from UAS-based mole fraction measurements by means of a nocturnal boundary layer budget approach, *Atmospheric Measurement Techniques Discussions*, 1–35, doi:10.5194/amt-2019-221, 2019.

1 Introduction

1.1 The global carbon cycle

Carbon is a central building block of life. All organisms have to exchange carbon with their environment in order to grow. This exchange takes place in the form of different carbon compounds, such as carbohydrates that are ingested by humans and other animals, carbon dioxide (CO_2) that is exhaled by animals and taken up by plants, or methane (CH_4) that is produced and consumed by microbes. In many cases, carbon runs through a chain of compounds that forms a closed cycle, i.e. carbon is recycled in the Earth system. A typical example of this recycling is the interplay between photosynthesis and cellular respiration: Plants convert CO_2 into carbohydrates, while animals or fungi convert these carbohydrates back into CO_2 . As many carbon compounds are transported over long distances, e.g. by the wind or by running water, the flow of carbon takes place on a global scale. The transport, conversion and storage of all carbon on Earth is called the global carbon cycle.

Organisms are neither the only nor the biggest players in the carbon cycle. The oceans, soil and rocks, the Earth's fossil fuel reserves and the atmosphere contain large amounts of carbon (Figure 1.1). The distribution and exchange of carbon between these reservoirs remained widely unchanged over thousands of years before the Industrial Revolution (Joos and Spahni, 2008). However, since the beginning of the industrial era we humans have been altering the global carbon cycle. On the one hand, we are extracting fossil fuel from geological reservoirs and burn it, effectively transporting carbon from the ground into the atmosphere. On the other hand, the fast growth of the human population since 1700 entailed the conversion of more and more parts of the landmass to arable land, mainly by deforestation. This ongoing land use change is transporting carbon from the biosphere into the atmosphere. It was only in the last 50 years that mankind realised which consequences this change of the carbon cycle may yield.

The atmospheric part of the carbon cycle is dominated by CO_2 , a colourless and in low concentrations odourless gas. Roughly 4 out of 10 000 molecules or $400 \mu\text{mol}\cdot\text{mol}^{-1}$ of the Earth's atmosphere are CO_2 molecules. The main sources of CO_2 are cellular respiration (e.g. by animals and fungi), burning of biomass or fossil fuels and cement production. Its main sinks are photosynthesis and, in the current state of the Earth system, dissolution in the oceans.

1 Introduction

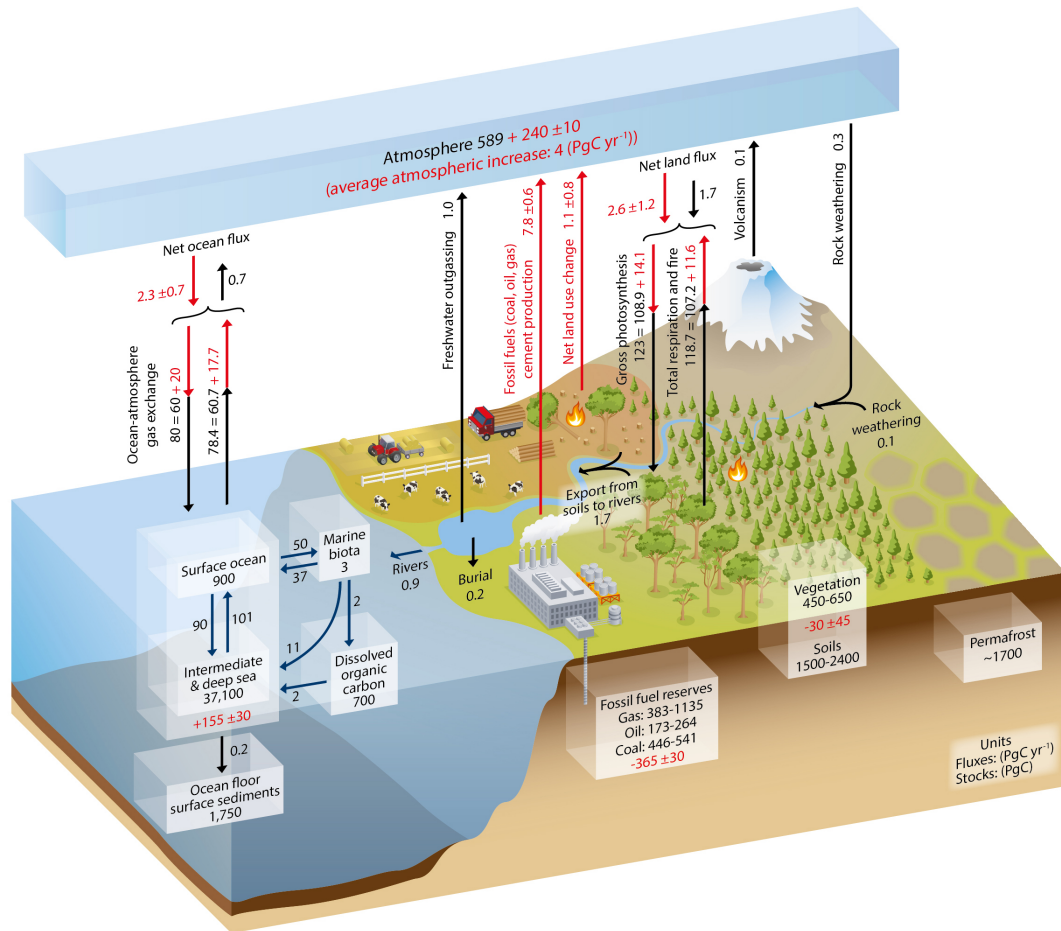


Figure 1.1: Schematic view of the global carbon cycle. Numbers in boxes indicate carbon stocks in Pg (10^{15} g), numbers on arrows indicate carbon fluxes in $\text{Pg} \cdot \text{yr}^{-1}$. Elements in black represent the state until the year 1750, elements in red the changes since then. Authorised reproduction from (Ciais et al., 2013, p. 471)

1.2 The greenhouse effect

Carbon dioxide is important for life on Earth not only as a nutrient or metabolite of organisms, but also due to its influence on the climate. It is a so called greenhouse gas. In the atmosphere, greenhouse gases absorb infrared radiation that is emitted by the Earth's surface and would otherwise be radiated into space. The atmosphere heats up and emits more infrared radiation towards the ground than without the absorption. This is known as the greenhouse effect and leads to a warming of the Earth.

The strength of the greenhouse effect is commonly quantified using the concept of radiative forcing, which is the change in the Earth's energy balance expressed as a change in energy flux density (Myhre et al., 2013, p. 664). The globally averaged CO₂ dry air mole fraction in the atmosphere has increased by 276–280 μmol·mol⁻¹ between 1750 and 2011, causing a radiative forcing of 1.63–2.01 W·m⁻² (Myhre et al., 2013, p. 676). During the same period, the fraction of CH₄ has risen as well. CH₄ is the second most abundant carbon compound in the atmosphere and a potent greenhouse gas. The globally averaged CH₄ dry air mole fraction has increased by 1056–1106 nmol·mol⁻¹ between 1750 and 2011, causing a radiative forcing of 0.43–0.53 W·m⁻² (Myhre et al., 2013, p. 677). The rise of atmospheric CO₂ and CH₄ abundance since 1750 is in stark contrast to their relatively stable preindustrial levels, as can be seen in Figure 1.2.

The radiation from the sun is a permanent heat source for the Earth. The incoming energy flux density at the top of the Earth's atmosphere is approximately 1360 W·m⁻² (Kopp and Lean, 2011). Considering the Earth's nearly spherical shape, the average received radiative power per surface area is 340 W·m⁻². Hence, the increase in atmospheric abundance of CO₂ and CH₄ between 1750 and 2011 affects the Earth's energy budget as much as would an increase in solar irradiance by 5.3 ‰ and 1.4 ‰, respectively. This change might seem negligibly small.

However, even small changes in the radiation balance of the Earth can lead to dramatic effects for the biosphere. One well-documented example of this sensitivity was the year 1816, called the "Year without summer". The eruption of Tambora volcano in Indonesia in April 1815 transported 10–100 Tg of sulphur into the stratosphere (Oppenheimer, 2003), which affected the weather around the globe during the following years. In 1816, the mean surface temperature in the northern hemisphere exhibited an anomaly of -0.5 °C (Briffa et al., 1998), which resulted in crop failures in Europe and large parts of North America. As a consequence, in the years 1816–1817 the Western world was hit by the worst famine in more than a century (Oppenheimer, 2003).

Recent temperature changes have been slower. Between 1951 and 2012, the combined land and ocean surface temperatures have increased by 0.49–0.59 °C (Hartmann et al., 2013, p. 162). Nevertheless, if the abundance of greenhouse gases continues to increase at the current rate, the global average temperature may rise to more than 2 °C above

1 Introduction

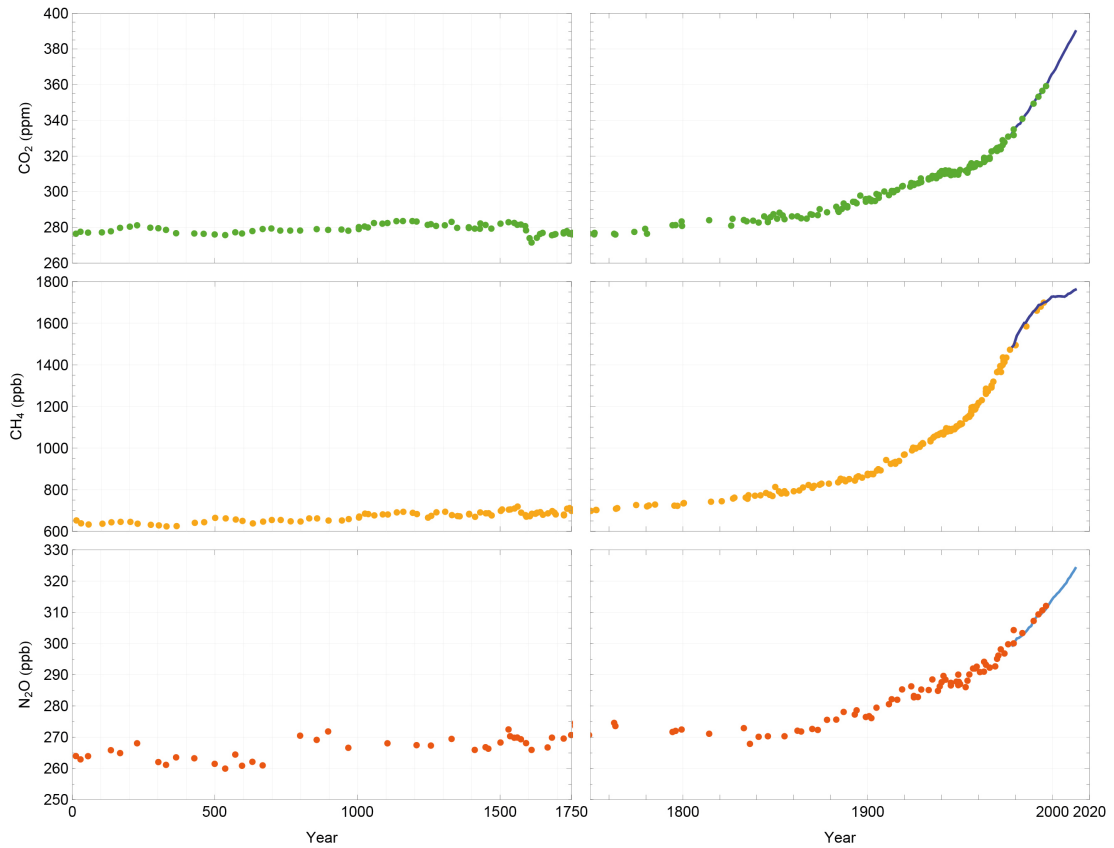


Figure 1.2: Evolution of CO₂, CH₄ and N₂O dry air mole fraction over the past 2000 years, determined from ice cores and firn (dots) and atmospheric measurements (lines). Note the different scaling of the time axis in the right panels. The pronounced increase in abundance of CO₂ and CH₄ since the 19th century illustrates the influence of the industrial revolution on the global carbon cycle. Units: 1 ppm (part per million) = 1 $\mu\text{mol}\cdot\text{mol}^{-1}$, 1 ppb (part per billion) = 1 $\text{nmol}\cdot\text{mol}^{-1}$. Authorised reproduction from (Ciais et al., 2013, p. 493)

1.3 Observation of the carbon cycle

the second half of the 19th century by the year 2100 (Collins et al., 2013, p. 1055) . This warming entails melting of ice sheets and glaciers worldwide, which will – together with thermal expansion of the oceans – result in a sea level rise by 32–63 cm compared to the period from 1986–2005 (IPCC, 2013, p. 25). Among the projected consequences of global warming are a higher frequency of extreme heat events (Collins et al., 2013, p. 1065), changes in precipitation patterns (Collins et al., 2013, pp. 1076) and weakening of the Atlantic Meridional Overturning Circulation including the Gulf stream (Kirtman et al., 2013, p. 994). Many of these changes are already being observed.

All these changes in the Earth system have immediate consequences for mankind. Rising sea levels pose an increased risk of flooding to people living near the coasts. Extreme heat events lead to crop loss and mortality due to hyperthermia. While changes in precipitation patterns can have positive or negative effects for a region, studies on crop yield suggest a dominantly negative impact (IPCC, 2014, pp. 4).

It is worth noting that the strongest greenhouse effect in the atmosphere is caused by water vapour, owing to its high abundance (Myhre et al., 2013, p. 666). However, water behaves differently than CO₂ and CH₄ in the atmosphere because of its physical properties: it can evaporate and precipitate within the temperature range of the troposphere and the Earth's surface. Under rising surface temperature more water evaporates, leading to an increase in atmospheric water vapour mole fraction and hence a stronger radiative forcing. On the other hand, under decreasing surface temperatures water precipitates, lowering the atmospheric water vapour mole fraction and consequently reducing radiative forcing. The abundance of water vapour is mainly driven by temperature, not by emissions. Therefore, water vapour exerts an amplifying feedback on climatic shifts, but is not an initial cause of changes.

Global warming is a reality mankind has to cope with. Policy makers are seeking ways to mitigate global warming and to adapt to those changes that cannot be avoided. Effective mitigation and adaptation both require precise predictions of the development of the Earth system under different scenarios, because the outcome and side effects of possible actions must be evaluated. Such predictions can only be made if all major components of the Earth system are well understood. As CO₂ and CH₄ are the main drivers of global warming (Myhre et al., 2013, pp. 666–667), the carbon cycle is of particular importance for these predictions.

1.3 Observation of the carbon cycle

Atmospheric measurements of carbon dioxide and methane are essential for our understanding of the carbon cycle and how it changes in a warming climate. Such measurements are made on a regular basis by global networks of surface stations, by specially

1 Introduction

instrumented aircraft and by research ships (Masarie and Tans, 1995). When local influences are filtered out, the data from these measurements allow the identification of global trends in the abundance of greenhouse gases. Moreover, by using atmospheric transport models and inverse methods, major greenhouse gas sources and sinks can be localised and quantified, generally on the scale of continents (Fan et al., 1998; Ciais et al., 2010). This is called the top-down approach to the quantification of the carbon cycle.

The complementary strategy, called bottom-up approach, starts with quantifying sources and sinks on a small scale such as the single plant or ecosystem level. Regional or global estimates of carbon exchange can be derived from this data by generalising and upscaling the findings with the help of larger-scale data sets, e.g. from Earth observation satellites and weather models. Generalisation can be achieved by formulation and parametrisation of models (e.g. Knorr, 2000) or by application of machine learning algorithms (Jung et al., 2009).

Atmospheric phenomena such as diffusion, plume dispersion, convection and synoptic weather events cover a large spatial range from sub-meter to continental scale. As they are important for both the top-down and the bottom-up approach, a complete picture of the carbon cycle can only be obtained if experimental methods are available that cover all of these scales. For studying the small end of the scale a variety of enclosure based measurement techniques have been developed, while the large end of the scale is reasonably well covered by global networks such as the WMO GAW (World Meteorological Organization Global Atmospheric Watch) program (WMO, 2001). However, intermediate scales are less well accessible. Specifically, the transition region between micro- and mesoscale in the sense of Orlanski (1975) poses a challenge. It comprises horizontal extents of 200 m to 20 km and periods from minutes to hours. The size of many human settlements and many ecosystems, both important contributors to the carbon cycle, lies in this region.

Stationary observations on instrumented masts or towers can deliver data on and beyond the time scale from minutes to hours, but due to their fixed location, the simultaneous sampling of phenomena on the micro- and mesoscale requires a network of stations so dense that it becomes prohibitively expensive for most use cases. Moreover, even tall towers can sample only the lowest few hundred meters of the atmosphere at a typically low number of fixed levels. Manned research aircraft, on the other hand, can take profiles and transects of the atmosphere in little time. However, for safety reasons they are generally not permitted to fly in the lowest layers of the atmosphere besides during take-off and landing. Missed approaches, i.e. intentionally discontinued landing approaches, allow the collection of air samples close to the ground, but this manoeuvre may only be performed at sites where the aircraft could actually land. Furthermore, because their operation is costly, manned aircraft are typically deployed for short periods of time only.

1.4 Unmanned aircraft systems

Unmanned aircraft systems (UAS), also called remotely piloted aircraft systems (RPAS), unmanned aerial vehicles (UAVs) or “drones”, have the potential to fill this observational gap. The International Civil Aviation Organization (ICAO) defines them as “pilotless aircraft [...] either remotely and fully controlled from another place (ground, another aircraft, space) or programmed and fully autonomous” (ICAO, 2005, p. B-6). For small-scale studies, UAS match or surpass the versatility of manned aircraft at a much lower operational cost. Especially smaller UAS with a mass of few kilograms are becoming more and more attractive for research. They can be operated by one or two persons in almost any environment and their prices are particularly low. UAS that are capable of fully autonomous flight are now available for few thousand Euros, which has become possible by the development of small and cheap electronics for inertial measurements and satellite navigation as well as a growing consumer market. Obtaining an operating permit is easier for lightweight platforms and no certification is required for potential custom modifications. Consequently, the use of small unmanned aircraft for research purposes has increased substantially over the past years.

A fundamental limitation of small UAS is their payload capacity, both in space and mass. For the meteorological quantities air temperature, humidity and pressure, compact and lightweight instrumentation has long been available, which is one reason why small UAS have been used in the field of meteorology for two decades (e.g. Egger et al. 2002; Spiess et al. 2007; Reuder et al. 2008). Airborne studies of the carbon cycle, however, require accurate trace gas sensors, which are hard to miniaturise.

1.5 Aim and structure of this work

With this work we want to demonstrate that natural and anthropogenic CO₂ signals in the atmosphere can be studied in a cost-effective and highly flexible way by using small unmanned aircraft. To this end, an analyser is needed that provides accurate measurements and is small and light enough to be carried by a small UAS. Atmospheric signals on the micro- and mesoscale in CO₂ are typically in the range of 1–100 μmol·mol⁻¹, while the background CO₂ dry air mole fraction¹ x_{CO_2} is about 400 μmol·mol⁻¹. If the sensitivity of the CO₂ analyser changes by only 1% during flight, e.g. due to the changes in ambient temperature, the resulting disturbance of 4 μmol·mol⁻¹ will obscure small signals. The uncertainty of the CO₂ measurements should therefore not be higher than 1 μmol·mol⁻¹, even under fast changes in environmental conditions. To be compatible with a variety of small UAS, the analyser’s weight should be not more than 1 kg. There

¹Throughout this dissertation, x_{CO_2} denotes the CO₂ dry air mole fraction at a point, i.e. the result of an in situ measurement.

1 Introduction

is no commercial off-the-shelf instrument available that fulfils these requirements. Therefore, we decided to develop COCAP, the COmpact Carbon dioxide analyser for Airborne Platforms. Its components and our calibration strategy are detailed in Chapter 2. In Chap. 3 we present the results from different tests that we carried out to assess COCAP's performance.

Once COCAP was ready for use and had proven its reliability, we applied this new tool to a question where traditional approaches struggle to yield reliable answers. Gas exchange between biosphere and atmosphere on the ecosystem level is commonly measured using the eddy covariance (EC) technique, which works well under turbulent conditions, but is subject to biases under stable conditions. This problem is most pronounced during the night, when radiative cooling of the surface often leads to stable stratification of the lowest part of the atmosphere. Therefore, independent methods for the measurement of nocturnal biogenic fluxes are required. Nocturnal boundary layer (NBL) budgets provide such a method, but difficulties in data collection have hindered their application in the past. In Chapter 4 we explain how the NBL budget method works and how the strengths of a UAS-borne carbon dioxide analyser can be leveraged to acquire the necessary data. Furthermore, we present enhancements to the NBL budget method such as the treatment of subsidence and a way to calculate the budgets' area of sensitivity, i.e. their footprint. We compare the flux estimates obtained from NBL budgets to fluxes observed in similar ecosystems and analyse the sensitivity of the flux estimates to experimental uncertainties.

2 A compact carbon dioxide analyser for airborne platforms

2.1 Literature review

Solutions for the measurement of greenhouse gases on board unmanned platforms have been found, but are not yet widely used, likely for practical and financial reasons. Berman et al. (2012) deployed a custom-built laser-based water vapour, carbon dioxide and methane analyser on the NASA SIERRA UAS, but the dimensions of $30 \times 30 \times 28 \text{ cm}^3$ and the mass of 20 kg prevent the use of this analyser on small, cost-effective systems. Khan et al. (2012) developed a smaller laser-based analyser for carbon dioxide or methane dry air mole fraction with a mass of 2 kg and a size of $20 \times 5 \times 5 \text{ cm}^3$. The estimated drift in x_{CO_2} during 5–10 minute flights with a small helicopter was 1 %, which limits the system's suitability for environmental studies. Watai et al. (2006) deployed a 3.5 kg measurement package containing a nondispersive infrared CO_2 sensor on a UAS. They reported a comparably low bias of $0.21 \mu\text{mol} \cdot \text{mol}^{-1}$ during tests with temperature changes similar to the conditions during flight. However, their setup requires 1 minute of in-flight calibrations every 6 minutes and comprises two gas cylinders, a pump and a drying cartridge in addition to a $20 \times 14 \times 8 \text{ cm}^3$ main module.

Recently, attempts have been made to equip UASs with commercial off-the-shelf CO_2 sensors designed for indoor air quality measurements. Their advantages are low cost, compact size and small mass of the measurement system. Brady et al. (2016) flew a 500 g payload containing such a CO_2 sensor on a small multicopter, but due to its high uncertainty (30 ppm plus 3% of reading according to manufacturer's specifications) the resulting data is hard to interpret. Numerous other groups have improved the accuracy of compact sensors by custom calibrations (e.g. Yasuda et al., 2012; Piedrahita et al., 2014; Shusterman et al., 2016; Martin et al., 2017). In some of these studies, measurement uncertainties below $5 \mu\text{mol} \cdot \text{mol}^{-1}$ have been achieved (Shusterman et al., 2016; Martin et al., 2017). However, none of these efforts aimed at the deployment of the sensors on UAS, which requires immunity to rapid changes in pressure and temperature as well as a high time resolution.

Aiming for a measurement package that is compact, accurate and robust, we have developed COCAP, the COmpact Carbon dioxide analyser for Airborne Platforms. It is

2 A compact carbon dioxide analyser for airborne platforms

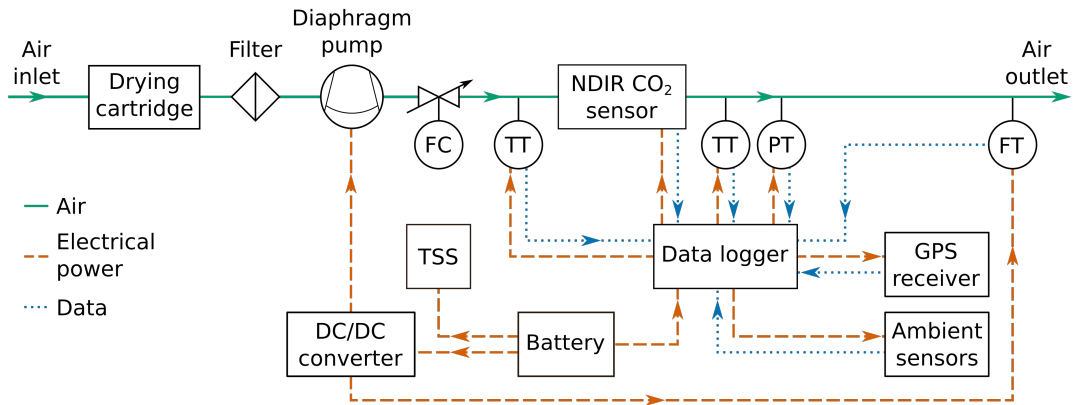


Figure 2.1: Flow of air, electrical power and data inside COCAP. FC – mass flow controller, TT – temperature transmitter (sensor), PT – pressure transmitter, FT – mass flow transmitter, TSS - temperature stabilisation system. The NDIR (nondispersive infrared) CO₂ sensor contains additional temperature sensors which are not included in this schematic view.

not merely a CO₂ sensor, but a self-contained package including meteorological sensors, a pump, a data logger and a temperature stabilisation system. The components of COCAP are explained in Sect. 2.2. Section 2.3 is a description of the field calibration device we designed for use with COCAP. Section 2.4 provides an overview of the different types of unmanned aircraft on which COCAP has been or could be deployed. The cost of the different elements of the measurement system is estimated in Sect. 2.5. Section 2.6 focuses on our strategy to ensure accurate measurements through calibration of COCAP's sensors. A summary of the whole chapter can be found in Sect. 2.7.

2.2 COCAP

2.2.1 System overview

COCAP measures CO₂ dry air mole fraction, temperature, relative humidity and pressure of ambient air. Furthermore, flow rate, pressure and temperature at different locations inside the analyser are recorded. We designed COCAP as an independent package containing not only sensors, but also control and data logging capabilities as well as a GPS receiver that provides position data and acts as time source. The mass of COCAP is 1 kg, excluding battery.

A schematic view of COCAP is provided in Fig. 2.1. All components but the battery and the drying cartridge are housed in a custom-built enclosure made from expanded

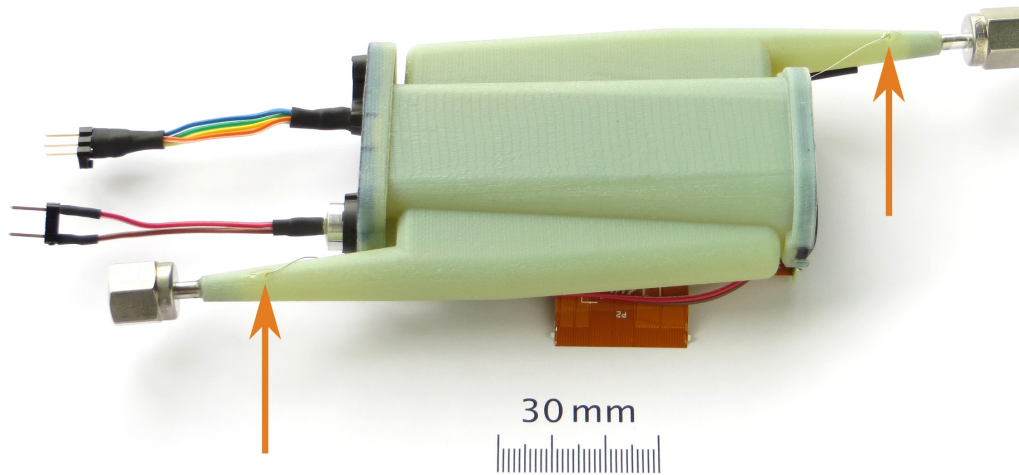


Figure 2.2: COCAP's carbon dioxide sensor, based on SenseAir AB's HPP family (High Performance Platform) of gas sensors. For deployment in COCAP it was built with a custom, 3D-printed measurement cell. The arrows indicate the location of temperature sensors inside inlet and outlet.

polypropylene (EPP). The enclosure has a wall thickness of 3 cm and acts both as mechanical protection and as thermal insulation. The enclosure is covered with a reflective metallised polymer film ("space blanket") to prevent heating of COCAP by sunlight.

2.2.2 Carbon dioxide sensor

COCAP measures carbon dioxide using a sensor (Fig. 2.2) from SenseAir AB based on their HPP (High Performance Platform) family of gas sensors (Hummelgård et al., 2015). It is a nondispersive infrared sensor operating at a wavelength of $4.26 \mu\text{m}$. The optical path has a length of 128 cm, which is obtained by 16 passes in an 8 cm long White cell (White, 1942). The total internal volume of the cell is 48 cm^3 . The mirrors are fabricated using plastic moulding which lowers the production cost. Heating elements and temperature sensors that enable temperature stabilisation of the optics are moulded into the mirrors. The sensor's mass is 80 g, including electronics. It was built with a custom, 3D-printed measurement cell that minimizes the time required for flushing by preventing dead volumes.

2 A compact carbon dioxide analyser for airborne platforms



Figure 2.3: Cartridges for drying agent (magnesium perchlorate)

2.2.3 Other components in the gas sampling line

Air that is drawn into COCAP's sample line is chemically dried as a first step. The drying facilitates the measurement of the *dry air* mole fraction of CO₂, avoids spectroscopic interferences and prevents condensation of water in the pump. We use magnesium perchlorate (105873, Merck KGaA, Germany) in cartridges built in-house from aluminium (Fig. 2.3). For improved drying performance we sieve the magnesium perchlorate and use only particles smaller than 2 mm. A single drying cartridge holds 1.5 g magnesium perchlorate, which is sufficient to dry nearly saturated air at a temperature of 24 °C and a flow rate of 300 ml·min⁻¹ to a water mole fraction of less than 200 µmol·mol⁻¹ for one hour.

Downstream of the drying cartridge a 0.2 µm filter (CM-0118, CO2Meter.com, USA) protects pump, flow regulator and CO₂ sensor from particles. The air flow through the gas line is driven by a diaphragm pump (NMS 020 B, KNF Neuberger GmbH, Germany) and throttled to a flow rate of 300 ml·min⁻¹ by the mechanical flow controller (PCFCDH-1N1-V, Beswick Engineering Inc., USA). At this flow rate the pump reaches a differential pressure of 350 hPa, whereas the flow controller is preset at the factory to a higher pressure difference of 700 hPa. We lowered the setting of the flow controller, but tests indicate that in the current configuration the flow rate is directly proportional to ambient pressure, i.e. the flow controller behaves like a needle valve. In future designs we recommend to better tune the flow controller for performance at low pressure differences or to reduce mass by replacing it with a needle valve.

The temperature of sample air is measured inside the inlet and the outlet of the CO₂ sensor with miniature thermistors (NCP15XH103F03RC, Murata Ltd., Japan) that are suspended from 0.2 mm diameter wire (Fig. 2.2 and 2.5). Pressure is measured with a compact piezoresistive pressure sensor (LPS331AP, ST Microelectronics, Switzerland). This model was chosen for its small physical size, high resolution and digital interface. As it lacks a connection port, we glued a 3D-printed cap with a turned stainless steel port connector to the PCB so that it forms an airtight enclosure around the pressure sensor (Fig. 2.4). The sample pressure is measured downstream of the CO₂ sensor close to its outlet. As the flow between the measurement cell and this point is virtually unrestricted, we assume equal pressure, i.e. we treat the reading of the pressure sensor as the pressure of the air inside the CO₂ sensor's measurement cell.

Finally, the mass flow rate of the sample air is measured with an analogue sensor (AWM3300V, Honeywell, USA). Downstream of the mass flow sensor the sample air is released from the gas line into COCAP's housing.

2 A compact carbon dioxide analyser for airborne platforms

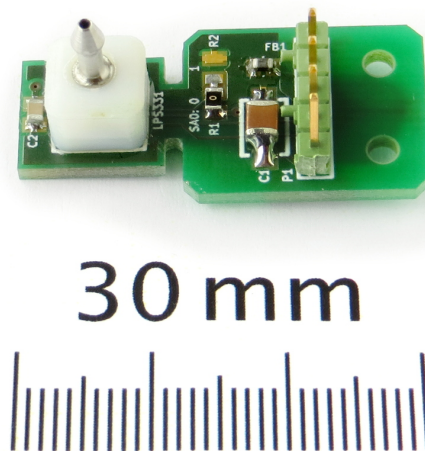


Figure 2.4: Sensor board for measurement of pressure in the gas line. The pressure sensor is located beneath the white cap ($7 \times 7 \times 6 \text{ mm}^3$). The shape of the PCB prevents bending of the sensor which would degrade the measurement.

2.2.4 Ambient sensors

The measurement of features in temperature and humidity on the scale of tens of meters with UAS that can move several meters per second requires fast measurements with time constants on the order of 1 s. This calls for unrestricted or even forced ventilation of the sensing elements. To this end we designed a small ($60 \times 35 \text{ mm}^2$) printed circuit board (PCB) that can be mounted in the most suitable location for any UAS (Fig. 2.6). Temperature is measured with a platinum resistance thermometer (Platinum 600 °C MiniSens Pt1000, IST AG, Switzerland), humidity is measured with a capacitive humidity sensor (P14 rapid in wired configuration, IST AG, Switzerland). Both sensors protrude over the edge of the PCB, which minimises thermal mass and improves ventilation. They are protected from mechanical damage and contamination by an aluminium tube (length 30 mm, inner diameter 12 mm). The tube is polished on the outside to prevent heating by the sun and anodized matt black on the inside which avoids reflection and focusing of sunlight onto the sensors. On fixed-wing UAS we mount the PCB forward-facing, on rotary-wing UAS upward-facing in the downwash of the rotors.

2.2.5 Data logger

The data from all sensors are recorded to a memory card by a data logger. For this purpose we modified an electronics board designed for the operation with SenseAir's

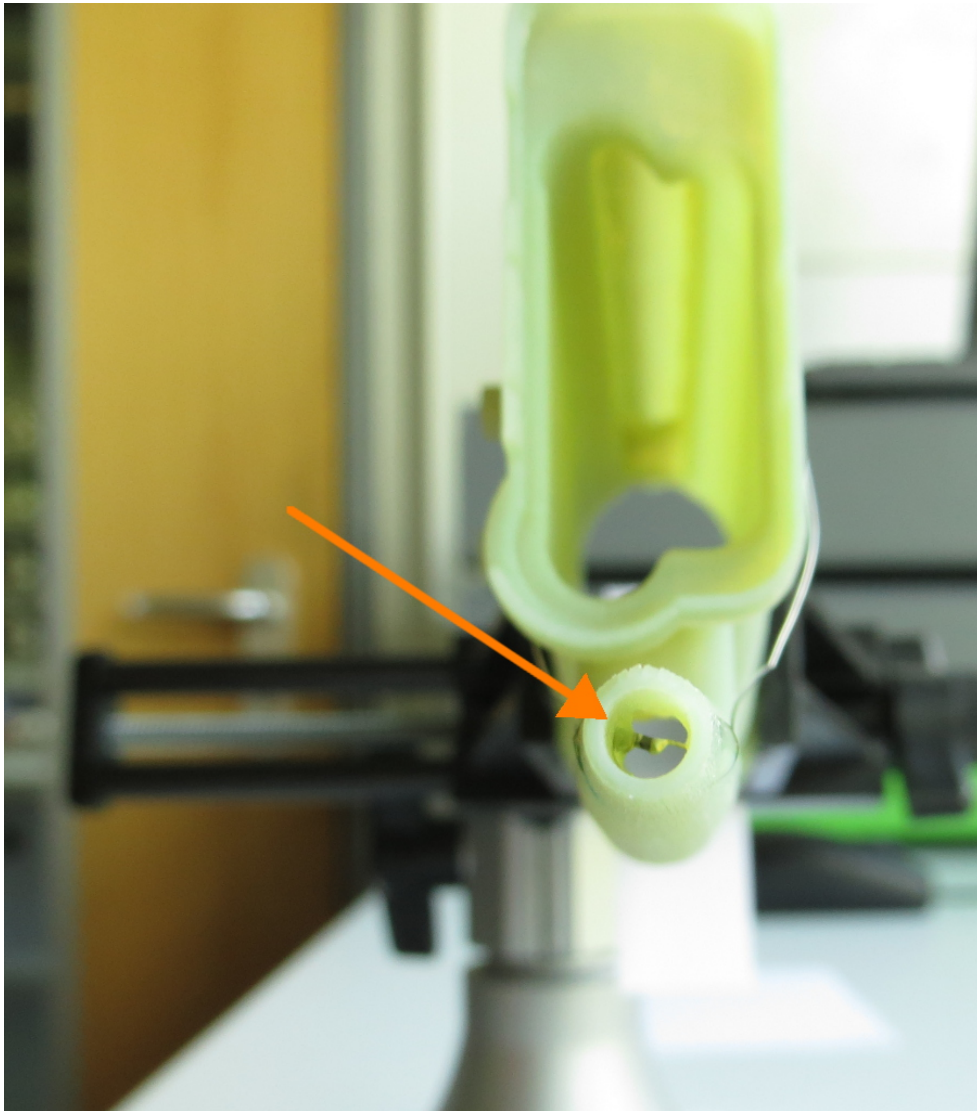


Figure 2.5: Detail of the outlet temperature sensor

2 A compact carbon dioxide analyser for airborne platforms

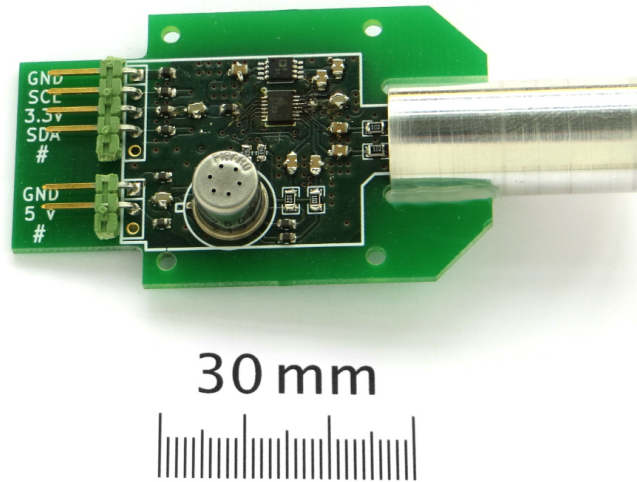


Figure 2.6: PCB for measuring temperature and relative humidity of ambient air. The sensors are protected by an aluminium tube (right hand side). A conformal coating covering all electronic components but the sensors prevents stray currents under humid conditions.

HPP gas sensors (Hök Instruments AB, Sweden) by adding connectors that provide an interface for the GPS receiver and different digital sensors. The board runs a firmware written for COCAP at the MPI for Biogeochemistry (Jeschag, 2014). Sensor data is recorded at 1 Hz. If a sensor samples at a higher rate, the measurements are averaged over one second. Data are continuously output via a serial interface and can be transmitted to a computer by means of an adaptor cable or a pair of radio modules (XBee 868, Digi International Inc., USA), allowing for real-time data visualisation and analysis. In addition, the data logger controls the built-in heaters of the CO₂ sensor to a user-adjustable temperature.

2.2.6 Temperature stabilisation

The temperature inside and outside COCAP influences the measurement of carbon dioxide in different ways. First, the density of the sample air and therefore the number of absorbing molecules in the measurement cell is inversely proportional to absolute temperature (ideal gas law, Clapeyron, 1834). Secondly, electronic components and the optical band-pass filter in the CO₂ sensor change their properties with temperature (Wilson, 2011; SCHOTT, 2015). Thirdly, the intensity of the absorption lines of any gas depends on temperature, which makes the optical depth of the sample air temperature dependent (McClatchey et al., 1973). Fourthly, changes in temperature influence the

emission strength of the IR source. Fifthly, thermal expansion may cause mechanical deformations of the optical assembly. We correct the x_{CO_2} readings for changes of the measurement system with temperature (see Sect. 2.6.1), but experience with earlier setups shows that for best possible precision an active stabilisation of temperature is needed.

The HPP CO₂ sensor has built-in heaters and temperature sensors that are thermally coupled to the optical surfaces, the IR source and the optical detector. In an earlier version of COCAP we covered the CO₂ sensor with isolating material and preheated the air stream with a heated tube that was connected to the sensor inlet. In this setup, the temperature at three points could be precisely controlled to 50 °C, but the distribution of temperature was inhomogeneous and varying with ambient conditions. Although a total of 9 temperature sensors were present at different locations in COCAP, the uneven temperature distribution made it impossible to fully determine the system's thermal state and a satisfactory temperature correction could not be established.

Consequently, we redesigned the stabilisation system to minimise temperature differences around the CO₂ sensor. This goal requires a setup where the heat exchange between different parts of the sensor happens much faster than dissipation of heat from the sensor to the changing environment. In many instruments this is achieved by means of massive bodies of copper or aluminium, which are characterised by high thermal diffusivity. However, as the mass of large metal parts is unacceptable for our application, we use air to transport heat inside COCAP. The lower thermal diffusivity of air is compensated for by forced convection driven by a fan. A heater, a temperature sensor and a custom PCB are connected and programmed as a control loop that stabilises the air temperature at 50 °C. The warm air stream circulates throughout COCAP's housing (Fig. 2.7) so that not only the CO₂ sensor is decoupled from changes in ambient temperature, but all electronics boards benefit from the stabilisation as well.

While being flown on a UAS the temperature around COCAP can change by several degrees within seconds. Compensation of these changes requires a fast control loop, which calls for a heating element and a temperature sensor with low thermal mass. We built the heating element (Fig. 2.8) from 38 surface-mount technology resistors (nominal resistance 360 Ω, length × width 2 × 1.25 mm², rated power 0.5 W) which are connected in parallel and provide a maximum heating power of 15 W at 12 V. We installed the heating element just above the air inlet of the fan (RLF 35-8/12 N, ebm-papst Mulfingen GmbH & Co. KG, Germany). Placing the heating element at the outlet of the fan would reduce the response time, but likely result in a less homogeneous temperature distribution across the air stream.

The temperature sensor ("air stream sensor", Fig. 2.9) in the control loop is a miniature thermistor (NCP15XH103F03RC, Murata Ltd., Japan). It is placed close to the detector

2 A compact carbon dioxide analyser for airborne platforms

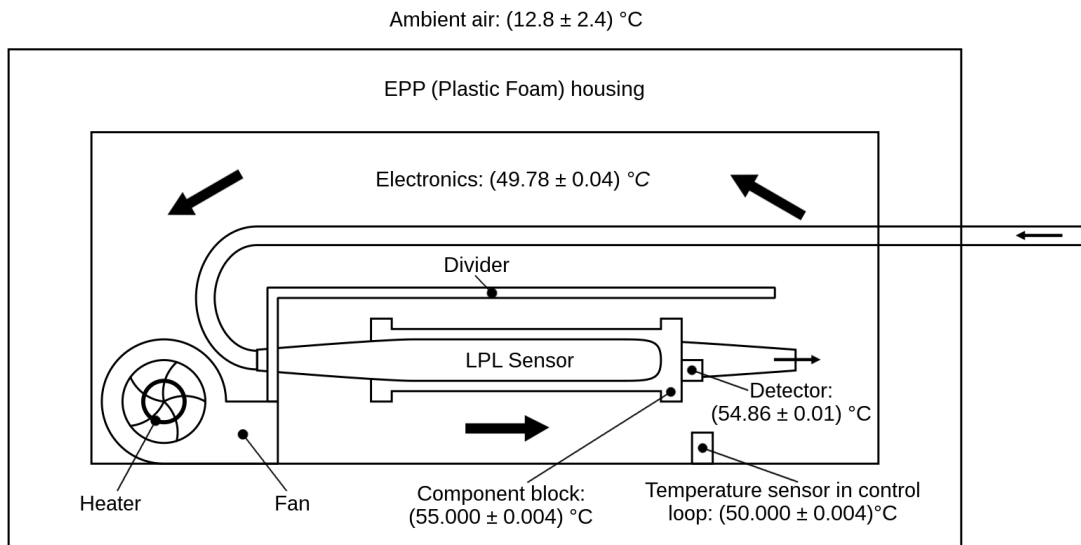


Figure 2.7: Temperature stabilisation of COCAP. A fan drives circulation of air inside the housing as indicated with the large arrows. The heater at the fan inlet is controlled to stabilise the temperature of the air stream to $50 \text{ }^\circ\text{C}$. The values given are mean and standard deviation of temperature at the respective point during flight simulations in an environmental chamber (see Sect. 5.1.2). During the simulations the temperature of the ambient air varied between 6.7 and $15.5 \text{ }^\circ\text{C}$. Temperatures outside this range may be encountered in field deployments, but the change in temperature between two calibrations is typically smaller.

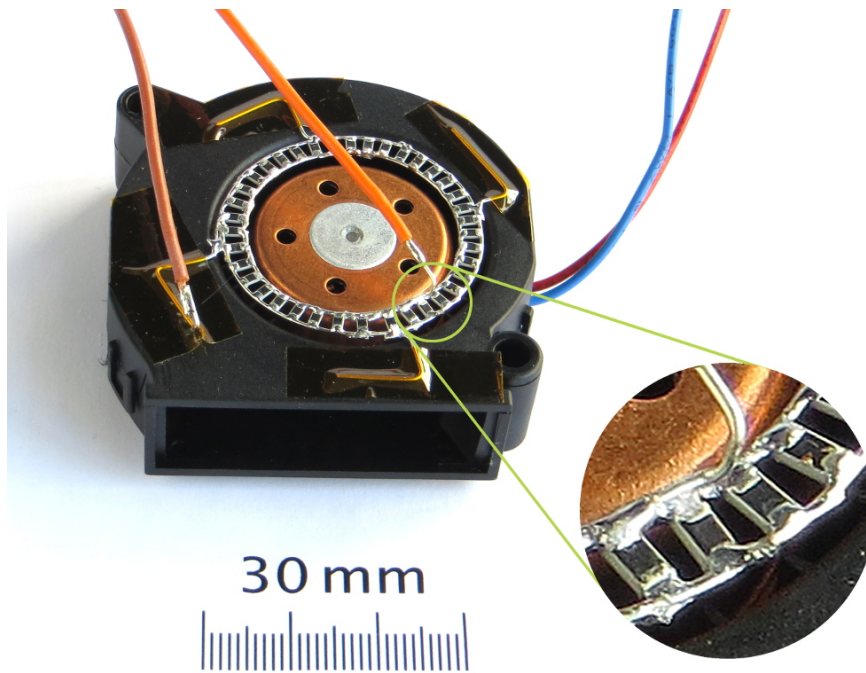


Figure 2.8: Fan and heating element used to stabilise temperature inside COCAP. The heating element is made of surface-mount technology resistors soldered to two concentric rings of wire. It is located just above the air inlet of the radial fan.

2 A compact carbon dioxide analyser for airborne platforms

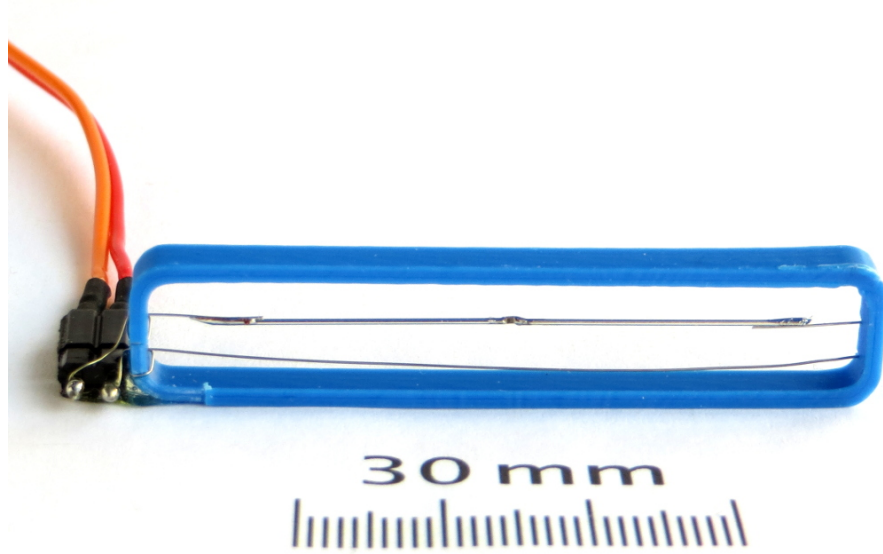


Figure 2.9: Sensor used for the measurement of the temperature of the air circulating inside COCAP. The sensing element (located in the centre of the blue 3D-printed frame) is a miniature thermistor ($1\text{ mm} \times 0.5\text{ mm} \times 0.5\text{ mm}$). Two 23 mm long pieces of 0.5 mm wire are soldered to both sides of the thermistor. They conduct heat, facilitating the measurement of a temperature that is averaged across the air stream.

of the CO₂ sensor and oriented perpendicular to the flow of circulating air to minimise flow resistance.

Fan, heating element and air stream sensor are connected to an in-house-built control board (Fig. 2.10 and 2.11) that runs a PID (proportional–integral–derivative) controller implemented in software. The temperature-dependent resistance of the air stream sensor is measured in a Wheatstone bridge configuration with a resolution of 1 mK at 50 °C. A trimmer potentiometer allows calibration of the temperature measurement. The control board detects if the thermistor is shorted or disconnected and disables heating in such cases.

The power dissipation of the heating element is controlled by pulse-width modulation with 16 bits resolution. The control board monitors the current drawn by the fan and powers the heating element only if the fan is operating normally. This protection prevents damage to the heating element which would overheat if the fan is disconnected or broken.

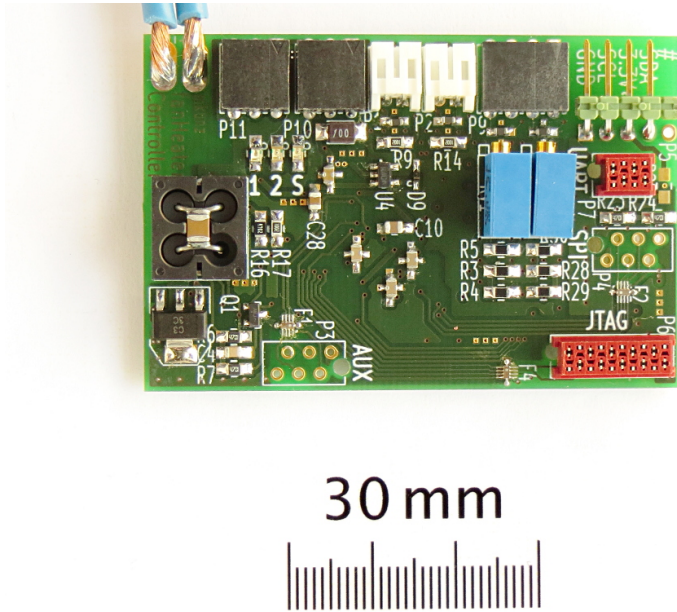


Figure 2.10: Front side of the temperature control board. Two control channels for temperature measurement and heater control are available, but only one is currently in use.

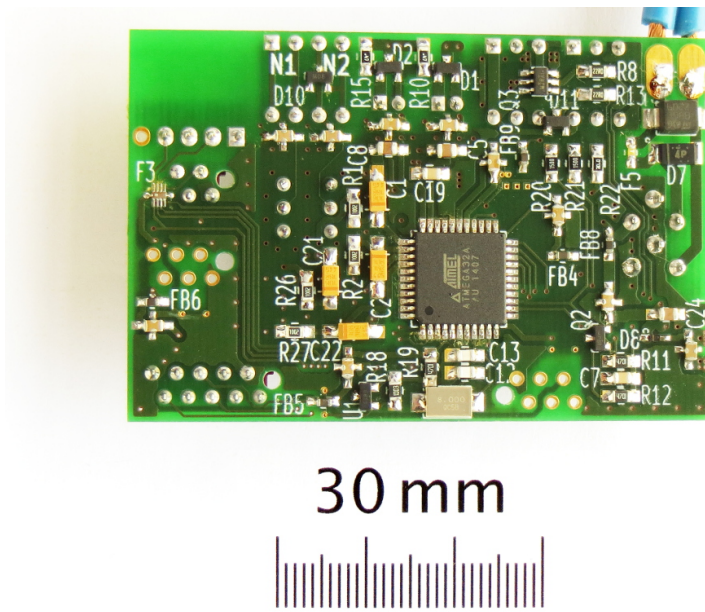


Figure 2.11: Back side of temperature control board with the Atmega32A (Atmel, USA) microcontroller that runs the PID controller

2 A compact carbon dioxide analyser for airborne platforms

The performance of the temperature stabilisation under flight conditions is discussed in Sect. 3.3 and Sect. 3.4.

2.2.7 Battery

COCAP requires a source of electrical power with a voltage in the range 10.2–14.0 V. We use a single lithium polymer battery with a nominal voltage of 11.1 V. The battery life time depends on the ambient temperature, but generally we can operate COCAP for more than one hour from a 2200 mAh battery weighing 200 g. By choosing a different battery size the package can be optimised for lower mass or longer run time.

2.3 Field calibration device

The periodic calibration of COCAP in the field with two different gas standards is necessary to avoid drift of the CO₂ measurement. In order to make the handling of gas cylinders in the field easier and safer we developed a field calibration device (Fig. 2.12). It consists of a gas cylinder dolly, accommodating two 10 l aluminium cylinders, and a valve box. The cylinders are securely tied to the dolly so that they can stay in place at all times, which simplifies transportation. Inside the valve box a three way valve allows switching between the two gas standards or shutting off the gas stream. The flow rate is controlled to 400 ml·min⁻¹ with a mechanical flow controller (PCFCDH-1N1-V, Beswick Engineering Inc., USA). The connection to COCAP has an open-split configuration so that there is always an 100 ml·min⁻¹ overflow and the gas standard is delivered at ambient pressure. At a field site three steps are necessary to make the system ready for use: (1) removing the protective caps from the cylinders, (2) mounting (including leak checking and flushing) of the pressure regulators (Model 14, Air Liquide USA LLC) and (3) connecting them to the valve box. For details of the field calibration sequence and gas standards see Sect. 2.6.3

2.4 Unmanned aircraft

2.4.1 Requirements of COCAP

COCAP has no dependence on any external system and can therefore be deployed on a variety of UAS. The only requirements are a payload capacity of typically 1.2 kg (depending on the choice of battery, see Sect. 2.2.7) and space for the 14×14×42 cm³ package, either inside the fuselage or attached to the outside of the vehicle. Sufficient ventilation must be ensured to prevent overheating. In Germany, UAS can be operated



Figure 2.12: Field calibration device

2 A compact carbon dioxide analyser for airborne platforms

without a permit at low heights¹ up to 100 m if their take-off mass is lower than 5 kg. COCAP's size and mass generally allow to meet this limit. In the following we give an overview of the platforms that we have used in the past and others that are potentially suitable for carrying COCAP.

2.4.2 Multicopters

Multicopters are rotary-wing aircraft with more than two rotors. They are generally easier to handle than fixed-wing aircraft due to their hovering ability and their built-in electronic control systems. Multicopters feature vertical take-off and landing as well as arbitrarily low vertical and horizontal flight speed. However, for aerodynamic reasons they typically have a lower endurance than fixed-wing aircraft of similar mass. Moreover, the strong mixing around and below the rotors gives rise to an uncertainty of the origin of a measured air sample. We alleviate this problem by sampling air through a carbon fibre tube with the inlet placed sideways or above the rotors.

So far we have flown COCAP on two different multicopters. One is an octocopter (S1000, DJI Ltd., China) with a total take-off mass of 8 kg. The other one is a quadcopter (custom-built, Sensomotion UG, Germany and Ostwestfalen-Lippe University of Applied Sciences, Germany, Fig. 2.13) weighing 4.8 kg with COCAP mounted. Both multicopters are electrically powered and provide at least 10 minutes of flight time.

2.4.3 Fixed-wing aircraft

Fixed-wing aircraft require a minimum air speed to fly and generally depend on an airstrip or additional equipment like bungees and nets for take-off and landing. On the other hand, they tend to have higher endurance and longer reach than multicopters. In addition, their high forward air speed makes it easy to mount sensors in a way that they are well ventilated by undisturbed air, i.e. by air that was not in contact with or displaced by the aircraft.

We carried out successful flight tests with an electrically powered fixed-wing aircraft (X8, Skywalker Technology Ltd., China) using a dummy that has the same mass and size as COCAP. The complete system weighed approximately 3.6 kg.

2.4.4 Other platforms

Two potentially suitable types of UAS that we have not yet tested are helicopters and tethered balloons. Helicopters, being lifted by one or two rotors, share the strengths of multicopters listed in Sect. 2.4.2. Additionally, they are more efficient, more stable

¹Throughout this dissertation, "height" specifies the vertical distance from ground level



Figure 2.13: COCAP mounted under a custom-built multicopter

2 A compact carbon dioxide analyser for airborne platforms

in windy conditions and generally achieve higher speeds, which translates to a longer reach.

Tethered balloons need no power to generate lift, allowing measurement periods that are limited only by the battery capacity of COCAP. Furthermore, they cause less disturbance of the air as they create no downwash. Their main disadvantages are the limited or absent manoeuvrability and the need for special ground equipment, at the least a winch.

2.5 Cost estimation

The cost estimate provided here includes materials and components in the state in which we procured them, but excludes any labour associated to their modification and assembly. We estimate the material costs for COCAP at EUR 4 500 and for the field calibration device (including two cylinders, but not the gas standards inside) at EUR 3 300. The recurring costs for gas standards and drying agent are few euros per flight and thus negligible.

Commercial off-the-shelf multicopters with a payload capacity of at least 1.2 kg are available for EUR 3 000, including essential equipment such as battery, charger and remote control.

2.6 Calibration

2.6.1 Calibration curve of the CO₂ sensor

A nondispersive infrared gas sensor measures the fraction of one component in a mixture of gases utilising the characteristic absorption bands that many substances exhibit in the infrared. The HPP sensor inside COCAP outputs a signal that is approximately proportional to the intensity of infrared radiation that has passed through the gas mixture. Absorption by one constituent of the gas reduces the intensity, but the relation between the mole fraction of this component and the intensity is non-linear and depends on temperature and pressure of the gas. Furthermore, sensor elements like the infrared source and detector can have a temperature dependence that influences the measurement. Generally, the carbon dioxide mole fraction x_{CO_2} of the gas mixture can be calculated as

$$x_{\text{CO}_2} = k(s, T_G, p_G, \dots) \quad (2.6.1)$$

where s is the infrared signal, T_G and p_G are temperature and pressure of the gas mixture, respectively, and the ellipsis indicates that other quantities may be included in

the calculation. The function k will henceforth be called the “calibration curve” of the carbon dioxide sensor.

Although an ab initio calculation of the calibration curve is in principle possible, we did not follow this approach due to lack of information (e.g. the precise transmission characteristics of the optical band-pass filter). Instead, we made a series of measurements with known CO₂ dry air mole fraction under changing ambient conditions and used regression analysis to approximate the calibration curve. To this end we placed COCAP in an environmental chamber where ambient temperature and pressure could be varied over the range expected in field deployments (Fig. 2.14 panel b and c). Temperature was changed in a step pattern from 28 °C to 0 °C while pressure was smoothly adjusted from 1100 hPa to 700 hPa and back during each temperature step. These disparate patterns were chosen to ease the attribution of sensitivities to one of the independent variables. Sample air with gradually changing CO₂ dry air mole fraction was provided to COCAP from a spherical, stainless steel, 8 l buffer volume that was continuously flushed with air from one of two gas cylinders (Fig. 2.15). One cylinder contained a lower-than-ambient CO₂ dry air mole fraction (349.9 μmol·mol⁻¹), the other one was enriched with CO₂ (648.6 μmol·mol⁻¹). At a flow rate of 400 ml·min⁻¹ the buffer volume acted approximately as a first order low-pass filter with a time constant of 20 min (Fig. 2.14a). Air leaving COCAP was directed to a Picarro G2401 cavity ring-down spectroscopy (CRDS) analyser (O’Keefe and Deacon, 1988) that had been calibrated to the WMO CO₂ X2007 scale and served as reference. Open splits upstream and downstream of COCAP ensured that sample air was delivered to both analysers at chamber pressure despite different flow rates (COCAP 300 ml·min⁻¹, Picarro G2401 200 ml·min⁻¹).

The dominant features in the infrared signal (Fig. 2.14d) are the step changes in x_{CO_2} and the influence of pressure changes. Note that in a nondispersive infrared sensor the signal is inversely related to the amount of absorbing molecules in the measurement cell. Hence, both low x_{CO_2} and low pressure lead to a high signal. The gradual changes in x_{CO_2} by 200 μmol·mol⁻¹ between 0:40 h and 6:30 h have a smaller influence on the infrared signal than the changes in pressure do. This shows the importance of a precise correction for ambient influences.

In total we carried out three experiments similar to the one depicted in Fig. 2.14 on consecutive days. The variation in temperature and pressure were the same for all experiments, but the initial CO₂ dry air mole fraction in the buffer volume differed and the switching between low-CO₂ and high-CO₂ cylinders took place at different times.

Regression analysis of the experimental data was carried out in GNU Octave (Eaton et al., 2017) using the *leasqr* function from the *optim* package. It is an implementation of the Levenberg–Marquardt algorithm for non-linear least-squares regression that allows the variation of some parameters of a model while others are fixed. This capability enabled a stepwise approach in which we fitted one part of a model at a time until finally

2 A compact carbon dioxide analyser for airborne platforms

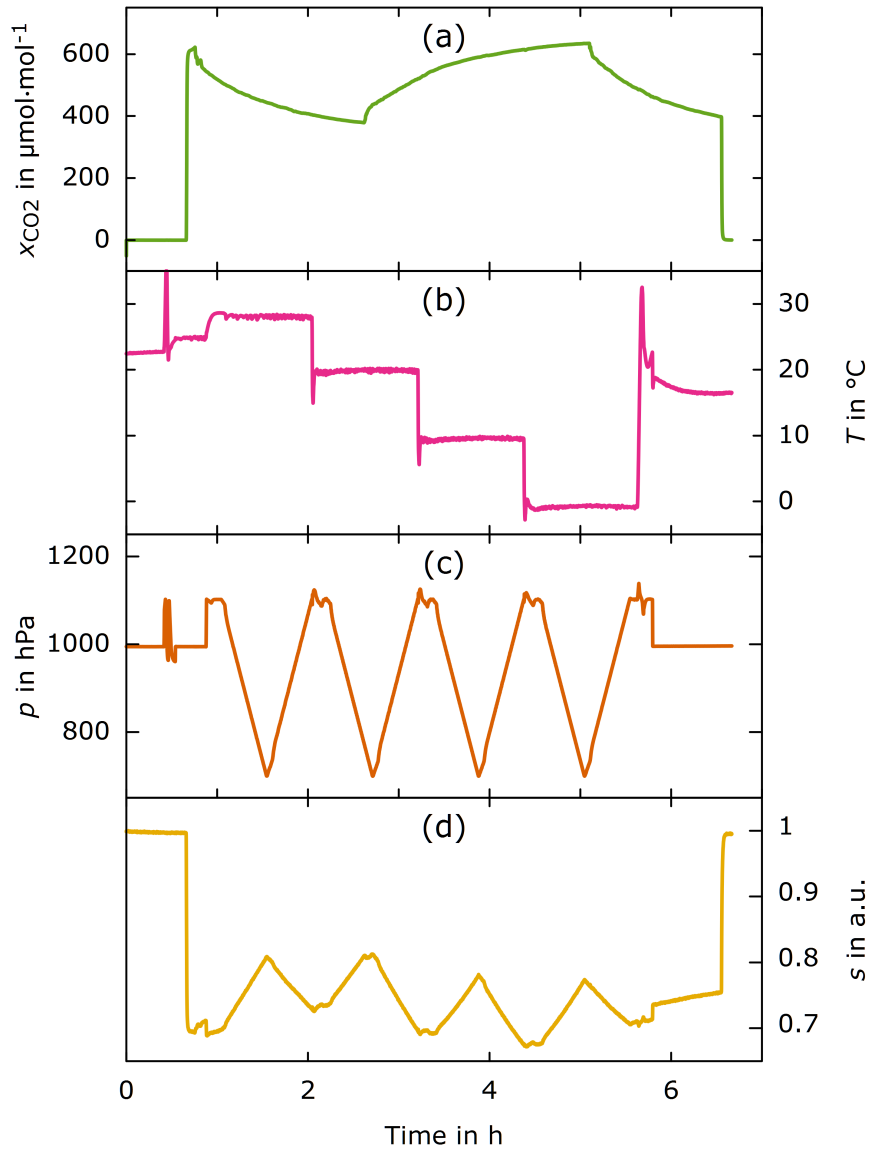


Figure 2.14: Conditions during one of the experiments carried out to define a calibration curve for the CO₂ sensor: (a) CO₂ dry air mole fraction x_{CO_2} measured with a reference analyser, (b) ambient temperature T , (c) ambient pressure p . (d) Normalised infrared signal s from the optical detector of COCAP's CO₂ sensor. The variations in pressure influence the observed signal more strongly than the changes in x_{CO_2} by $200 \mu\text{mol}\cdot\text{mol}^{-1}$, which illustrates the need for a precise pressure correction.

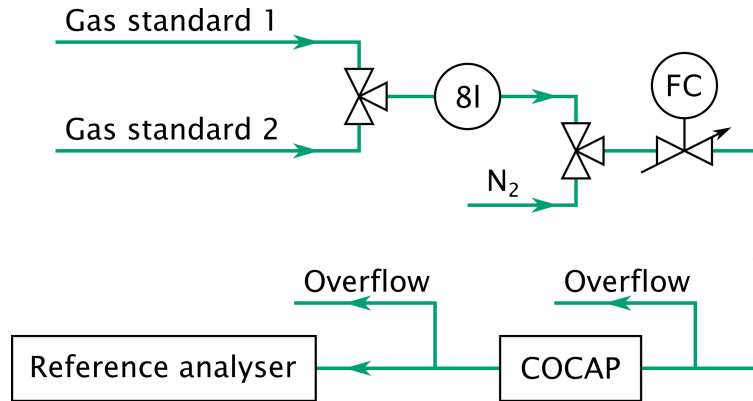


Figure 2.15: Setup used to determine a calibration curve for the CO₂ sensor. FC is a mass flow controller. The 8l buffer volume was flushed with either of two gas standards differing in CO₂ content, providing a slowly changing CO₂ dry air mole fraction. The second three-way valve is used to deliver nitrogen with zero CO₂ at the beginning and the end of each experiment.

all parameters could be set free. In contrast, straightforward fitting of a complete model at once did not converge. We attribute this to the high number of parameters (10 or more) and to the lack of initial values sufficiently close to the optimum.

The models that we fitted to the experimental data are of the form

$$x_{\text{CO}_2} = k(s, T, p \dots) \quad (2.6.2)$$

$$= \frac{g_1(T_{\text{Inlet}}, T_{\text{Outlet}})}{g_2(p)} \cdot g_3(g_4(s, \dots)) + b \quad (2.6.3)$$

The function g_1 represents the gas temperature, g_2 the pressure inside the measurement cell of the CO₂ sensor. The fraction g_1/g_2 originates from the ideal gas law, but in many of our models it has a more general form, including constant and quadratic terms to account for other effects like temperature or pressure broadening of absorption lines. The function g_3 is a polynomial of second or third order that approximates the non-linear relation between the amount of absorbing molecules in the measurement cell and the light intensity at the detector. The purpose of g_4 is to correct the detector signal for disturbances, e.g. change of gain with temperature. Finally, b is a constant representing the CO₂ sensor's offset.

In our regression analysis we repeatedly performed three steps: (1) formulation of a model, (2) fitting of the model to the experimental data by minimising the sum of squared residuals and (3) evaluation of the model performance. Given the large number of parameters in the models, the second step was susceptible to "overfitting", i.e. fitting

2 A compact carbon dioxide analyser for airborne platforms

Table 2.1: Summary of the calibration of COCAP’s ambient sensors: Conditions during calibration, correction model and root mean square error (RMSE) of the corrected indications with respect to the reference. T , U and p are temperature, relative humidity and pressure, respectively. The subscript R stands for raw, the subscript C for corrected measurements.

Sensor	T in °C	U in %	p in hPa	Model	RMSE
Temperature	5–40	50	1000	$a_1 T_R^2 + a_2 T_R + a_3$	0.04 °C
Humidity	10–30	15–100	1000	$a_1 U_R^2 + a_2 U_R + a_3$ $+ a_4 U_R \cdot T_C + a_5 T_C$	1.4 %
Pressure	0–40	N/A	400–1000	$a_1 p_R^2 + a_2 p_R + a_3$	1.1 hPa

to a point at which the model represents not only an underlying process, but also random variations in the experimental data. We countered overfitting in two ways. On the one hand, we rejected models in which an additional parameter reduced the sum of squared residuals only insignificantly. On the other hand, we validated the fitted models against independent data measured on a different day, which allowed us to assess the stability of the parameters over time. Based on these considerations we chose the following calibration curve:

$$x_{\text{CO}_2} = \frac{a_1 T_{\text{Outlet}} + a_2}{p + a_3} (a_4 g_4^3 + a_5 g_4^2 + g_4 + a_6) + a_7 \quad (2.6.4)$$

$$g_4(s, p) = \frac{s + a_8}{a_9 p + a_{10}} \quad (2.6.5)$$

a_1 through a_{10} are the parameters fitted in the regression. The capability of this calibration curve to compensate for ambient influences is illustrated in Fig. 2.16.

2.6.2 Calibration of ambient sensors

We calibrated COCAP’s temperature, humidity and pressure sensors prior to measurements in the field. The general calibration approach was the same for all three sensor types: As a first step, we placed them together with a reference instrument in an environmental chamber, varied the relevant ambient conditions and recorded the indications of both the sensor under test and the reference. As a second step, we fitted a model that relates the indications of the sensor under test to the reference measurements. This model can later be used to correct sensor indications during field measurements.

Calibration of the temperature and humidity sensors was carried out in a PSL-2KPH chamber (ESPEC Corp., Japan). A chilled-mirror dew point hygrometer (Dewmet TDH,

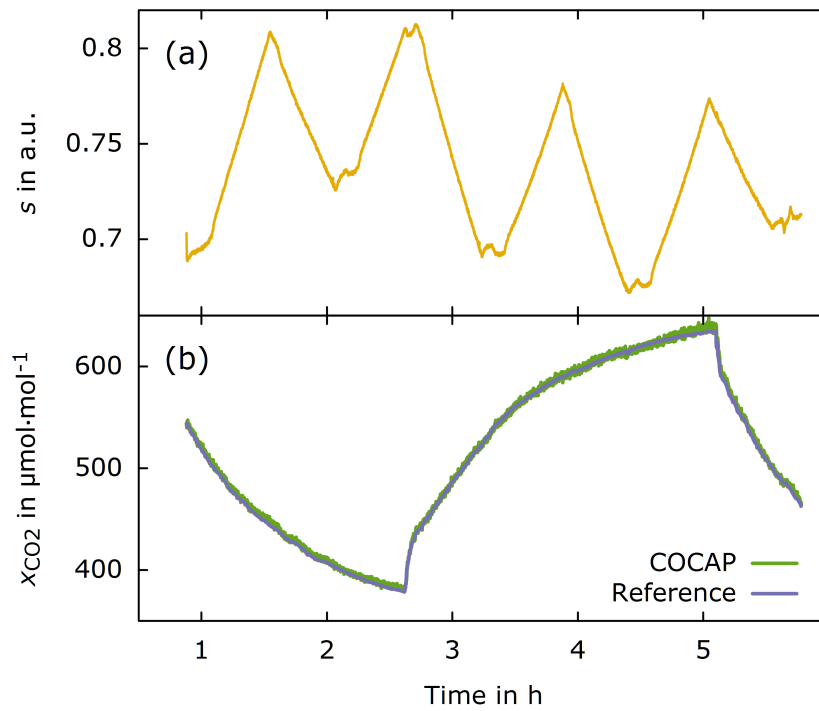


Figure 2.16: (a) Normalised infrared signal of COCAP's CO₂ sensor under changing ambient conditions. This is a subset of the data shown in Fig. 2.14d. (b) x_{CO_2} calculated using the calibration curve (Eq. 2.6.4 and 2.6.5) compared to the measurements of a reference analyser (Picarro G2401). The x_{CO_2} signal is recovered despite strong influences from changing pressure.

2 A compact carbon dioxide analyser for airborne platforms

Michell Instruments Ltd., UK) with a measurement uncertainty of 0.1 °C for temperature and 0.2 °C for dew point served as the reference. Reference and sensor under test were placed close to each other and actively ventilated during the measurements.

The pressure sensors were calibrated in a CH3030 chamber (SIEMENS AG, Germany). The reference instrument (Druck DPI 740, General Electric Company, USA) has a measurement uncertainty of 0.26 hPa.

Details of the calibrations are listed in Table 2.1. The correction model for the humidity sensor depends not only on the raw humidity signal, but also on air temperature. It therefore relies on the corrected indication of the temperature sensor.

A potential source of error in the humidity calibrations are the different response times of the chilled-mirror dew point hygrometer and the slower reacting capacitive humidity sensor. We avoid the introduction of a bias by calibrating with slowly varying symmetric humidity patterns, i.e. by using the same rate of change during humidity increase and decrease.

2.6.3 Field calibration

The CO₂ dry air mole fraction reported by COCAP drifts over time (see Sect. 3.5), necessitating periodic calibration. We decided against in-flight calibrations to reduce the system mass, to save space and to have the full flight time available for the measurement of ambient air. Instead we sample two gas standards before and after each flight using the field calibration device described in Sect. 2.3. One of the standards has a CO₂ dry air mole fraction close to clean ambient air (397.57 μmol·mol⁻¹), the other one is enriched with CO₂ (447.44 μmol·mol⁻¹). Both standards consist of natural air collected at the Max Planck Institute for Biogeochemistry in Jena, Germany, i.e. the standards are similar in isotopic composition to the air that we typically measure in the field. This way we avoid isotope related errors that can occur with synthetic air standards (Tohjima et al., 2009). The standards are sampled for 5 minutes each. We discard the first 3 minutes to ensure that the measurement system is well flushed, leaving 2 minutes for averaging. This time span is a compromise between noise reduction (the minimum standard error of the mean would be achieved by averaging over 4 minutes, see Sect. 3.5) on the one hand and consumption of gas standards and time spent for the field calibration (and lost for ambient measurements) on the other.

During data analysis, the calibration curve (see Sect. 2.6.1) is applied to all measurements of COCAP, resulting in a time series of CO₂ dry air mole fraction. Averaging is carried out for each gas standard and each sampling period by calculating the arithmetic mean of the CO₂ dry air mole fraction. Next, “virtual” standard measurements are created by interpolating between the calculated averages linearly in time. Using these virtual standard measurements two correction parameters $a_S(t)$ (slope) and $a_O(t)$ (offset)

are calculated for each point in time between the first and last standard measurement such that the difference between corrected measurement and assigned value vanishes. The corrected CO₂ dry air mole fraction is thus calculated as

$$x_{\text{CO}_2} = a_S(t) \cdot k(s, T, p \dots) + a_O(t) \quad (2.6.6)$$

2.7 Summary of Chapter 2

With COCAP we have developed a self-contained analyser for the measurement of CO₂ dry air mole fraction, temperature, humidity and pressure of ambient air. The analyser is designed for deployment on unmanned aircraft without any dependency on the carrier system. COCAP is typically operated under ambient conditions that change quickly and over wide ranges. These challenging conditions can compromise the accuracy of CO₂ sensors. We ensure COCAP's accuracy by (1) temperature stabilisation, (2) drying of sample air, (3) a calibration curve that includes correction terms for temperature and pressure and (4) by regular field calibrations.

With a volume of $14 \times 14 \times 42 \text{ cm}^3$ and a mass of 1 kg COCAP fits onto small UASs with a take-off mass below 5 kg. It is therefore a cost-effective tool to study carbon dioxide in the lowest 100–1000 m of the Earth's atmosphere. On a multicopter or fixed-wing aircraft COCAP enables measurements at a finer scale than manned aircraft and without restrictions of minimum flight altitude.

3 Tests and validation

3.1 Overview

A measuring instrument can be affected not only by the quantity it is intended to measure, but also by other influencing quantities. If these influencing quantities are known, they can be reduced by design of the instrument or a correction can be applied to the measured values. The influence of humidity and ambient temperature on COCAP are reduced by drying sampled air before measurement and by stabilisation of the internal temperatures. Furthermore, COCAP's sensitivity to the remaining temperature changes and to ambient pressure are corrected for by the calibration curve. The effectiveness of such measures must be verified in experiments before a newly designed instrument can be relied on. Moreover, unexpected influencing quantities can be revealed by tests carried out in an environment that resembles the intended operating conditions of the measuring instrument as closely as possible.

An instrument that is carried by a small UAS can be exposed to rapid changes in temperature and pressure, especially if the flight pattern covers a large range in altitude. Moreover, an instrument on a UAS is subject to vibrations, electromagnetic interferences and fluctuating levels of wind and sunlight. Additionally, testing COCAP under realistic conditions requires the measurement of x_{CO_2} in ambient air with varying composition. Specifically, changes in humidity are desirable to reveal potential problems with the drying of the sample gas. At the same time, changes in CO_2 content allow validation of COCAP's calibration curve and could reveal potential adsorption and desorption of substantial amounts of CO_2 inside the analyser. To provide a reference, another instrument must simultaneously sample the same air that is measured by COCAP. Laser-based analysers are widely used for high-accuracy measurements of greenhouse gases (e.g. Laurent, 2016) and their high precision and stability makes them suited for use as a reference. However, with a mass of more than 10 kg they are too large to fly on any UAS available for this work.

As an intermediate step between stationary indoor testing and UAS flights we integrated COCAP into an instrumented van and took measurements while driving on a road that climbs 700 m from a city into a rural area. We cover this experiment in Section 3.2 and explain how we compare time series from two analysers with different time constants.

3 Tests and validation

Insights gained during the measurements with the instrumented van led to modifications of the thermal control inside COCAP. In order to assess the improved temperature stabilisation, we placed COCAP in an environmental chamber and simulated the changes in ambient pressure and temperature that would typically be encountered during a flight to 1000 m height (Sect. 3.3). Carrying out this experiment in the lab allowed us to measure a standard, i.e. an air sample with known CO₂ dry air mole fraction, during the simulated flights. This facilitates the quantification of COCAP's measurement error by comparing the measured mole fraction to the value assigned to the standard.

However, the simulated flights did not include all disturbances that are present during an actual flight on a UAS. To investigate how well the temperature stabilisation works in presence of vibration, electromagnetic interference, wind and sunlight, we mounted COCAP to a multicopter and performed a flight to a height of 430 m. In Sect. 3.4 the results of this test flight are presented.

The influence of noise, especially of thermal noise generated in electronic circuits, on a measurement can be reduced by averaging over several samples. However, the precision achievable by averaging is limited by drift of the instrument over time, i.e. over long averaging periods the error caused by drift becomes larger than the error caused by noise. We characterised COCAP's noise and drift performance based on Allan deviation, a measure that is explained in Section 3.5.

The final validation experiment for COCAP was a series of flights on board a UAS near the instrumented, 99 m high mast of the ICOS station Lindenberg. This study enabled direct comparison of COCAP's in-flight x_{CO_2} measurements to the high-accuracy measurements taken at different heights at the mast. The study and its results are detailed in Section 3.6.

A summary of our findings in Sect. 3.7 concludes this chapter.

3.2 Measurements with an instrumented van

3.2.1 Experimental setup

We integrated COCAP into the "Mobile Lab" (Pétron et al., 2012), an instrumented van equipped with a laser-based cavity ring-down spectrometer for carbon dioxide, carbon monoxide, methane and water (G2401-m, Picarro Inc., USA). Air was sampled at 3.5 m above street level while driving up and down a road that covers 700 m in elevation (1650–2360 m above sea level). During the drive, COCAP was exposed to the same pressure changes that would occur during a flight at these altitudes. Field calibrations (see Sect. 2.6.3) were carried out by injecting air from cylinders with slightly higher-than-ambient pressure into the sampling line at regular intervals. We carried out the experiment with the Mobile Lab in Boulder, Colorado, USA, on 15 October 2015. The

3.2 Measurements with an instrumented van

drive started in the city, went up Flagstaff Road to a rural area near Flagstaff Mountain and Green Mountain and then the same way back down to the city. During the drive, the weather was mostly sunny and ambient temperature varied between 6 and 13 °C.

At the time of the experiment, the temperature stabilisation described in Sect. 2.2.6 had not yet been fully implemented. The built-in heaters of the CO₂ sensor were active, but no heated air stream was circulating in COCAP's enclosure. Instead, a comparatively slow heater was connected to a metal tube attached to the inlet of the CO₂ sensor. This heater was controlled for a stable gas temperature at the inlet temperature sensor (Sect. 2.2.3).

3.2.2 Compensating for different flushing time of two analysers

As COCAP and the CRDS analyser were connected to the same sampling line, delay and mixing caused by tubing and inlet filter affected them equally. However, the flushing time of the analyser's measurement cells is different, which makes direct comparison of their readings inappropriate. In the following we explain how we handled this issue mathematically.

The flushing process can be described as a convolution of the CO₂ dry air mole fraction at the inlet of the sampling line, $x_{\text{Inlet}}(t)$, with an analyser-specific instrument function $f(t)$:

$$x(t) = (x_{\text{Inlet}} * f)(t) \quad (3.2.1)$$

$$= \int_{-\infty}^{\infty} x_{\text{Inlet}}(t - t') \cdot f(t') dt' \quad (3.2.2)$$

The response $x(t)$ of the analyser is the reported CO₂ dry air mole fraction. Due to causality, $x(t)$ cannot depend on future CO₂ dry air mole fractions at the inlet. Hence, the lower limit of the integration can be set to zero:

$$x(t) = \int_0^{\infty} x_{\text{Inlet}}(t - t') \cdot f(t') dt' \quad (3.2.3)$$

The instrument function $f(t)$ is not known *a priori*, but can be estimated from the response to a step change in $x_{\text{Inlet}}(t)$. Such step changes occurred at the end of calibration measurements when the supply of gas standard into the sampling line was shut off. From the data we found that for both analysers the response $x_{\text{SC}}(t)$ to a step change can be modelled by an exponential decay of the form

$$x_{\text{SC}}(t) = (x_0 - x_{\infty}) \cdot e^{-t/\tau} + x_{\infty} \quad (3.2.4)$$

3 Tests and validation

where x_0 and x_∞ are the CO₂ dry air mole fractions before and after the step change, respectively, and τ is the characteristic time constant of the flushing process, also called the step response time. We determined time constants of 25 s for COCAP and 13 s for the CRDS analyser. To find the function $f(t)$ we differentiate Eq. 3.2.3:

$$\frac{d}{dt}x(t) = \frac{d}{dt} \int_0^\infty x_{\text{Inlet}}(t-t') \cdot f(t') dt' \quad (3.2.5)$$

$$= \int_0^\infty f(t') \cdot \frac{d}{dt} x_{\text{Inlet}}(t-t') dt' \quad (3.2.6)$$

In case of a step change at the inlet, the differentiation yields the Dirac delta function δ , scaled by the height of the step ($x_\infty - x_0$):

$$\frac{d}{dt}x_{\text{SC}}(t) = \int_0^\infty f(t') \cdot (x_\infty - x_0) \cdot \delta(t-t') dt' \quad (3.2.7)$$

$$= (x_\infty - x_0) \cdot f(t) \quad (3.2.8)$$

Rearranging and applying Eq. 3.2.4:

$$f(t) = \frac{\frac{d}{dt}x_{\text{SC}}(t)}{x_\infty - x_0} \quad (3.2.9)$$

$$= \frac{(x_\infty - x_0) \cdot e^{-t/\tau}}{(x_\infty - x_0) \cdot \tau} \quad (3.2.10)$$

$$= \frac{e^{-t/\tau}}{\tau} \quad (3.2.11)$$

This means that the instrument function of either analyser can be described with an exponential decay which has the same time constant as the analyser's step response. For practical reasons, we treat $f(t)$ as equal to zero outside $0 \leq t \leq 5\tau$. Because no carbon dioxide is created or removed inside the analysers, the time integral over $f(t)$ must be equal to one, necessitating normalisation of the truncated response function:

$$f'(t) = \begin{cases} 0 & \text{if } t < 0 \\ \frac{f(t)}{1-e^{-5}} & \text{if } 0 \leq t \leq 5\tau \\ 0 & \text{if } t > 5\tau \end{cases} \quad (3.2.12)$$

Through the measurement process both analysers effectively convolute the x_{CO_2} signal present at the inlet of the sampling line with their respective instrument function. To make the results comparable, we convolute the measurements of each analyser with the

3.3 Simulated flights

instrument function of *the other* analyser. If both measurements were perfect, this would yield identical results because convolution is commutative:

$$x_{\text{COCAP}} * f_{\text{CRDS}} = (x_{\text{Inlet}} * f_{\text{COCAP}}) * f_{\text{CRDS}} \quad (3.2.13)$$

$$= (x_{\text{Inlet}} * f_{\text{CRDS}}) * f_{\text{COCAP}} \quad (3.2.14)$$

$$= x_{\text{CRDS}} * f_{\text{COCAP}} \quad (3.2.15)$$

Here x_{COCAP} and x_{CRDS} are the CO_2 dry air mole fractions measured by COCAP and the CRDS analysers, respectively. Convoluting each analyser's measurement with the instrument function of the other analyser can therefore be viewed as an equalisation of the flushing times of both analysers.

3.2.3 Results and discussion

The temperature inside the van increased from 14 °C to 20 °C during the drive. Despite the substantial changes in ambient conditions, the measurements from both analysers agree to within $2 \mu\text{mol}\cdot\text{mol}^{-1}$ during most of the experiments (Fig. 3.1). Differences are mainly caused by limitations of the simple model for the instrument functions, which become apparent during fast changes in x_{CO_2} , and by sensor noise. They are reduced to less than $1 \mu\text{mol}\cdot\text{mol}^{-1}$ when high-frequency variations are filtered out. Between 9:55 and 10:15 a consistently negative difference of about $-0.8 \mu\text{mol}\cdot\text{mol}^{-1}$ is observed. This difference might be related to sunlight exposure. Other experiments, carried out in the lab under a strong lamp or outside in the sunlight, had also suggested a sensitivity to changes in irradiance. Consequently, we redesigned the temperature stabilisation of COCAP with the aim of a faster response to changing ambient conditions and a more homogeneous temperature distribution inside the enclosure. The solution we came up with was the combination of fan, heater and controller described in Sect. 2.2.6. It was used in all other experiments covered in this and the next chapter.

3.3 Simulated flights

3.3.1 Experimental setup

Three consecutive flights between 0 and 1000 m above sea level (Fig. 3.2 panels a and b) were simulated by placing COCAP in an environmental chamber (CH3030, SIEMENS AG, Germany). Temperature and pressures were controlled to approximately resemble the International Civil Aviation Organization Standard Atmosphere (ICAO, 1993). Each simulated flight had a duration of 20 minutes with 5 minutes ascent and 15 minutes

3 Tests and validation

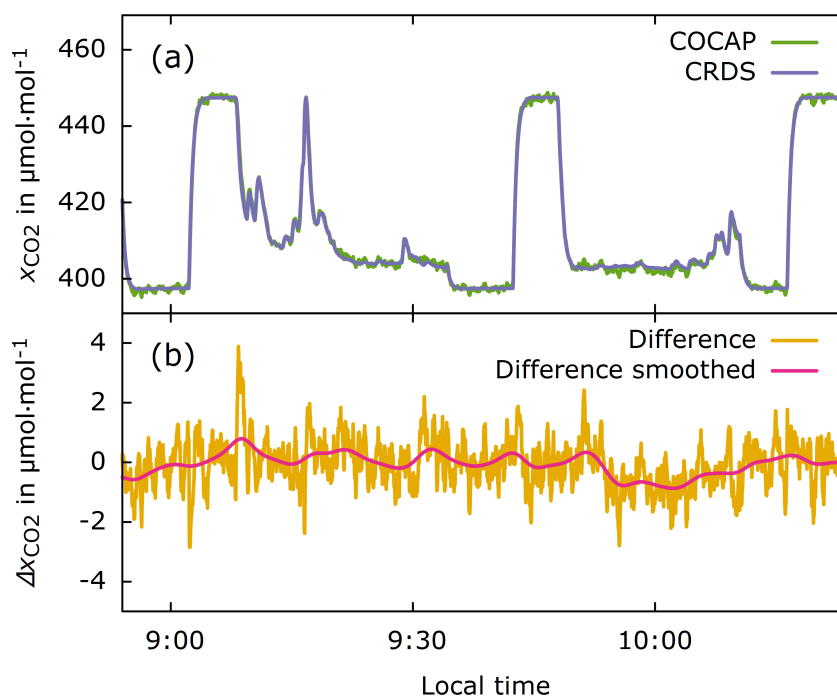


Figure 3.1: (a) CO₂ dry air mole fraction x_{CO_2} of ambient air measured by COCAP and a CRDS analyser during a car drive. The three step-like patterns originate from the field calibration during which two gas standards are sampled. The peak at 9:16 occurred while waiting at a traffic light on a busy street. (b) Difference and smoothed difference of x_{CO_2} measured by COCAP minus x_{CO_2} measured by the CRDS analyser. The smoothing is implemented by convolution with a Gauss window of 200 s full width at half maximum. The measurements of both analysers have been corrected using the field calibrations and the flushing times have been equalised as explained in the text.

3.3 Simulated flights

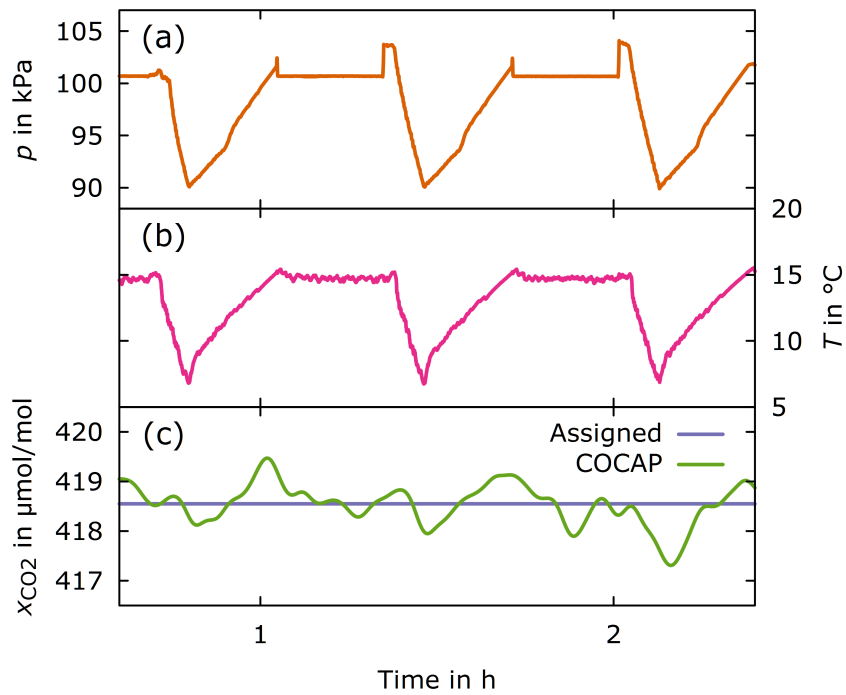


Figure 3.2: Stability test in an environmental chamber. The variations in ambient pressure p and temperature T approximately represent three flights between 0 and 1000 meters above sea level in the International Standard Atmosphere. Air with constant dry air mole fraction of CO_2 was supplied to COCAP from a cylinder. Calibrations were carried out before and after the flights (not shown) using two gas standards ($397.5 \mu\text{mol}\cdot\text{mol}^{-1}$ and $447.4 \mu\text{mol}\cdot\text{mol}^{-1}$). The dry air mole fraction x_{CO_2} measured with COCAP has been smoothed by convolution with a Gauss window of 200 s full width at half maximum in order to reduce the high-frequency noise. The sharp features in pressure were caused by turning the environmental chamber's pressure regulation off after and back on before each flight.

3 Tests and validation

descent. After a 20 minutes break without changes in temperature and pressure this pattern was repeated. Only dry air samples from cylinders were supplied to COCAP, hence no drying cartridge was necessary. Otherwise, the analyser was operated in standard configuration, including pump and flow control. An open split with overflow upstream of the analyser's inlet ensured that air was sampled at the pressure of the environmental chamber at all times. First we measured two gas standards with CO₂ dry air mole fractions of 397.5 $\mu\text{mol}\cdot\text{mol}^{-1}$ and 447.4 $\mu\text{mol}\cdot\text{mol}^{-1}$ for 5 minutes each at 15 °C and 100 kPa. Afterwards, air with 418.6 $\mu\text{mol}\cdot\text{mol}^{-1}$ CO₂ was supplied over a period of two hours while the environmental chamber was simulating three flights as detailed above. Finally, we sampled the two gas standards again for 5 minutes each at 15 °C and 100 kPa. The x_{CO_2} measurement by COCAP is affected by different sources of error: random noise, drift over time, calibration errors and influence of temperature and pressure. We reduced the noise by convoluting the time series with a Gauss window of 200 s full width at half maximum (Fig. 3.2c). A two-point calibration was derived from the standard measurements at the beginning and end of the test and applied to the full time series using linear interpolation in time. This procedure cancels out linear drift over time, but due to the influence of noise on the measurement of the gas standards and non-linearity in the instrument response a calibration error remains. The influence of temperature and pressure was corrected for with the calibration curve described in Sect. 2.6.1.

3.3.2 Results and discussion

The x_{CO_2} time series in Fig. 3.2c exhibits a local minimum whenever pressure and temperature are minimal, with a maximum deviation from the assigned value of the cylinder (418.6 $\mu\text{mol}\cdot\text{mol}^{-1}$) of -1.2 $\mu\text{mol}\cdot\text{mol}^{-1}$ at 2:10 h. This indicates that the calibration curve does not completely eliminate the effect of pressure and temperature changes on the measurement result. The bias of the mean over the whole test, representing the combined effect of the calibration error and changes of the measurement system with temperature and pressure, was -0.03 $\mu\text{mol}\cdot\text{mol}^{-1}$. The standard deviation of the 1 Hz time series before noise reduction was 2.7 $\mu\text{mol}\cdot\text{mol}^{-1}$, the standard deviation after noise reduction was 0.41 $\mu\text{mol}\cdot\text{mol}^{-1}$.

Figure 3.3 shows time series of temperatures measured at different points inside COCAP during the simulated flights. Statistics of these time series are given in Table 3.1. The differences in the observed patterns result from the air circulation inside COCAP's housing: First, heated air from the fan streams along the inlet tube of the CO₂ sensor. Next, it passes the air stream sensor (see Sect 2.2.6). Finally, it reaches the outlet tube and the detector of the CO₂ sensor.

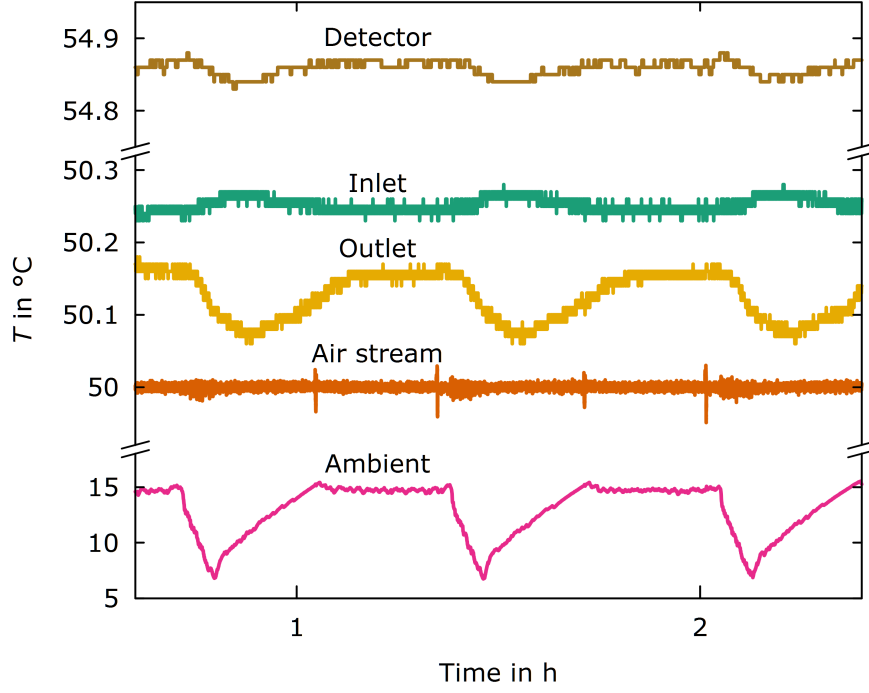


Figure 3.3: Temperatures inside and outside COCAP under simulated flight conditions (depicted in Fig 3.2 panels a and b). The temperature sensors in the detector, inlet and outlet of the CO₂ sensor are uncalibrated, hence they have an unknown offset of up to 1.1 °C. The detector is about 5 K warmer than the other parts (note the broken temperature axis) due to heat transfer from one of the mirrors, which is heated to 55 °C. Ambient temperature is plotted at a different scale as it varies two orders of magnitude more than the stabilised internal temperatures. The spikes in air stream temperature are related to fast pressure changes in the environmental chamber (see Fig 3.2a).

Table 3.1: Mean \bar{T} , standard deviation d and range $T_{max} - T_{min}$ of temperatures under simulated flight conditions.

Sensor	\bar{T} in °C	d in mK	$T_{max} - T_{min}$ in mK
Ambient	12.83	2366	8786
Air stream	50.00	4	79
Inlet	50.25	10	50
Outlet	50.12	32	110
Detector	54.86	10	50

3 Tests and validation

The air stream sensor is part of the control loop and therefore its temperature stays close to the set point of 50 °C. The inlet and outlet temperature sensors measure the temperature of the sample gas, which indirectly reflects the temperature of the air circulation because heat is exchanged through the walls of the inlet and outlet tubes. The temperatures of the outlet exhibits minima whenever the ambient temperature is reduced. This is caused by increased heat transfer from the circulating air to outside COCAP's housing. The inlet shows the inverse behaviour, i.e. increasing temperature under reduced ambient temperature, because it is located between fan and air stream sensor. In an colder environment the air has to be heated more to keep the temperature at the air stream sensor constant, so the temperature at the inlet rises.

The temperature of the detector varied qualitatively similar to that of the outlet because detector and outlet are located close to each other. However, the temperature of the detector is approximately 5 K higher and the amplitude of the temperature variations is roughly three times lower than at the outlet. This is due to the detector's thermal coupling to one of the two mirrors of the CO₂ sensor, which is temperature controlled to 55 °C. Overall, the temperature stabilisation reduces the variability in the internal temperatures by two orders of magnitude compared to the changes in ambient temperature (see Table 3.1).

3.4 Lannemezan flights

The so far highest flight of COCAP on a UAS was carried out in Lannemezan, France, on 20 May 2016 at 15:30 UTC (17:30 local time). COCAP was mounted under a custom-built multicopter (Sensomotion UG, Germany and Ostwestfalen-Lippe University of Applied Sciences, Germany, Fig. S10). Starting from an elevation of 600 m above sea level a maximum height of 430 m was reached. The flight took place under clear sky in a light breeze (2 m · s⁻¹ wind speed). It served as a real-world test of COCAP's temperature stabilisation (Fig. 3.4). While ambient pressure p changed by 5 kPa and ambient temperature T_{Ambient} by 4.5 °C during the flight, the temperature of the air stream at the CO₂ sensor's outlet T_{Outlet} varied by only 0.13 °C and the temperature of the optical detector T_{Detector} by only 0.02 °C. These results demonstrate that the temperature stabilisation functions as expected despite the presence of wind, sunlight, vibration and radio signals.

3.5 Allan deviation of CO₂ dry air mole fraction

The Allan or two-sample variance $\sigma_y^2(\tau)$ is defined as (Allan, 1987)

3.5 Allan deviation of CO₂ dry air mole fraction

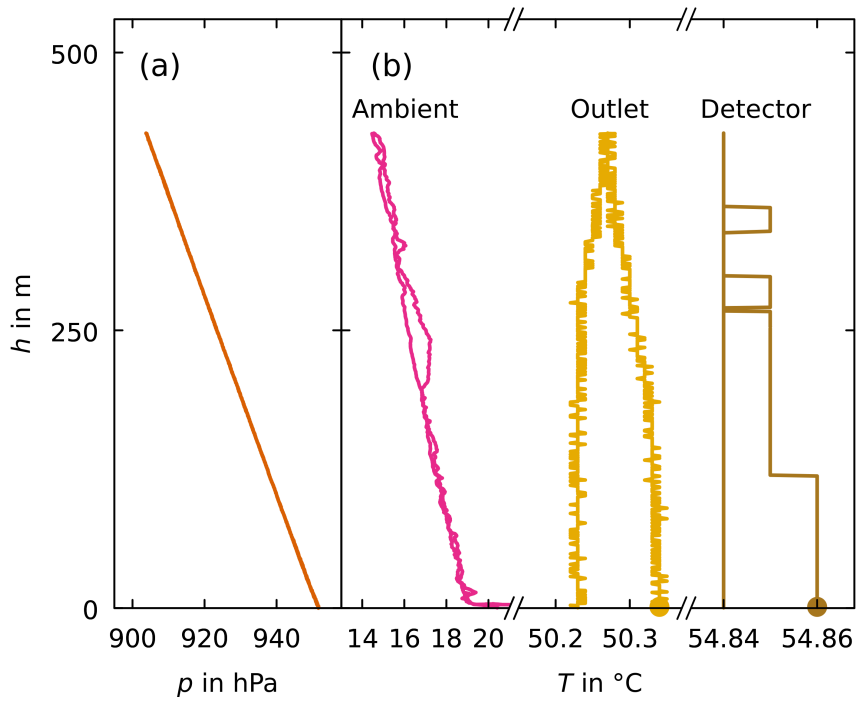


Figure 3.4: Stability of COCAP's internal temperatures during a flight to a maximum height of $h = 430$ m. p is ambient pressure, T is temperature. The temperatures of outlet and detector during take-off are indicated with a filled dot. Note the broken temperature axis and the different scaling used for ambient, outlet and detector temperature.

3 Tests and validation

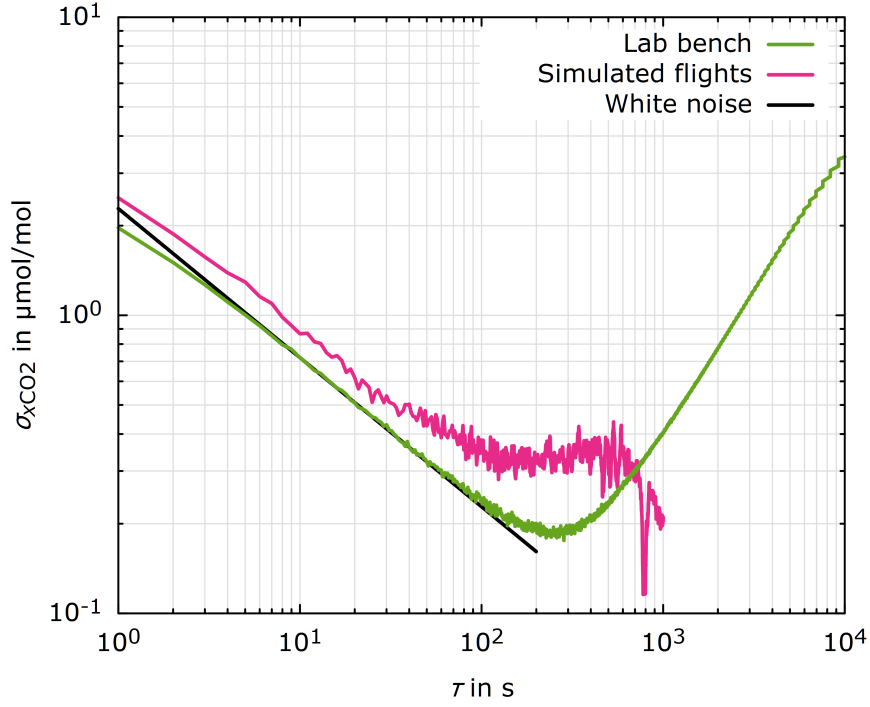


Figure 3.5: Allan deviation $\sigma_{x\text{CO}_2}$ of unfiltered CO_2 dry air mole fraction versus averaging period τ . Air from a cylinder was measured under laboratory conditions and during the simulated flights described in Sect 3.3. The latter is depicted until $\tau = 1000$ s, i.e. one sixth of the length of the time series. The characteristic $-1/2$ slope of white noise is indicated by the black line.

$$\sigma_y^2(\tau) = \frac{1}{2} \langle (\Delta y)^2 \rangle \quad (3.5.1)$$

where Δy is the difference between two consecutive arithmetic means of measurements over periods of τ and the angle brackets denote the expected value. The square root of the Allan variance is called Allan deviation σ_y .

To characterise noise and drift of COCAP we connected the analyser in an open split configuration to a cylinder containing natural air with a CO_2 dry air mole fraction of $384.3 \mu\text{mol}\cdot\text{mol}^{-1}$. This air sample was measured in a lab environment over a period of 24 hours. The Allan deviation of this dataset (Fig. 3.5) reaches a minimum of approximately $0.2 \mu\text{mol}\cdot\text{mol}^{-1}$ at an averaging period of 230 s. For averaging periods shorter than 100 s the curve has a slope of $-\frac{1}{2}$ in the log-log plot, which is characteristic of white noise. At $\tau_c = 1800$ s, the typical time between field calibrations, the Allan deviation is approximately $0.7 \mu\text{mol}\cdot\text{mol}^{-1}$ and dominated by drift. Our correction

3.6 Comparison to the ICOS station Lindenberg

scheme (see Sect. 2.6.3) removes offset and gain errors at the point in time when the field calibrations were carried out and uses linear interpolation between the calibrations. Therefore, the largest uncorrected drift is expected to be lower than $0.4 \mu\text{mol}\cdot\text{mol}^{-1}$, the Allan deviation for $\frac{1}{2}\tau_C = 900$ s. The error caused by noise is lower than $0.4 \mu\text{mol}\cdot\text{mol}^{-1}$ if averaging is performed over an interval of at least 32 s.

Figure 3.5 also shows the Allan deviation of COCAP's x_{CO_2} measurements during the simulated flights described in Sect. 3.3. Forced ventilation and substantial changes in ambient pressure and temperature during the simulated flights lead to an increased Allan deviation compared to the measurements in a lab environment. Estimation of the expected drift for $\frac{1}{2}\tau_C = 900$ s is not feasible based on that dataset due to artefacts which become visible at averaging periods beyond 400 s. What we can say with confidence is that even under simulated flight conditions the Allan deviation is lower than $0.5 \mu\text{mol}\cdot\text{mol}^{-1}$ for averaging periods between $\tau = 40$ s and $\tau = 400$ s.

3.6 Comparison to the ICOS station Lindenberg

3.6.1 Measurement site and flight pattern

The Lindenberg observatory is part of the Integrated Carbon Observation System (ICOS, www.icos-ri.eu) and meets the WMO GAW recommendations for high accuracy atmospheric trace gas measurements (WMO, 2016). The ICOS station Lindenberg (ICOS short name: LIN) is located in the eastern part of Germany ($52^\circ 10' \text{ N}$, $14^\circ 07' \text{ E}$) in a flat, rural area. At LIN a 99 m high mast is equipped with inlets at 2.5 m, 10 m, 40 m and 98 m above ground level. Air is drawn from all inlets continuously, but only one sampling line is analysed at a time. The gas analyser is connected to a different sampling line every five minutes ("quasi-continuous sampling"). It measures carbon dioxide and methane dry air mole fraction.

We mounted COCAP on the same multicopter that was used in Lannemezan (see Sect. 3.4) and carried out a total of 21 flights close to the mast (distance less than 150 m) on 18 and 27 October 2016, using the same setup on both days. During each flight, the multicopter ascended vertically to 100 m above ground level at a climb rate of $0.5 \text{ m}\cdot\text{s}^{-1}$, followed by a descent at a rate of $2 \text{ m}\cdot\text{s}^{-1}$. The same pattern was then repeated at approximately 70 m distance from the first ascent. Each flight lasted 9 minutes and the two ascents were separated in time by 4 minutes. The only exception was flight 7, which we had to abort after the first ascent due to a technical problem with the multicopter.

In flight, the multicopter mixes the air around it. To avoid artefacts in our measurements caused by this mixing, we sampled air from 70 cm above the rotors. Furthermore, for the analysis detailed below we used only the data collected during the ascents, i.e. when the UAS was flying into and sampling undisturbed air. In each flight, we carried

3 Tests and validation

out the second ascent upwind of the first ascent, which ensured that the mixing caused by the first ascent did not degrade the measurements during the second ascent.

On the evening of 18 October, the sky was cloudy with occasional drizzle, the wind speed was low ($1.5 \text{ m}\cdot\text{s}^{-1}$), and the lowest 100 meters of the atmosphere were weakly stable. On the early evening of 27 October, conditions were similar, but without precipitation. After 21:00 local time on 27 October, the sky cleared up, followed by the formation of radiation fog.

3.6.2 Results and discussion

At the mast's 2.5 and 10 m inlets, the variability of the CO_2 dry air mole fraction was larger than above due to respiration fluxes from soil and vegetation that were intermittently mixed upwards by turbulence. This high variability makes these levels less suitable for comparison to COCAP, as our flights were not synchronised with the sampling at the mast. We were not allowed to fly higher than 100 m, hence few measurements were taken at the same height as or above the 98 m inlet. We therefore focus our comparison on the 40 m inlet of the mast.

After applying the calibration curve to the measurements of COCAP's CO_2 sensor, we corrected for its temporal response by deconvolution. For each ascent, we then calculated the arithmetic mean of the measurements taken between a height of 30 and 50 m. Figure 3.6 shows these means together with the LIN measurements at 40 m plotted against time. Overall, there is good agreement between COCAP and LIN. The variability in COCAP's data is higher, likely caused by a low-pass effect of the mast's sampling system. Further differences are due to the measurements being taken 100–150 m apart and at different times. Finally, instrument noise leads to discrepancies. All these factors should have a zero mean effect, whereas a consistent bias between COCAP and the ICOS station Lindenberg would indicate a problem with the calibration. A change of bias over time would suggest instrument drift.

To better assess the presence of bias, we averaged the measurements from the mast's 40 m inlet over a period starting 20 min before and ending 20 min after the respective flight (Fig. 3.7a). We then calculated the difference between the measurements by COCAP and LIN (Fig. 3.7b). Additionally, we estimated the noise level of COCAP's CO_2 sensor. The correction for COCAP's finite time response by deconvolution has the side effect of amplifying high frequency electronic noise. Therefore, we did not use the Allan deviation of the data described in Sect 3.5, but calculated the Allan deviation of the deconvoluted time series. During each ascent, the multicopter climbed from 30 to 50 m height in approximately 40 s. In analysing a period during which a standard gas was measured, we found an Allan deviation of $1 \mu\text{mol}\cdot\text{mol}^{-1}$ for $\tau = 40 \text{ s}$. This number is represented as error bars in Fig. 3.7b.

3.6 Comparison to the ICOS station Lindenberg

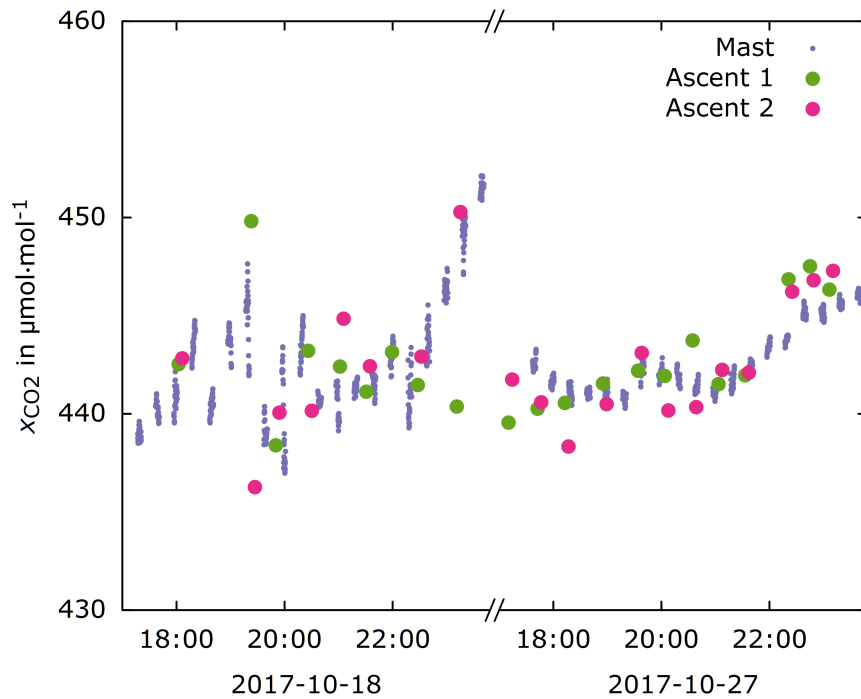


Figure 3.6: Comparison between the CO₂ dry air mole fraction x_{CO_2} measured by CO-CAP and by the instrumented mast at LIN. Large dots represent calibrated measurements taken by COCAP during the ascents at a height of (40 ± 10) m, small dots are measurements from the LIN mast's 40 m inlet. Times are in local time (UTC+2). The sun set at 18:02 local time on 18 October and at 17:43 local time on 27 October. The gaps in the station data are due to the measurement of other inlets and working tanks at those times.

3 Tests and validation

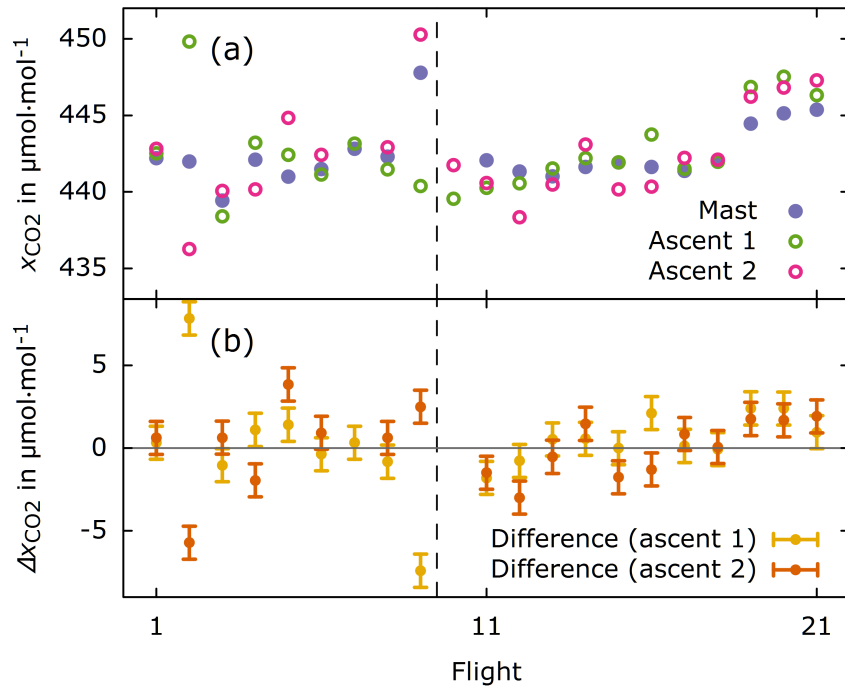


Figure 3.7: (a) Data from COCAP are same as in Fig. 3.6. Measurements from the mast's 40 m inlet have been averaged over a period that starts 20 min before and ends 20 min after the respective flight. No measurements from the mast are available for flight 10 because calibration cylinders have been measured at this time. (b) x_{CO_2} measured by COCAP minus x_{CO_2} measured by LIN. Error bars indicate the noise level of COCAP's CO₂ sensor after deconvolution (see text). Flights 1 through 9 were carried out on 18 October, flights 10 through 21 on 27 October (indicated by dashed vertical line).

3.6 Comparison to the ICOS station Lindenberg

Table 3.2: Mean of the difference between COCAP’s CO₂ dry air mole fraction measurements x_{COCAP} and the corresponding measurements by LIN x_{LIN} (± 1 standard error). Subsets of COCAP’s measurements are also analysed.

COCAP measurements	$\overline{x_{\text{COCAP}} - x_{\text{LIN}}}$ in $\mu\text{mol}\cdot\text{mol}^{-1}$
All	0.23 ± 0.45
18 October	0.16 ± 0.85
27 October	0.28 ± 0.49
All first ascents	0.39 ± 0.66
All second ascents	0.06 ± 0.52

Table 3.3: Statistical tests for bias. Here x denotes measurements by COCAP and the index defines a subset: ‘A’ for all measurements, ‘18’ and ‘27’ for 18 and 27 October, respectively, and ‘A1’ and ‘A2’ for first and second ascent, respectively. $D(x)$ represents the difference between x and the corresponding measurements by LIN. An overline denotes the arithmetic mean.

Null hypothesis	Statistical test	Test result p
$\overline{D(x_C)} = 0$	Welch’s t -test	0.75
$\overline{D(x_{18})} = \overline{D(x_{27})}$	Welch’s t -test	0.72
$\overline{D(x_{A1})} = \overline{D(x_{A2})}$	Student’s t -test	0.75

Table 3.2 contains the mean difference between the measurements by COCAP and LIN. A bias of zero lies within one standard error of the mean difference. This is also true for both nights considered individually and for both ascents of all flights considered individually. Table 3.3 lists the results of statistical tests of three hypotheses: (1) no bias between COCAP and LIN, (2) no change in the mean difference between COCAP and LIN from 18 October to 27 October and (3) no change in the mean difference between COCAP and LIN from the first to the second ascents. None of the hypotheses was rejected ($p > 0.7$ in all cases).

The physical connection between COCAP and the multicopter did not include a dedicated shock absorber (see Fig. S10). Although COCAP’s plastic foam housing and the flexibility of the mounting straps provided limited mechanical isolation, sudden movements and vibrations of the multicopter due to turbulence, rotor unbalance and flight manoeuvres have been partially transmitted to the measurement system. In theory, these mechanical disturbances could deteriorate the accuracy of the CO₂ measurements, e.g. by causing misalignment of the optical bench of the CO₂ sensor. The data collected during the flights at LIN, however, do not exhibit increased noise levels or instrument

3 Tests and validation

drift compared to data collected on the ground, suggesting that the movements and vibrations did not degrade COCAP's performance.

3.7 Summary of Chapter 3

We have characterised COCAP's performance in a range of experiments in the lab and in the field. When high-frequency noise is filtered out, COCAP's measurements of CO₂ dry air mole fraction were found to deviate from a reference by not more than 1.2 $\mu\text{mol}\cdot\text{mol}^{-1}$ during simulated flights and by not more than 1 $\mu\text{mol}\cdot\text{mol}^{-1}$ during deployment in an instrumented van. During three simulated and one actual flight COCAP's improved temperature stabilisation kept the variation of internal temperatures one to two orders of magnitude lower than the variation in ambient temperature. A flight on board a multicopter demonstrated that the temperature stabilisation is robust against wind, vibrations and electromagnetic interference. The Allan deviation plot of a 24 h long measurement in the lab suggests that the error caused by noise and drift is lower than 0.4 $\mu\text{mol}\cdot\text{mol}^{-1}$ if the measurements are averaged over at least 32 s and calibrations are carried out every 30 min. In a comparison to the ICOS station Lindenberg we found no indication of (1) calibration problems, (2) uncorrected drift of COCAP between two measurement days, (3) drift of COCAP during flight or (4) degradation of COCAP's accuracy due to vibrations and sudden movements of the multicopter.

Altogether, our results show that COCAP takes reliable measurements of CO₂ dry air mole fraction even under the challenging environmental conditions encountered on board unmanned aircraft.

4 Using COCAP to estimate nocturnal fluxes

4.1 Nocturnal boundary layer budgets

On the ecosystem level, sources and sinks of carbon dioxide and methane are commonly quantified using the eddy covariance (EC) technique (Baldocchi, 2003). By correlating high-frequency (typically 10–20 Hz) measurements of gas concentration with equally fast measurements of the three-dimensional wind vector, eddy covariance provides a direct measurement of vertical tracer flux. This approach works well at daytime when the air is turbulently mixed. However, EC measurements often underestimate nighttime fluxes (Goulden et al., 1996; Gu et al., 2005). This is related to the stable stratification that often develops close to the surface at night. Stable conditions violate assumptions underlying the EC technique: firstly, fluxes are not transported predominantly by turbulence as opposed to advection and secondly, in case of sporadic turbulent events in an otherwise stable layer, the assumption of stationarity is not justified. Despite large efforts, there is currently no final solution how to obtain reliable measurements of nighttime fluxes using the EC technique (Gu et al., 2005; Aubinet et al., 2010; Hayek et al., 2018).

Daytime NEE consists of photosynthetic uptake and release of carbon through respiration. Nighttime NEE is governed by respiration only, as photosynthesis cannot take place without light. Photosynthetic uptake and total respiration fluxes have similar magnitude, but opposite sign. Therefore, even slight underestimation of nocturnal respiration can result in a considerable overestimation of an ecosystem's long-term carbon uptake. Furthermore, daytime fluxes are often partitioned into photosynthetic uptake and respiration using methods that rely on the nighttime measurements (Wohlfahrt and Galvagno, 2017). Errors in the nocturnal fluxes might compromise this partitioning.

The nighttime problem of EC measurements calls for complementary methods to quantify and potentially correct for the errors. Biometric approaches, including enclosure-based methods, plant growth assessment and stock inventories, are often employed to obtain independent estimates for NEE (Goulden et al., 1996; Wilson and Baldocchi, 2001; Campioli et al., 2016). However, these methods quantify the exchange of carbon on a much smaller spatial scale than EC measurements. The chambers used for determining soil respiration typically cover an area of less than one square meter, while

4 Using COCAP to estimate nocturnal fluxes

the EC technique is sensitive to fluxes from an area of 10^4 – 10^6 m², depending on the site and on meteorological conditions (Chen et al., 2009). Given these different scales, comparing NEE values obtained using different methods is difficult. Inhomogeneities in the ecosystem under study, such as spatial variability of soil properties (e.g., texture, carbon content, nitrogen content), soil environmental conditions (e.g., soil temperature and moisture) or plant community composition can lead to biases in the comparison.

In the absence of a method with a sensitivity area similar to the EC technique, larger-scale flux estimates are the next best choice to better constrain the errors of EC measurements. Nocturnal boundary layer (NBL) budgets, first described by Choulaton et al. (1995) and Denmead et al. (1996), provide such estimates. The NBL budget method makes use of the stable stratification at night, which can act as a flux-integrating enclosure. During clear nights, the emission of thermal radiation cools down the Earth's surface much faster than the air, owing to the surface's higher emissivity. An inversion layer forms, inhibiting exchange of air between the stable NBL and the neutral residual layer above (Stull, 1988, p. 15). Any tracer emitted from the surface into the atmosphere is therefore accumulated within the NBL. By measuring the rate of accumulation, the tracer flux can be estimated.

Different setups have been used for NBL budgeting. Acevedo et al. (2004) measured CO₂ dry air mole fractions at a 12 m tower, sampling only the lowest parts of the NBL. Although they did not sample the whole layer, they were able to create a budget by determining an effective accumulation height from either heat flux or balloon-borne humidity and temperature measurements and assuming a uniform accumulation rate of CO₂ up to this height. Winderlich et al. (2014) used CO₂ and CH₄ dry air mole fraction measurements at 6 heights on a 301 m tall tower, yielding profiles that encompass the whole NBL during most nights. Often the NBL budget method is applied without a tower. A tethered balloon can lift a 100–300 m long hose through which a ground-based gas analyser samples air from different heights (Choulaton et al., 1995; Denmead et al., 1996; Culf et al., 1999). Alternatively, a light analyser can be carried by the tethered balloon directly (Pattey et al., 2002).

Despite providing unique information, the NBL budget method has been applied only infrequently in recent years. This might be related to the cost and operational limits of towers and tethered balloons. Unmanned aircraft systems (UAS) could make the NBL budget method more accessible. UAS with payload capabilities on the order of 1 kg are now available for few thousand Euros. When equipped with lightweight trace gas analysers and meteorological sensors they have the potential to probe the NBL with large flexibility at low cost. Multicopters are a particularly attractive type of UAS for this kind of study, because their vertical take-off, vertical landing and hovering capability makes them easy to operate in a range of environments.

4.2 Site and instrumentation

However, the air movement caused by a UAS can disturb the NBL and thereby compromise the measurements. A reliable NBL budget can be created only if this issue is addressed. A second challenge is not specific to UAS, but common to all NBL budgets: the area contributing to the budget depends heavily on the meteorological conditions and can extend far from the point of measurement. For a given time and site this footprint cannot be influenced by experimental design. Nevertheless, knowledge of the footprint is beneficial for the data analysis and interpretation of the results. In earlier NBL studies, this topic has received only basic treatment (Culf et al., 1999) or was ignored altogether.

To assess the suitability of UAS as measurement platforms for the creation of NBL budgets we carried out a proof of concept study. We deployed a carbon dioxide analyser on a multicopter and repeatedly sampled vertical profiles of the NBL during two nights in July 2016 as part of the ScaleX 2016 campaign in Fendt, Germany. In the following, we report on this study and present our findings. Section 4.2 is a description of the site and the available ground-based instrumentation, the airborne measurement system and the unmanned aircraft. In Section 4.3 we explain how we dealt with the disturbance caused by the UAS, which post-processing steps we carried out and how we created the NBL budget. Furthermore, we delineate how a Lagrangian transport model can be applied to identify which areas contribute to the budget, i.e. how to determine the footprint of our flux estimates. In Section 4.4 we present and discuss the profiles taken by the UAS, the fluxes obtained from the NBL budget and a summary of the footprint analysis. We compare our observations to references and assess the robustness of our flux calculation. In Section 4.5 we summarise the merits and experimental challenges of our approach.

4.2 Site and instrumentation

4.2.1 Fendt site

The Fendt site is located in southern Germany in the Alpine Foreland (Figure 4.1) at 11.060°N 47.833°E (WGS84), 600 m above mean sea level. The site lies in a flat valley bordered by a gentle slope to the east and a steep slope leading to a 100 m higher plateau to the west. The valley floor is dominated by pasture and some crops, while the slopes to the east and west are covered with coniferous and mixed forest, respectively. Fendt belongs to the district Weilheim–Schongau, which has a population density of 139 km⁻² (Statistisches Bundesamt (Destatis), 2018, 35th percentile of all districts in Germany).

Five kilometres south-west of the Fendt site lies an isolated, 988 m high mountain, the “Hoher Peißenberg”. Close to its summit the German Weather Service (Deutscher Wetterdienst DWD) operates the Meteorological Observatory Hohenpeißenberg (MOHP) and the ICOS station Hohenpeißenberg (HPB).

4 Using COCAP to estimate nocturnal fluxes

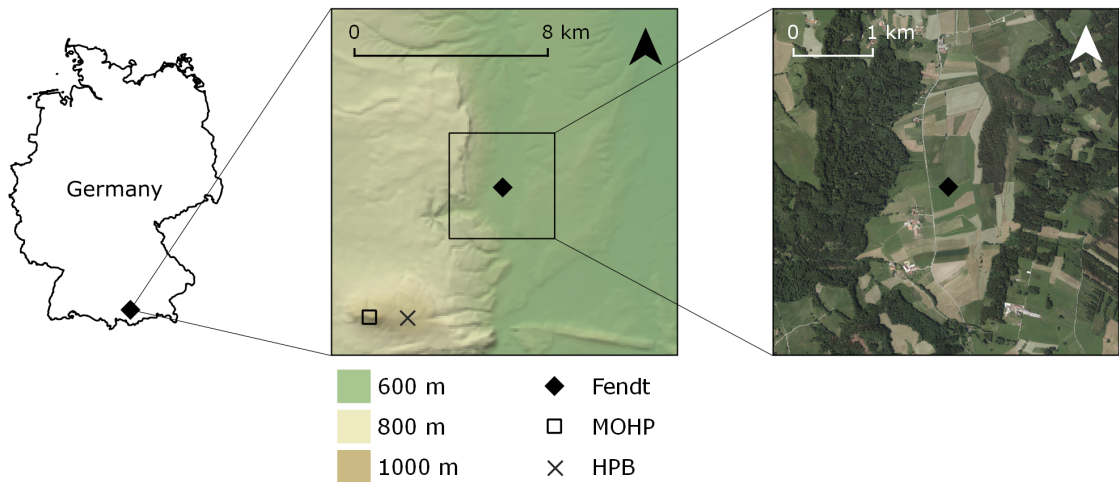


Figure 4.1: Location, topography and aerial image of the Fendt site and its surroundings. MOHP is the Meteorological Observatory Hohenpeißenberg, HPB is the ICOS station Hohenpeißenberg. Digital elevation model and aerial imagery by Bayerische Vermessungsverwaltung, www.geodaten.bayern.de.

4.2.2 Ground-based instrumentation

Fendt is part of the TERENO (Terrestrial Environmental Observatories) network and therefore extensively instrumented. For a detailed description see Wolf et al. (2017) and Zeeman et al. (2017). In the following, we list only those instruments that produced the data presented in this chapter.

During the ScaleX 2016 campaign, CO₂ dry air mole fraction at 1, 3 and 9 meters above ground level was measured with a cavity ring-down spectrometer by successive sampling of air through three inlets installed at a 9 m high mast. Each inlet was sampled once every 7.5 min, with occasional interruptions due to calibrations and other measurements. An EC system installed at 3.5 m height (Zeeman et al., 2017) quantified the turbulent exchange of CO₂. Air temperature and upward as well as downward radiation were measured at 2 m height. Two sets of automated chambers were operated to determine the total NEE or respiration flux of grass and soil. One set comprised four LI-8100 long-term chambers (LI-COR, Lincoln, NE, USA), two with clear enclosure for measuring NEE and two with opaque enclosure for measuring respiration. All four chambers covered an area of 317.8 cm² and will be referred to as “small chambers” from here on. The other set consisted of 5 custom-built opaque chambers covering an area of 2500 cm², referred to as “big chambers” hereafter. All the instruments mentioned so far

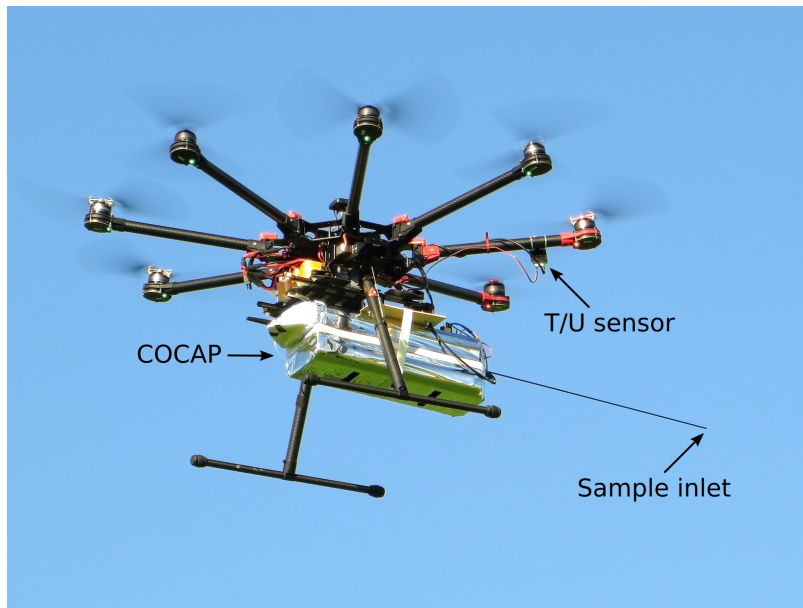


Figure 4.2: COCAP carried by a multicopter during the ScaleX 2016 campaign. The position of the sample inlet for the CO₂ measurement and of the temperature and humidity sensor board are indicated.

were located close to each other and our UAS flew within 200 m horizontal distance to each of them.

Besides the on-site instruments we use two more data sources for our analysis. One is the observation of cloudiness at the Meteorological Observatory Hohenpeißenberg, recorded every hour either by a person or an automated instrument. We consider these 5 km distant measurements representative for Fendt, with a potential time lag on the order of 1 h in case of synoptic events. The second non-local data source is the greenhouse gas monitoring system at the ICOS station Hohenpeißenberg, situated at 934 m above mean sea level. We use its measurements of the CO₂ dry air mole fraction at 131 m tower height, i.e. at 460 m above the Fendt site.

4.2.3 Airborne payload

For the study presented here, temperature, pressure, relative humidity and CO₂ dry air mole fraction of ambient air were measured using COCAP (see chapter 2). COCAP was mounted below the multicopter. Air samples for the measurement of carbon dioxide dry air mole fraction were drawn from an inlet placed 30 cm below and 20 cm to the side of the rotors (Figure 4.2). The temperature and humidity sensor board, requiring strong ventilation for fastest response, was placed directly below one of the rotors. The sensor

4 Using COCAP to estimate nocturnal fluxes

for ambient pressure was located inside COCAP's housing, which was not hermetically sealed and therefore in equilibrium with ambient pressure.

4.2.4 Unmanned aircraft

During ScaleX 2016 COCAP was deployed on an S1000 multicopter (SZ DJI Technology, China) controlled by a Pixhawk autopilot (3D Robotics, Berkeley, CA, USA) running the ArduPilot APM:Copter V.3.3.3 Firmware. Take-off mass of the whole system was 8 kg. The multicopter was powered by three lithium polymer batteries with a voltage of 22.2 V and a capacity of 5000 mAh each, achieving a maximum flight time of 12 min. Our special flight permit included nighttime flights, but because the take-off mass of our UAS exceeded 5 kg, all flights were limited to a maximum height of 150 m.

4.3 Methods

4.3.1 Disturbance by the UAS

A multicopter as a rotary-wing aircraft counterbalances gravity by accelerating air downwards through the movement of its rotors. The resulting displacement of air can interfere with in situ measurements, because air might be sampled at a location where it would normally not reside. In addition, volumes of air originating from different locations can be mixed together.. The greater the displacement and mixing caused by the UAS, the greater is the potential impact on e.g. the measurement of a gradient. Air movement below and above the rotors is not symmetric: below a rotor, air is pushed downwards as a directed stream with high speed. In contrast, the air flow towards the rotor comes from different directions and has lower speed. The reader can easily confirm this with a fan or a hair dryer: while the outflow of air can be felt meters away, the inflow is hard to sense even near the rotor.

In view of the asymmetric flow pattern we expect that during ascent of the UAS air parcels are measured with negligible displacement from their undisturbed location. During descent, however, the sensors are moved into a volume that potentially has been flushed with air originating from several meters above. During hovering at a fixed location or during purely horizontal movement, the sensors might reside in a partially closed flow loop that extends below and aside the multicopter, effectively measuring a mixture of air from different locations.

For the study presented here, flying near the ground can have a particularly strong influence on the measurements for three reasons. Firstly, downward motion of the air stops at the ground and displaced air must move laterally or upwards, making a fast flow path back to the UAS more likely. Secondly, in our nighttime experiments the air

near the ground is stably stratified. Therefore, air pushed downwards by the rotors experiences a restoring upward force, increasing the chance that closed flow loops form. Thirdly, the strongest gradients in temperature and CO₂ dry air mole fraction are present close to the ground, hence even a small displacement of air can have a large effect on the measured values.

In case of considerable horizontal air speed, due to either wind or horizontal flight, the rotor-induced airflow should have a smaller effect on measurements because the sampling system is moving away from air that has been displaced. We investigated this effect by flying horizontally at different speeds over a homogeneous meadow (see Section 4.4.4).

Based on the considerations above and the data presented in Sections 4.4.3 and 4.4.4 we create the NBL budget only from those measurements that were taken during ascent of the multicopter. The sensitivity of the NBL-derived fluxes to inclusion of hover and descent data is discussed in Section 4.4.5. We discard COCAP x_{CO_2} data collected below 9 m height for the calculation of the NBL budget. Instead, the lowest part of the x_{CO_2} profile is defined by the stationary measurements at the 9 m mast at 1, 3 and 9 m height. Pressure and temperature at these levels are interpolated from COCAP's measurements. During flight, the horizontal distance between COCAP and the 9 m mast was lower than 150 m at any time. Hence, we do not expect pronounced horizontal gradients in x_{CO_2} between the measurement locations. In Sect. 4.4.6 the effect of the replacement with stationary measurements on the mean and spread of the derived fluxes is discussed.

4.3.2 Correction for response time of sensors

On a moving platform the finite response time of sensors can be a source of measurement error, as the response time distorts the attribution of data points to time and location. COCAP's pressure and temperature sensors are fast enough for this effect to be neglected, but both the humidity and the CO₂ sensor require correction.

The response of a capacitive humidity sensor can be expressed as (Miloshevich et al., 2004)

$$\frac{dU_m}{dt} = a_U(U_a - U_m). \quad (4.3.1)$$

U_a and U_m are ambient and measured relative humidity, respectively. The coefficient a_U is inversely related to the sensor's response time and might be temperature-dependent. Solving Equation 4.3.1 for U_a provides a simple way to compute true humidity from measurements. We use a 4th order Savitzky-Golay filter (Savitzky and Golay, 1964) with a length of 15 samples to compute $\frac{dU_m}{dt}$ while keeping high-frequency noise at an acceptable level. The coefficient $a_U = 14$ s was determined by an optimisation that

4 Using COCAP to estimate nocturnal fluxes

minimises the difference between the corrected humidity profiles for ascent and descent. We tested a linear and quadratic dependence of a_U on ambient temperature, but found no improvement that would justify the additional degrees of freedom in the model.

The response of COCAP's CO₂ sensor is more complex. Its response to step changes in CO₂ dry air mole fraction can be approximated as

$$x_{SC}(t) = \begin{cases} x_0 & \text{if } t < t_d \\ a_C(x_0 - x_\infty)e^{(t_d-t)/\tau_1} + (1 - a_C)(x_0 - x_\infty)e^{(t_d-t)/\tau_2} + x_\infty & \text{if } t \geq t_d. \end{cases} \quad (4.3.2)$$

Here x_0 and x_∞ denote the CO₂ dry air mole fraction before and infinitely long after the step change, respectively, and t_d is the sensor's dead time.

We determined the parameter a_C , the dead time t_d as well as the time constants τ_1 and τ_2 from experimental data collected in the field. With COCAP running in flight configuration, i.e. with the inlet tube attached, we connected a tube with gas flowing from a cylinder. We observed a dead time of $t_d = 5$ s between making the connection and the first change of COCAP's reading. The remaining parameters were found by least-squares regression of Equation 4.3.2 to the data. In our setup, τ_1 was equal to 27 s and τ_2 equal to 3.2 s.

Ignoring noise and calibration error, any CO₂ signal x_a is reported by COCAP as the convolution of x_a with the CO₂ sensor's instrument function f (see chapter 2):

$$x_m(t) = (x_a * f)(t) \quad (4.3.3)$$

$$\text{with } f = \begin{cases} 0 & \text{if } t < t_d \\ \frac{1}{x_\infty - x_0} \cdot \frac{dx_{SC}}{dt} & \text{if } t \geq t_d. \end{cases} \quad (4.3.4)$$

As x_{SC} is known from experiment, f can be calculated. The ambient signal x_a can be recovered from the measured signal x_m by deconvolution (Figure 4.3). We carried out the deconvolution in Fourier space where it is equal to a division. In the numerical implementation it is important to discretise f in a way that does not underestimate the slope of f between the time steps t_d and $t_d + \Delta t$, because doing so would lead to a strong enhancement of the noise during the deconvolution of x_m with f . The opposite error, i.e. overestimating the slope between t_d and $t_d + \Delta t$, is less critical and just results in a slight smoothing.

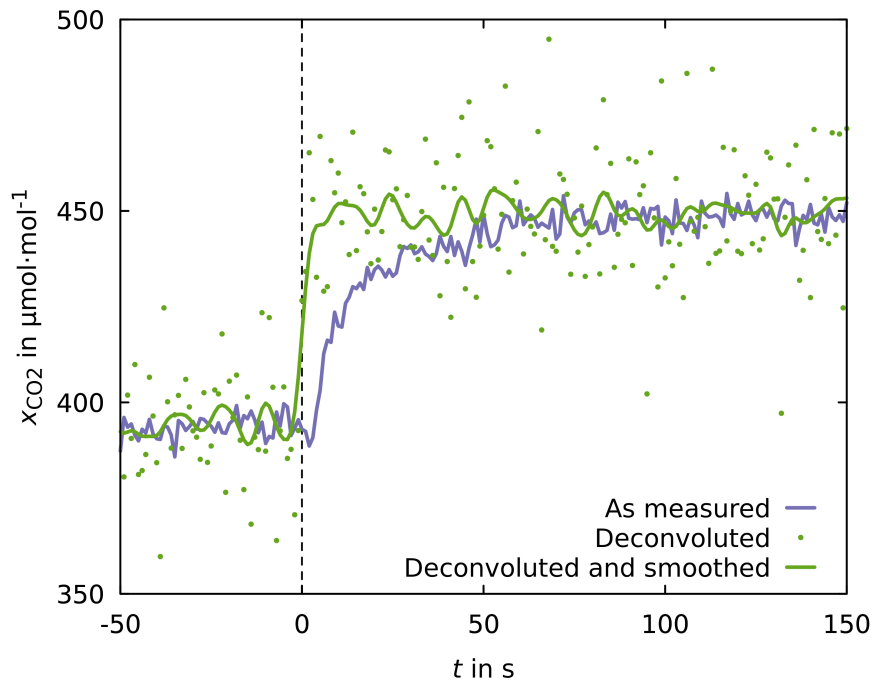


Figure 4.3: Response of COCAP to an abrupt change in CO_2 dry air mole fraction x_{CO_2} at the inlet at time $t = 0$ s. The measured signal reveals a dead time of 5 s of the sampling system. Furthermore, the step change in x_{CO_2} is smoothed out. Both effects are removed by deconvolution at the cost of higher noise. Smoothing the deconvoluted signal reduces the noise with only minor impact on the time response. Smoothing was carried out by convolution with a Gaussian of 5 s full width at half maximum (FWHM).

4 Using COCAP to estimate nocturnal fluxes

4.3.3 Calculation of the NBL budget

For a parcel of air in the atmosphere the following continuity equation holds (Leuning, 2004, Equation 6.2):

$$E = \frac{\partial c}{\partial t} + \nabla \cdot (c \vec{u}) \quad (4.3.5)$$

$$= \frac{\partial c}{\partial t} + c(\nabla \cdot \vec{u}) + u \frac{\partial c}{\partial l_1} + v \frac{\partial c}{\partial l_2} + w \frac{\partial c}{\partial z}. \quad (4.3.6)$$

Here E is the strength of a volume source (or sink) of carbon dioxide (in units $\mu\text{mol} \cdot \text{m}^{-3} \cdot \text{s}^{-1}$), c is the concentration of carbon dioxide and t denotes time. The components u , v and w of the wind vector \vec{u} point towards east (l_1 -direction), towards north (l_2 -direction) and upwards (z -direction), respectively. Molecular diffusion is neglected. Due to continuity of the air flow, the term $c(\nabla \cdot \vec{u})$ equals zero. If we follow an air parcel as it is transported by horizontal winds, those terms that contain a horizontal wind component vanish as well and Equation 4.3.6 is reduced to

$$E = \frac{\partial c}{\partial t} + w \frac{\partial c}{\partial z}. \quad (4.3.7)$$

Now we integrate vertically over those air parcels that form a vertical column over our site at the time of measurement (at earlier or later points in time, the air parcels are not aligned in a vertical column, unless the wind vector is equal at all heights):

$$\int_0^{z_t} E dz = S = \int_0^{z_t} \frac{\partial c}{\partial t} dz + \int_0^{z_t} w \frac{\partial c}{\partial z} dz. \quad (4.3.8)$$

For our measurements, we choose $z_t = 125$ m, so all biotic sources of carbon dioxide are within the column and S represents NEE.

Between a reference time t_0 (see below) and the time of a flight t_F the column has accumulated

$$\int_{t_0}^{t_F} S dt = \int_{t_0}^{t_F} \int_0^{z_t} \frac{\partial c}{\partial t} dz dt + \int_{t_0}^{t_F} \int_0^{z_t} w \frac{\partial c}{\partial z} dz dt \quad (4.3.9)$$

$$= \int_0^{z_t} c(z, t_F) dz - \int_0^{z_t} c(z, t_0) dz + \int_{t_0}^{t_F} \int_0^{z_t} w \frac{\partial c}{\partial z} dz dt. \quad (4.3.10)$$

Dividing the accumulated amount of CO₂ by $t_F - t_0$ yields NEE averaged over this time span, denoted \bar{S} :

$$\frac{\int_{t_0}^{t_F} S dt}{t_F - t_0} = \bar{S} = \underbrace{\frac{\int_0^{z_t} c(z, t_F) dz - \int_0^{z_t} c(z, t_0) dz}{t_F - t_0}}_{(A)} + \underbrace{\frac{\int_{t_0}^{t_F} \int_0^{z_t} w \frac{\partial c}{\partial z} dz dt}{t_F - t_0}}_{(B)}. \quad (4.3.11)$$

Term A represents the enhancement in CO₂ concentration and term B the vertical exchange of CO₂. We choose t_0 as the time when the surface radiation balance becomes negative, i.e. the time when the stable NBL starts to form. A positive \bar{S} means emission of CO₂ from the surface into the atmosphere.

The CO₂ concentration c can be calculated from CO₂ dry air mole fraction x_{CO_2} , air temperature T and dry pressure p_d using the ideal gas constant R (Foken et al., 2012, p. 5):

$$c = \frac{p_d}{RT} x_{\text{CO}_2}. \quad (4.3.12)$$

As COCAP measures x_{CO_2} , T , p and relative humidity U , the integral $\int_0^{z_t} c(z, t_F) dz$ in Equation 4.3.11 term A is readily computed. However, each air parcel is sampled only once, at the time t_F when it passes the Fendt site. In order to evaluate the second integral in term A, $\int_0^{z_t} c(z, t_0) dz$, we assume horizontal and vertical homogeneity of the CO₂ dry air mole fraction at the time t_0 , i.e. $x(t_0)$ is assumed to be independent of l_1 , l_2 and z within the spatial domain relevant for our experiments. Thus we can calculate the second integral from the measurement of a different column at Fendt at t_0 .

Note that this is a weaker assumption than the horizontal homogeneity of the CO₂ concentration *in the NBL* presumed in other studies (Choularton et al., 1995; Culf et al., 1999; Acevedo et al., 2004). All natural environments exhibit a certain horizontal heterogeneity in S . The sign of the daytime CO₂ flux is generally negative, whereas the sign of the nighttime flux is positive, but they are often of similar magnitude. Before t_0 , the convective boundary layer is well mixed up to a height of typically 1 km, whereas after t_0 a strong NBL confines emissions from the surface to the lowest ≈ 100 m of the atmosphere (see Sect. 4.4.3). Therefore, the horizontal heterogeneity in c caused by the horizontal heterogeneity in S is one order of magnitude smaller during day time than during the night. The convective mixing during the day also keeps vertical gradients inside the boundary layer low, hence the approximation of $x(t_0)$ being independent of z is justified.

4 Using COCAP to estimate nocturnal fluxes

Term B in Equation 4.3.11 contains the product $w \partial c / \partial z$, which generally includes both turbulent exchange and subsidence. In a stable NBL, however, little turbulent exchange takes place. In the statically neutral residual layer above the NBL, turbulence is present, but the vertical concentration gradient in the residual layer is small and as a consequence the vertical transport of CO₂ is small as well. Hence, we neglect turbulent exchange and identify $w \partial c / \partial z$ with subsidence or lifting. The vertical wind speed w due to subsidence at a height of 100 m is usually on the order of $100 \text{ m} \cdot \text{d}^{-1}$, i.e. very low and therefore challenging to measure. We retrieve an estimate of w from the Integrated Forecast System (IFS) run by the European Centre for Medium-Range Weather Forecasts (ECMWF).

In order to calculate $\partial c / \partial z$ at different times between t_0 and t_F , we use a simple model for the growth of the NBL:

$$x_{\text{CO}_2}(t, z) = x_{\text{CO}_2}\left(t_F, \frac{t_F - t_0}{t - t_0} z\right) \quad (t_0 < t \leq t_F). \quad (4.3.13)$$

Where $\frac{t_F - t_0}{t - t_0} z$ exceeds the maximum height of the profile measured at time t_F we assume the CO₂ dry air mole fraction to be equal to $x(t_0)$. This model for the growth of the NBL can be visualised best by starting at t_F and looking back in time. At $t = t_F$ the factor $(t_F - t_0) / (t - t_F)$ is equal to unity and the model yields the measured profile. At earlier times, the measured profile is compressed in z -direction, such that the height of the NBL decreases linearly as we go back in time. As t approaches t_0 , the model yields a thin layer enriched with CO₂ at the surface and a constant CO₂ dry air mole fraction of $x(t_0)$ above.

The concentration $c(t, z)$ is calculated from $x_{\text{CO}_2}(t, z)$ using Equation 4.3.12. To this end, we determine $p_d(t, z)$ and $T(t, z)$ by linear interpolation in time between the first profile of the night and the profile measured at t_F .

In summary, the model for the growth of the NBL represents four simplifying assumptions: (1) During the night, the NBL height increases linearly, (2) the integral $\int_0^{z_t} x_{\text{CO}_2}(t, z) dz$ increases linearly with time, (3) the shape of the x_{CO_2} profile (constant, linear, exponential. . . with height) within the NBL remains the same throughout the night and (4) the dry pressure and temperature of an air column measured at Fendt are representative for the whole footprint of the measurement (see Sect. 4.3.4).

4.3.4 Footprint calculation

The columns of air probed at Fendt at different times had a different history, depending on the wind field and atmospheric stability. Atmospheric transport models can identify the surface areas that have contributed to an observed tracer concentration, i.e. the footprint of an observation. We simulate atmospheric transport with STILT, the Stochastic

Time-Inverted Lagrangian Transport model (Lin et al., 2003; Gerbig et al., 2003), which is based on NOAA's HYSPLIT particle dispersion model (Stein et al., 2015). In our configuration, STILT launches 10 000 air parcels at different heights (see below) at every full hour during the period of our NBL measurements. Driven by meteorological data with a resolution of $0.1^\circ \times 0.1^\circ$ from the ECMWF IFS (European Centre for Medium-Range Weather Forecasts Integrated Forecast System), STILT calculates the back trajectories of these parcels until 10 h in the past. For each time step of the simulated transport the model determines the sensitivity of the CO_2 concentration in the parcel to the CO_2 flux at the surface. To do so, the height up to which mixing occurs is estimated from the meteorological data. Surface fluxes are expected to be diluted into a column that extends from the surface to 1/2 this height in each time step.

The back trajectories calculated by STILT are then aggregated into mole fraction footprints on a regular grid with a resolution of $2 \text{ km} \times 2 \text{ km}$. As explained in the previous section we assume the x_{CO_2} distribution to be homogeneous in the lateral and horizontal directions at time t_0 . We therefore restrict the aggregation to that part of each back trajectory that lies between t_0 and the time of measurement.

A single STILT run determines the sensitivity of an observation at a specific height to upwind fluxes. Formally, the mole fraction footprint of a measurement taken at the geographic location (l_1, l_2) at time t and observation height z can be written as $f(l_1, l_2, z, t \mid l_{G1}, l_{G2})$. As all our measurements were taken at the same horizontal location, the dependency of f on l_1 and l_2 will be omitted hereafter. The mole fraction footprint is a function whose value is the sensitivity to the surface flux at the grid cell specified by (l_{G1}, l_{G2}) in units of $[f] = \mu\text{mol} \cdot \text{mol}^{-1} \cdot \mu\text{mol}^{-1} \cdot \text{m}^2 \cdot \text{s}$. To determine the relative contribution of surface fluxes in different areas to our NBL-derived fluxes we need a different, but related function, the flux footprint f_F with units $[f_F] = \mu\text{mol} \cdot \text{m}^{-2} \cdot \text{s}^{-1} \cdot \mu\text{mol}^{-1} \cdot \text{m}^2 \cdot \text{s} = 1$. The flux footprint is calculated by integration over an array of mole fraction footprints for different measurement heights, i.e. analogous to Equation 4.3.11 term A and Equation 4.3.12:

$$f_F(t \mid l_{G1}, l_{G2}) = \frac{\int_0^{z_t} \frac{p_d(z, t)}{RT(z, t)} \cdot f(z, t \mid l_{G1}, l_{G2}) dz}{t - t_0} \quad (4.3.14)$$

Dry pressure p_d and air temperature T at time t and height z are inter- or extrapolated from the measured profiles. The ensemble of mole fraction footprints comprises footprints for 12 different measurement heights between 10 m and 120 m in 10 m-steps.

The meteorological data we use have a horizontal resolution of $0.1^\circ \times 0.1^\circ$, corresponding to $11 \text{ km} \times 8 \text{ km}$ at the latitude of Fendt. Terrain features that are smaller than a grid cell, like the valley slope to the west of the Fendt site, cannot be represented at

4 Using COCAP to estimate nocturnal fluxes

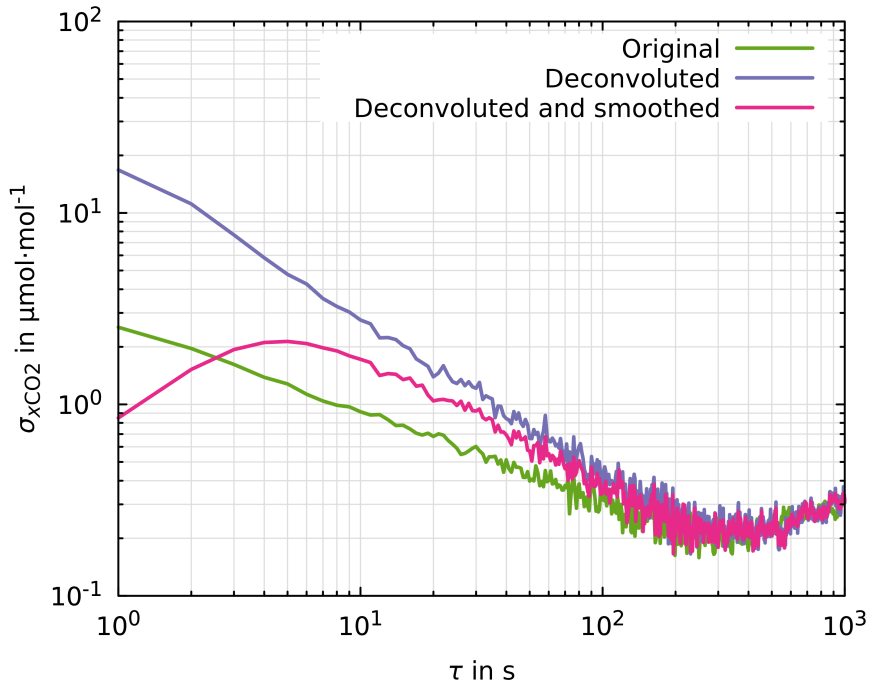


Figure 4.4: Allan deviation of CO₂ dry air mole fraction $\sigma_{x_{CO_2}}$ as measured, after deconvolution and after deconvolution followed by smoothing (convolution with a Gaussian of 5 s FWHM) for different averaging periods τ . All three cases converge for averaging periods longer than 100 s.

these resolutions. The vertical resolution of the meteorological data depends on height above ground. The lowest layer extends from the ground to 10 m height, the following 5 layers extend from the top of the next lower layer to 31 m, 55 m, 80 m, 108 m and 138 m, respectively.

4.4 Results and discussion

4.4.1 Uncertainty of x_{CO_2} measurements

The uncertainty of COCAP's x_{CO_2} measurements due to drift and calibration errors is about $1 \mu\text{mol}\cdot\text{mol}^{-1}$ (see chapter 2). The additional uncertainty caused by noise is dependent on the data treatment, as can be seen from Figure 4.4. This Allan deviation plot (Allan, 1987) is based on measurements of a gas standard ($x_{CO_2} = 447.44 \mu\text{mol}\cdot\text{mol}^{-1}$) over a period of 1.4 h, taken in the field on 6 July 2016.

The curves illustrate that deconvolution amplifies noise in the data by a factor of 7 if no averaging is applied ($\tau = 1$ s). However, if more than 100 samples are averaged, the difference between original and deconvoluted data becomes negligible and the uncertainty of the average due to noise is lower than $0.5 \mu\text{mol}\cdot\text{mol}^{-1}$. All our column integrals (see Section 4.3.3) have a sample size larger than 100.

Figure 4.4 also shows the Allan deviation of deconvoluted data that has been smoothed by convolution with a Gaussian of 10 s FWHM. The Allan deviation increases between $\tau = 1$ s and $\tau = 5$ s. This increase is an artefact caused by the autocorrelation that the smoothing induces. If COCAP was perfectly calibrated and exhibited no drift, any single point in the smoothed dataset would have an uncertainty of $2.1 \mu\text{mol}\cdot\text{mol}^{-1}$ (corresponding to $\tau = 5$ s), not $0.8 \mu\text{mol}\cdot\text{mol}^{-1}$ (corresponding to $\tau = 1$ s).

4.4.2 Meteorological conditions

From the data collected during ScaleX 2016 we calculate NEE for the nights 6–7 July and 9–10 July. The sun set at 19:15 UTC and 19:14 UTC on 6 and 9 July, respectively, and rose at 03:25 UTC and 03:27 UTC on 7 and 10 July, respectively. Both nights were free of precipitation. Cloud cover was high during the first night (see Figure 4.5a), but the pronounced negative net radiation (Figure 4.5b) indicates that the clouds were mostly transparent for outgoing long-wave radiation. In the second night the sky was clearer, resulting in a steadier radiation balance. During both nights, strong radiative cooling was observed. Air temperature decreased from 18°C to 9°C and from 24°C to 11°C over the course of the first and second night, respectively (Figure 4.5c). In combination with low wind speeds (Figure 4.5d) this lead to the development of a pronounced temperature inversion at the surface, i.e. a stable NBL. The change from positive to negative net radiation occurs approximately at $t_0 = 18 : 00$ UTC in both nights.

4.4.3 Profiles

We carried out a total of 27 flights during the ScaleX 2016 campaign. For the calculation of a NBL budget we analyse those flights that took place after $t_0 = 18:00$ UTC and reached a height of at least 125 m. Twelve flights fulfil these criteria: flight 4 through 10 (first night, Figure 4.6) and flight 19 through 23 (second night, Figure 4.7). The location of take-off and landing differs slightly between flights, but all flights took place within the same $250 \times 250 \times 150 \text{ m}^3$ bounding box. For display in panel b of Figures 4.6 and 4.7 the CO_2 dry air mole fraction has been smoothed with a Gauss filter of 5 s FWHM. To prevent distortion in the vertical direction, the height z has been filtered the same way. For this reason, the upper end of the profiles in panel b is at slightly lower height than in

4 Using COCAP to estimate nocturnal fluxes

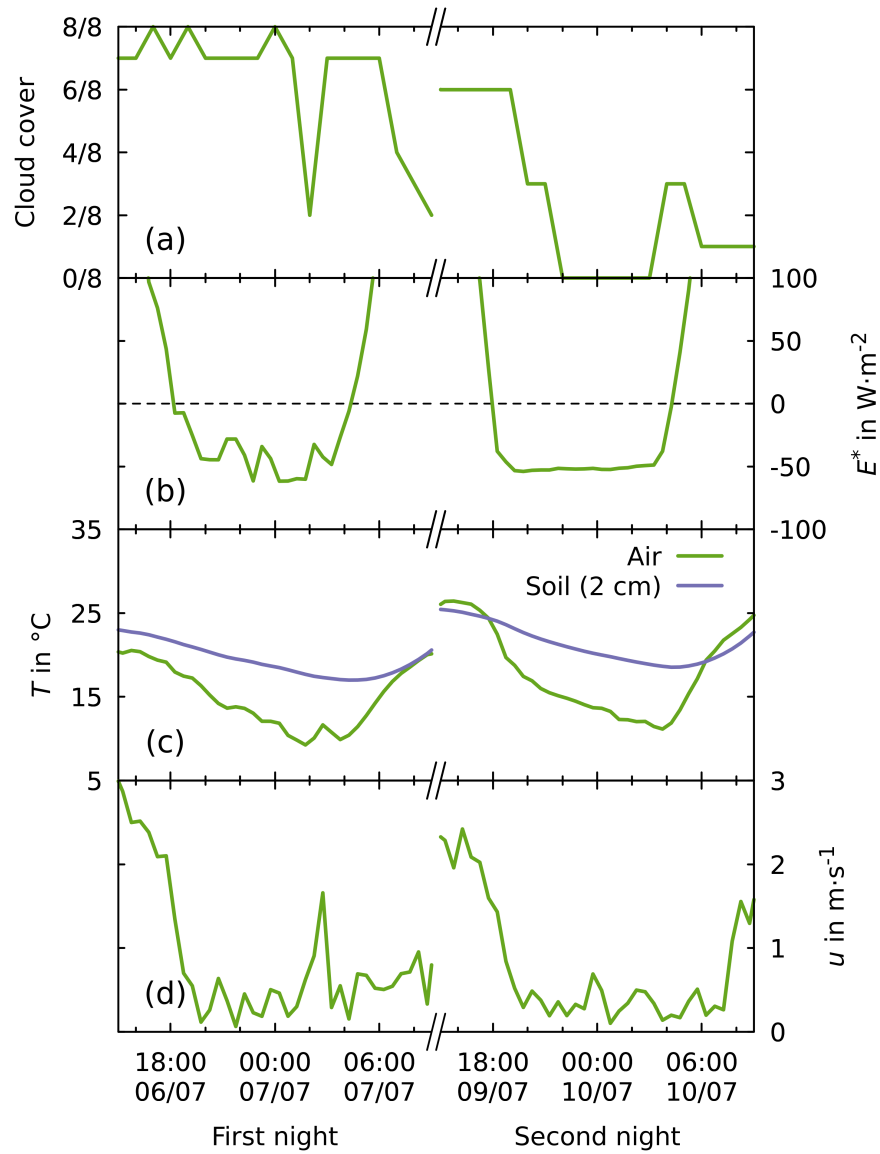


Figure 4.5: Meteorological conditions during the NBL soundings: (a) cloud cover, (b) net radiation E^* , (c) temperature T of air (2 m height) and soil (2 cm depth), (d) horizontal wind speed u (3.5 m height). Cloud cover was determined at MOHP, all other observations were made directly at Fendt.

panel a. Calculation of the NBL fluxes (see Section 4.4.5) was carried out with unfiltered x_{CO_2} and z .

During the first night, a stable NBL can be identified from the UAS profiles for flights 6 through 10. The upper end of the temperature inversion aligns with the top of the CO_2 enhancement to within 10–20 m. At the time of flights 6 and 8 through 10, the NBL has a height of 50–70 m, whereas the profile from flight 7 indicates a greater NBL height of ≈ 100 m. We interpret this as an indication that the column measured in flight 7 has been influenced by katabatic inflow of cool, CO_2 -enriched air at some point during the night, potentially hours before the flight and kilometres away from Fendt. This interpretation is supported by the flux estimates (see Section 4.4.5). The profiles from flight 5, which exhibit virtually no gradient, are discussed below.

During the second night, a stable NBL with a height of 50–70 m is visible in all profiles. The flight pattern had been refined and included two ascents and descents far enough from each other to avoid disturbance of the measurements in the second part by air movements caused during the first part. These redundant measurements give insight to the reliability of the measurement system and to the variability of temperature and CO_2 dry air mole fraction on small temporal and spatial scales. The data from flight 21 agrees well between each of the two ascents and descents, suggesting that disturbance by the UAS, instrument noise and drift are small compared to the observed signals. Flight 22 and 23 were carried out only one and two hours later, respectively, and followed the same flight track. However, the data from these flights reveals considerable differences between each of the two ascents and descents, especially in x_{CO_2} for heights below 50 m. We interpret this as natural variability on the scale of the flight track, i.e. ≈ 200 m in horizontal distance and ≈ 3 min in time. This small-scale variability is a source of random error in NBL budgets. Multiple ascents during the same flight are effectively averaged in our flux calculations, resulting in a reduction of the random error.

The x_{CO_2} profiles measured during flight 20, 22 and 23 all exhibit a non-zero gradient with height in the region above the strong inversion, indicating that some CO_2 has escaped the stable NBL. This is supported by the profiles of virtual potential temperature, which are more inclined above the NBL in comparison to the first night. Both features might be the result of intermittent turbulence, a phenomenon often observed at night that can have different causes (see Aubinet, 2008 and references therein). Our budgets include the measurements up to 125 m height, so any CO_2 that has been transported higher than this is missing in the budgets. In future campaigns, flights with a greater maximum height could be carried out to quantify the effect this has on the NBL-derived fluxes, or to extend the budget vertically.

The flight pattern used during the second night also included two horizontal transects at 10 m height that were flown at a ground speed of $3 \text{ m}\cdot\text{s}^{-1}$. Their purpose was to enable measurements of undisturbed air near the ground, but later analysis of flight

4 Using COCAP to estimate nocturnal fluxes

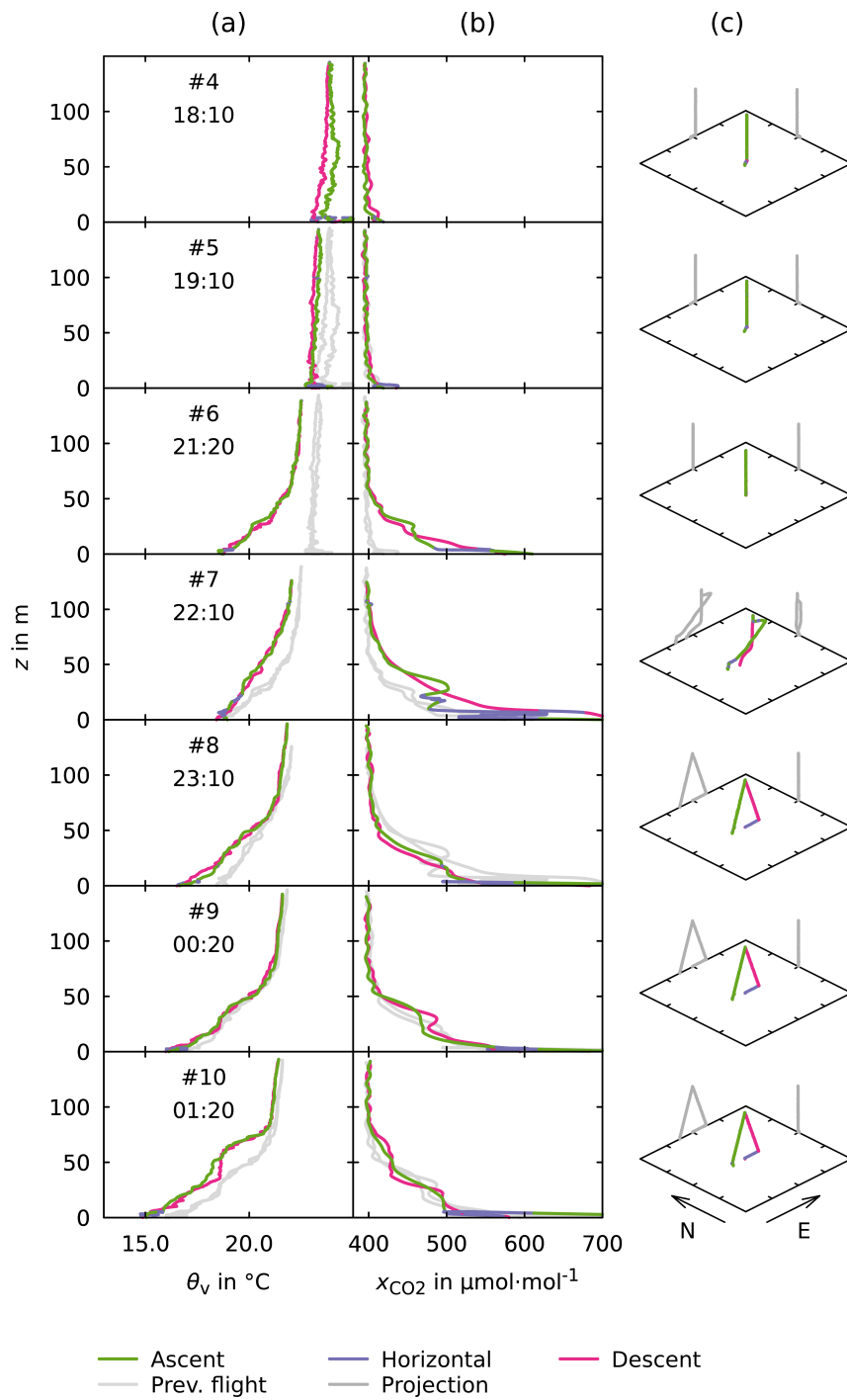


Figure 4.6: Profiles from flights 4 through 10, carried out in the night from 6 to 7 July 2016. Due to space constraints see Fig. 4.7 for complete caption.

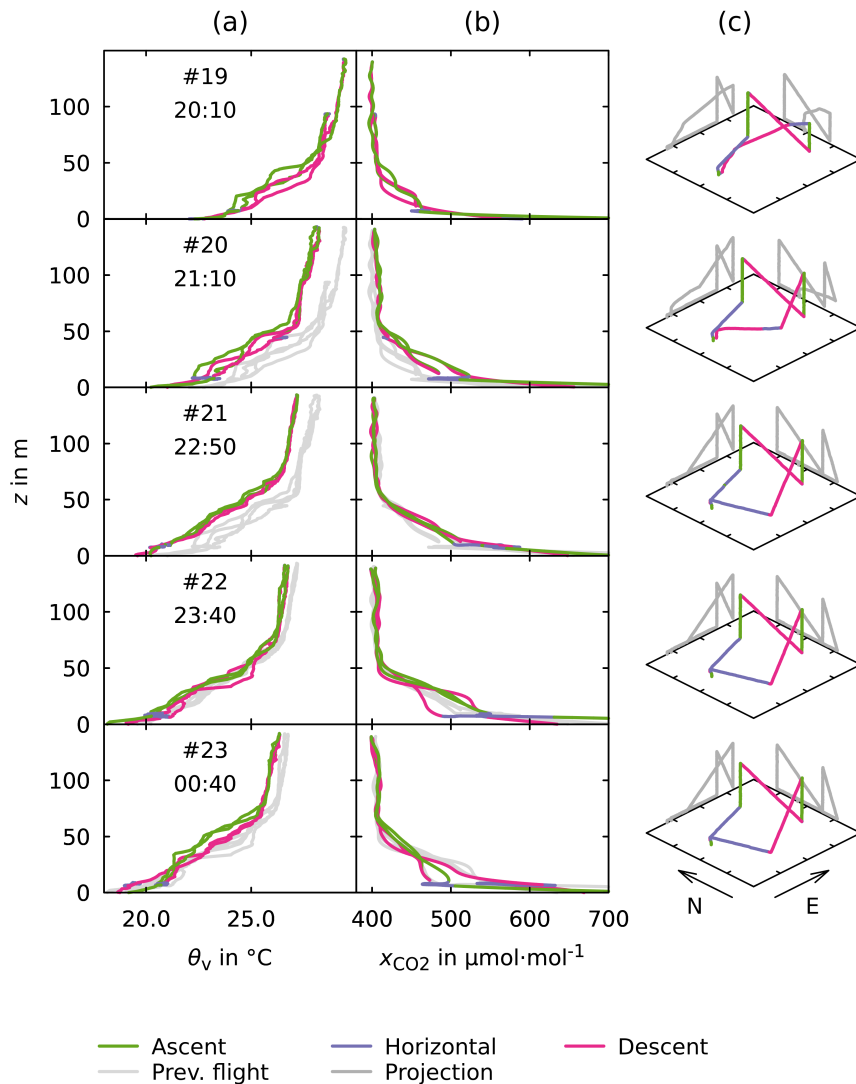


Figure 4.7: Profiles from flights 19 through 23 carried out in the night from 9 to 10 July 2016. Times are given in UTC. (a) Virtual potential temperature θ_v at height z . Axis is shifted towards higher temperatures compared to Figure 4.6, but covers the same span. (b) Carbon dioxide dry air mole fraction x_{CO_2} at height z . To reduce noise x_{CO_2} has been smoothed (for details see text). In both (a) and (b) the light grey curves are copies of the previous profile (ascent, horizontal flight and descent combined). (c) Flight track with horizontal projections (grey). Northward and eastward direction marked, tick marks 100 m apart.

4 Using COCAP to estimate nocturnal fluxes

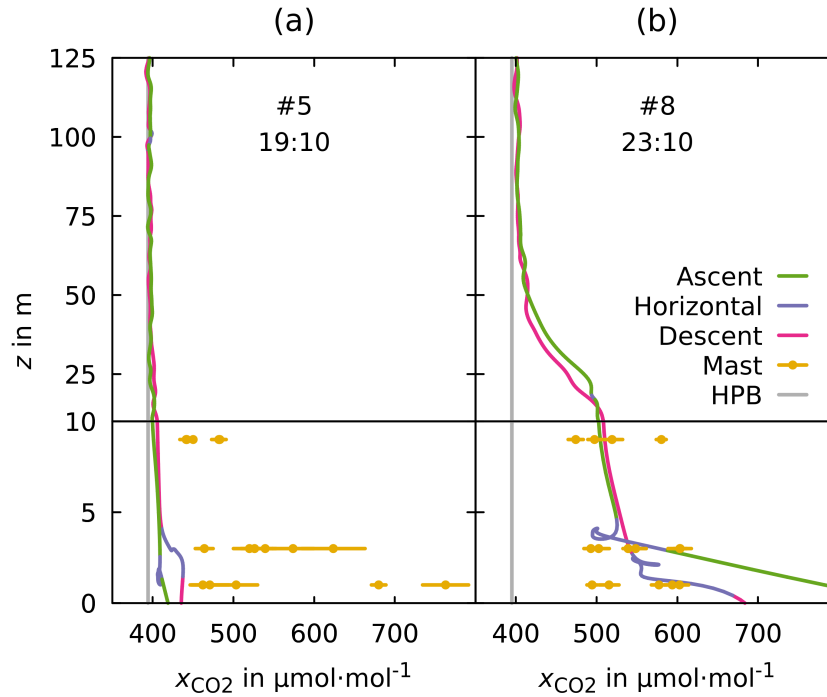


Figure 4.8: Comparison of x_{CO_2} measurements by COCAP, by the ICOS station Hohenpeißenberg (HPB) and by the on-site 9 m mast (a) for flight 5 and (b) for flight 8. The dots and bars are mean and standard deviation, respectively, for each 1-minute sampling period of the mast. Note that the scaling of the vertical axis changes at height $z = 10$ m.

14 (see Section 4.3.1) revealed that the ground speed was insufficient to fully reach this goal.

The profiles for flight 5 are close to straight vertical lines, which would indicate a well-mixed atmosphere. However, they were measured under low wind speed one full hour after the surface radiation balance became negative, i.e. under conditions favourable for the development of a stable nocturnal boundary layer and accumulation of CO_2 near the ground. This apparent contradiction can be explained by comparing COCAP's data to stationary measurements. Figure 4.8a shows the CO_2 profile taken by COCAP together with data from the 9 m mast and from HPB (see Sections 4.2.1 and 4.2.2). The diagram includes those measurements from the mast that fall into the time interval from 15 min before take-off to 15 min after landing. They reveal that the CO_2 dry air mole fraction near the ground was increased relative to the upper two thirds of the profile and fluctuated strongly, e.g. at 3 m height between 450 and 650 $\mu\text{mol}\cdot\text{mol}^{-1}$. These observations are in line with a weakly stable layer near the surface: Surface

fluxes accumulated in this layer, but weak turbulent events caused e.g. by wind shear occasionally spread them out to higher layers. The disturbance by the multicopter during take-off or landing prevented COCAP from seeing this accumulation. On the other hand, the higher part of COCAP's profile, taken in the residual layer that is left over from the daytime mixed layer, matches the mean CO₂ dry air mole fraction measured at HPB during the time interval from 1 h before take-off to 1 h after landing. This agreement confirms that COCAP was working properly during the flight.

The profile from flight 8, carried out later in the same night, is consistent with the measurements at the 9 m mast (Figure 4.8). We see two reasons for this difference to flight 5. Firstly, the radiative cooling (see Figure 4.5) at the time of flight 8 (23:10) was stronger than at the time of flight 5 (19:10). The temperature gradient near the ground was not resolved in COCAP's measurements during flight 5, but the weaker radiative cooling compared to the later flight has likely resulted in a weaker temperature inversion, allowing more vertical displacement of air by the multicopter. Secondly, the thicker NBL at 23:10 with a less steep CO₂ gradient close to the ground means that potential sampling of air parcels originating from above or below the multicopter did not affect the measurements during flight 8 as much as during flight 5.

At heights above 70 m the CO₂ profile from flight 8 approaches the CO₂ mole fraction measured at HPB, indicating that the stable NBL retains most of the surface fluxes. Likewise, the CO₂ profiles of all other flights come near the measurements at HPB above the NBL (not shown). This suggests that any transport of CO₂ across the top of the NBL is small in magnitude.

The measurement of continuous profiles of the CO₂ dry air mole fraction up to heights of 100 m or more has been challenging in the past. In some studies, NBL budgets were therefore based on a measurement near the ground and an assumed gradient up to the top of the NBL. However, the complex shape of the profiles displayed in Figures 4.6 and 4.7 suggest that neither the assumption of a constant (cf. Acevedo et al., 2004) nor a linearly decreasing (cf. Culf et al., 1997) CO₂ dry air mole fraction would properly represent the conditions at Fendt. The detailed structures resolved in our measurements also indicate great potential of combined measurements of meteorological parameters and trace gas mole fractions for studying small-scale phenomena in the NBL.

4.4.4 Disturbance by the UAS

The potential virtual temperature measured at heights between 10 and 60 m are generally higher during descent than during ascent. This effect is more pronounced for flights 19 through 23 (Figure 4.7), likely due to the stronger temperature gradient compared to flights 5 through 10 (Figure 4.6). The observed difference supports the reasoning of Section 4.3.1: As the multicopter descends, the onboard sensors measure warmer air

4 Using COCAP to estimate nocturnal fluxes

that was pushed downwards by the rotors. Close to the ground (at heights below 10 m) closed flow loops start to form and colder air from below the multicopter reaches the sensors during descent, as can be seen in the profiles from flights 6, 8, 9, 10 and 23.

Systematic differences between ascent and descent are less visible in the profiles of CO₂ dry air mole fraction, likely due to a larger variability of CO₂ within the nocturnal boundary layer. This variability is reflected in the difference in x_{CO_2} between each of the two ascents and descents in the flights 19 through 23, esp. flight 20 and 23.

Flight 14 was dedicated to the investigation of vertical mixing during horizontal movement at different air speeds. It was carried out on 7 July at 22:15 UTC. Winds were particularly low that night (on average $0.3 \text{ m}\cdot\text{s}^{-1}$ between 22:00 and 22:30 UTC) and hence ground speed of the UAS was approximately equal to air speed. A stable nocturnal boundary layer had developed, as can be seen from the profiles of θ_v and x_{CO_2} measured during an earlier flight at 20:15 UTC (see Figure 4.9 panels a and b). The UAS flew a spiral pattern at a height of 10 m above ground with decreasing ground speed (Figure 4.9c). Throughout flight 14, COCAP's air inlet faced the direction of movement. The flight took place over a flat, homogeneous meadow. Hence, we assume that terrain and vegetation had caused no heterogeneity in the lateral distribution of temperature and CO₂. We analyse three sections of nominal speed $5 \text{ m}\cdot\text{s}^{-1}$, $3 \text{ m}\cdot\text{s}^{-1}$ and $1 \text{ m}\cdot\text{s}^{-1}$. Figure 4.9d shows the median virtual potential temperature and CO₂ dry air mole fraction for each section. The standard error of the median was calculated by bootstrapping with 1000 samples generated from the empirical distribution of the measurements (Wilcox, 2012, pp. 43) and is depicted as horizontal and vertical bars.

The decrease of virtual potential temperature with decreasing speed in Figure 4.9d suggests that upward mixing of air from lower layers has a stronger influence on the measurements at lower speed. Likewise, the CO₂ dry air mole fraction measured at $1 \text{ m}\cdot\text{s}^{-1}$ is $20 \mu\text{mol}\cdot\text{mol}^{-1}$ higher than during faster flight. However, we did not observe a significant difference in x_{CO_2} between a ground speed of $3 \text{ m}\cdot\text{s}^{-1}$ and $5 \text{ m}\cdot\text{s}^{-1}$. The sample inlet for the CO₂ measurement extends 20 cm to the side of the rotors, while temperature and humidity are measured directly below a rotor (see Fig 4.2). As the sample inlet was pointing forward throughout the flight, it might have mostly avoided partially closed flow loops during movement at $5 \text{ m}\cdot\text{s}^{-1}$, while the temperature and humidity sensors were still affected.

In summary, our results suggest that measurements taken during the ascent of the multicopter are more reliable than those taken during descent and hover. Horizontal transects at low heights can yield measurements that are contaminated with air from below the sampling height. This contamination is lower at higher horizontal air speed, because the multicopter moves away from the vortices it has created. Our experiment does not answer the question whether at 10 m height a horizontal speed of $5 \text{ m}\cdot\text{s}^{-1}$ is sufficient to avoid the contamination entirely.

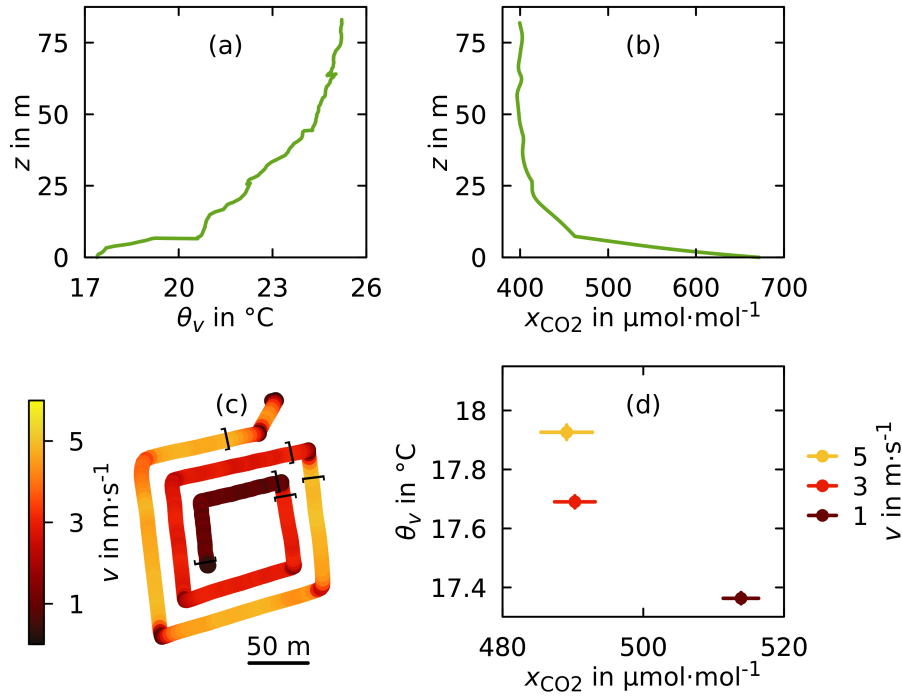


Figure 4.9: Vertical profiles of (a) virtual potential temperature θ_v and (b) CO₂ dry air mole fraction x_{CO_2} at 20:15 UTC on 7 July 2016. (c) Track of flight at 22:15 UTC on the same night coloured by horizontal ground speed. Three sections of nominal speed $5 \text{ m}\cdot\text{s}^{-1}$, $3 \text{ m}\cdot\text{s}^{-1}$ and $1 \text{ m}\cdot\text{s}^{-1}$ are marked with brackets. Height was 10 m above ground throughout the flight. (d) Median of virtual potential temperature and CO₂ dry air mole fraction measured during those three sections of the flight. Bars represent the bootstrapped standard error of the median, see text for details. The standard error of the virtual potential temperature is so small that the vertical bars are barely visible. At lower speeds, θ_v is lower and x_{CO_2} higher, suggesting the sampling of air that originates from below the flight height.

4.4.5 Carbon dioxide fluxes

The first profiles of the first and second night were taken at 18:10 UTC (flight 4) and 20:10 UTC (flight 19), respectively. Hence, Flight 4 is representative for the x_{CO_2} profile at $t_0 = 18 : 00$ UTC, but flight 19 is not. We therefore need an estimate for the profile at t_0 . Due to the convective mixing that takes place during the day, the CO_2 dry air mole fraction within the boundary layer is nearly independent of height, an assumption that is supported by the profile from flight 4 (see Fig. 4.6). Assuming further that all surface fluxes were trapped in the developing NBL, air parcels above the NBL height should have preserved the CO_2 dry air mole fraction of the column between t_0 and the time of the first flight. Consequently, we assume the whole column $x_{\text{CO}_2}(t_0, z)$ to be equal to the mean dry air mole fraction of the first measured profile between 50 m and 125 m height. For consistency we apply this approach to both nights.

The fluxes we calculated from the NBL budgets are listed in Table 4.1, given as amount of CO_2 per time and surface area. We refrain from the common unit $\mu\text{gC-CO}_2 \cdot \text{m}^{-2} \cdot \text{s}^{-1}$ as it does not comply with the SI rules¹. The storage flux in Table 4.1 corresponds to term (A) in Equation 4.3.11, the subsidence flux to term (B) and the total flux is equal to \bar{S} , i.e. the NEE averaged over the time from t_0 to t_F . During both nights, horizontal convergence of air masses lead to lifting and consequently a negative subsidence flux. However, the subsidence flux was small compared to the storage flux, accounting for about 1 percent of the total flux. An important consequence of the low subsidence flux is that errors stemming from the simplified model of the NBL growth (see Sect. 4.3.3) have only a minor influence on the uncertainty of the total flux.

The plausibility of our results can be checked against EC and chamber measurements taken at Fendt. Both the EC and the chamber measurements observed only the fluxes from the pasture at the site, while the NBL budget has a larger footprint. Even at low wind speeds of $0.5 \text{ m} \cdot \text{s}^{-1}$ air parcels travel 1.8 km every hour. Therefore, the NBL budget also includes sources that are located at several kilometres distance. Given the land cover around Fendt, those sources likely include forests, crop fields and potentially some residential areas (see Section 4.14 for an exemplary footprint). Nevertheless, as pasture is the dominant land cover in the area, all three methods should agree in magnitude at night.

No EC measurements of good quality are available for either of the nights during which we probed the NBL (Figure 4.10), because strong radiative cooling with little wind resulted in stable stratification and hence violation of the assumptions underlying the EC technique. Therefore, we resorted to calculating the mean diurnal cycle from

¹“Units are never qualified by further information about the nature of the quantity; any extra information on the nature of the quantity should be attached to the quantity symbol and not to the unit symbol.” (International Bureau of Weights and Measures, 2006, p. 132)

Table 4.1: Fluxes of CO₂ calculated from NBL budgets

Begin dd/mm HH:MM	End dd/mm HH:MM (flight)	Storage flux in $\mu\text{mol} \cdot \text{m}^{-2} \cdot \text{s}^{-1}$	Subsidence flux in $\mu\text{mol} \cdot \text{m}^{-2} \cdot \text{s}^{-1}$	Total flux in $\mu\text{mol} \cdot \text{m}^{-2} \cdot \text{s}^{-1}$
	06/07 19:08 (#5)	13.7	0.0	13.7
	06/07 21:16 (#6)	12.3	-0.1	12.2
06/07 18:00	06/07 22:14 (#7)	16.1	-0.2	15.9
	06/07 23:09 (#8)	11.3	-0.1	11.2
	07/07 00:21 (#9)	9.4	-0.1	9.3
	07/07 01:13 (#10)	8.4	-0.1	8.4
	09/07 21:06 (#20)	17.2	-0.2	17.0
09/07 18:00	09/07 22:48 (#21)	11.3	-0.1	11.2
	09/07 23:43 (#22)	11	-0.1	10.9
	10/07 00:35 (#23)	9.9	0.0	9.9

4 Using COCAP to estimate nocturnal fluxes

the EC measurements taken between 4 July 2016 00:00 UTC and 11 July 2016 23:59 UTC, a period that includes all our flights and was reasonably consistent in the diurnal variations of temperature. The result is presented in Figure 4.10. All fluxes calculated from the NBL budget lie within the range of NEE observed by EC between 18:00 and 01:00 UTC ($6\text{--}16 \mu\text{mol} \cdot \text{m}^{-2} \cdot \text{s}^{-1}$). However, the two methods disagree on the trend during the night. The later the flight at Fendt took place, the lower the NBL-based average NEE, indicating a decreasing flux over the course of the night. We interpret this, at least partially, as an effect of the temperature decrease during the night (Figure 4.5), which reduces respiration. In contrast, NEE from the EC station increases during the night. The reason for this trend is not clear.

Figure 4.11 shows the NBL-derived fluxes in comparison to chamber measurements. Data from the small chambers is available only for the second night. Opaque chambers measure respiration, while clear chambers, the EC station and the NBL budget observe NEE. Therefore, a comparison of the fluxes obtained with these different techniques is only meaningful when photosynthesis is low or absent, i.e. roughly between sunset and sunrise. The convergence of the fluxes of the clear and dark chambers just after 18:00 UTC suggests that photosynthesis has largely ceased as early as t_0 . Hence, throughout the time span for which we create the NBL budget NEE is dominated by respiration and all the different techniques are comparable. Surprisingly, the measurements with the big chambers yield fluxes only 1/3 as high as obtained with the small chambers, even though all chambers were deployed close to each other on the same meadow. Despite careful investigation the reason for this discrepancy has not yet been found. The NBL budgets agrees in magnitude to the fluxes measured with the small chambers. Similar to the NBL budget, all chamber measurements exhibit a negative trend in fluxes over the course of both nights.

In addition to in situ measurements at Fendt, the range of nighttime NEE of pasture and forests observed in other studies at central European sites with a climate similar to Fendt (Cfb or Dfb in the Köppen-Geiger classification according to Peel et al., 2007) provides a plausibility check for the NBL budgets (Table 4.2). We exclude crop fields from the comparison, as their NEE depends heavily on crop type and time of harvest. Compared to the literature values, NEE for Fendt derived from the NBL budget is on the high end of ranges reported for pasture and higher than fluxes reported for forests. One explanation is that our measurements took place on two fair weather days in the warmest month of the year 2016, which likely resulted in higher respiration than observed on average over a longer period. Another potential cause for higher fluxes observed with the NBL budget relates to the terrain at Fendt. At night, katabatic flows of cool, CO_2 -rich air can stream down the steep slope west of the measurement site. Though Fendt is situated in a valley with only a shallow slope to the east, this inflow might lead to localised lifting of air that is not accounted for in the ECMWF IFS data

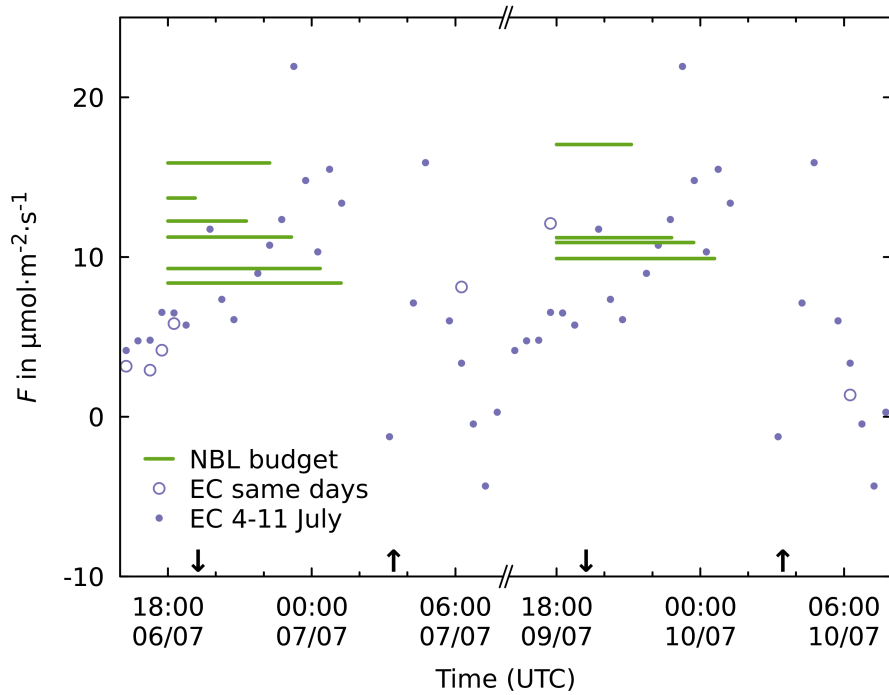


Figure 4.10: Comparison of vertical fluxes F calculated from the NBL budget and using the EC method. The fluxes from the NBL budget are depicted as lines, where the vertical position of each line represents the average flux over the time span specified by the horizontal extend of the line. Open circles represent the quality-filtered EC measurements taken on the same days as the NBL measurements. Solid dots represent the mean diurnal cycle of the quality-filtered EC measurements averaged over the period from 4 July 2016 00:00 UTC to 11 July 2016 23:59 UTC. Upward and downward arrows mark the time of sunrise and sunset, respectively. NBL budget and EC agree in magnitude of NEE at night, but not in sign of the trend.

4 Using COCAP to estimate nocturnal fluxes

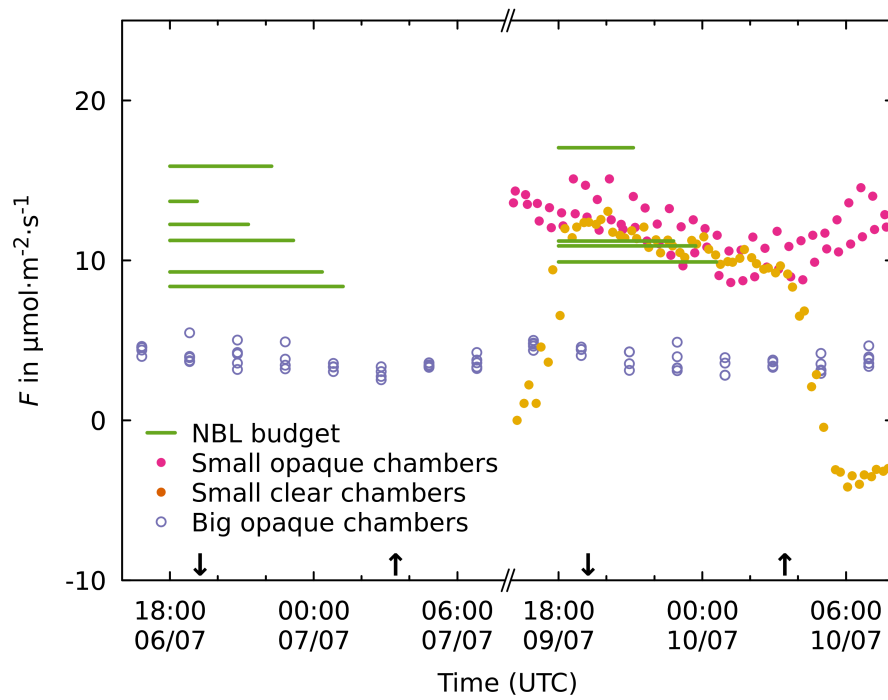


Figure 4.11: Comparison of flux F calculated from the NBL budget and flux measured with different chambers. The axis scaling and sunset/sunrise markers are the same as in Figure 4.10. Nighttime fluxes observed with the small and the big chambers differ by a factor of three for unknown reasons. The NBL budget agrees in magnitude and trend to the measurements with the small chambers.

Table 4.2: Nighttime fluxes observed in other studies

Location	Land cover	Period dd/mm/yyyy	Method	Flux in $\mu\text{mol} \cdot \text{m}^{-2} \cdot \text{s}^{-1}$	Source
Grillenburg, Germany	Pasture	02/07/2004– 16/07/2004	EC	5.1–10.5	Gilmanov et al. (2007)
Stubai Valley, Austria	Pasture	01/07/2002– 30/07/2002	EC	6–17	Wohlfahrt et al. (2005)
Stubai Valley, Austria	Pasture	01/07/2002– 30/07/2002	Chambers + model	6–11	Wohlfahrt et al. (2005)
Stuttgart, Germany	Pasture	13/08/2006– 17/11/2006	Chambers	1.3–3.2	Chen et al. (2014)
Waldstein– Weidenbrunnen, Germany	Managed spruce forest	01/06/2007– 15/07/2007	Mass balance	1–7	Siebicke et al. (2012)
Hesse, France	Managed beech forest	05/08/2005– 06/08/2005	EC	1.1–5.5	Longdoz et al. (2008)
Hainich, Germany	Unmanaged beech forest	12/08/2005– 30/09/2005	Mass balance	3–9	Kutsch et al. (2008)
Hainich, Germany	Unmanaged beech forest	12/08/2005– 30/09/2005	Bottom-up model	5–5.5	Kutsch et al. (2008)

4 Using COCAP to estimate nocturnal fluxes

and hence not included in our calculation of subsidence. The increased NBL height and high variability in the lowest 50 m observed during flight 7 as well as the higher flux derived from the NBL budget are an indication of such an inflow event.

4.4.6 Sensitivity of fluxes

The NBL budget is influenced by measurement uncertainty, incomplete knowledge about the state of the atmosphere and data selection. In order to quantitatively assess the influence of these factors on our results, we changed the procedure of calculating fluxes in either of the following ways:

1. by adding a bias of ± 2 m to the altitude measurements,
2. by adding a bias of $\pm 3 \mu\text{mol}\cdot\text{mol}^{-1}$ to x_{CO_2} of all but the first profile of each night,
3. by using COCAP data for the whole column instead of replacing x_{CO_2} in the lowest 9 m with stationary measurements taken at the 9 m mast,
4. by using COCAP data taken during the whole flight, i.e. using ascent, descent and hover instead of ascent only, or
5. by disregarding subsidence.

Check 1 accounts for the uncertainty of COCAP's pressure-based altitude measurements. Check 2 allows us to evaluate the influence of both the uncertainty of COCAP's x_{CO_2} measurements and the spatial heterogeneity of $x(t_0)$. The former is known from experiment (see Section 4.4.1) and the latter can be estimated from the CO_2 measurements at HPB. Assuming that the 131 m inlet at HPB is in the residual layer all night, the interquartile range of the x_{CO_2} measurements of a single night approximately reflects the variability of the background onto which fluxes accumulate. It amounts to $1.1 \mu\text{mol}\cdot\text{mol}^{-1}$ and $2.4 \mu\text{mol}\cdot\text{mol}^{-1}$ for the period from 18:00 UTC to 02:00 UTC in the first and second night, respectively. Check 3 and 4 relate to the disturbance caused by the UAS, which is discussed in Sections 4.3.1 and 4.4.4.

The mean fluxes for each night obtained using the changed procedures are summarised in Table 4.3. The largest difference to the normal ("No change") procedure occurs when x_{CO_2} is altered ($\pm 11\%$ for the first and $\pm 7\%$ for the second night, respectively). Biasing the altitude or not using the data from the 9 m mast also have a considerable influence on the mean flux.

Figure 4.12 shows the values from Table 4.3 in graphical form. In addition, the fluxes calculated for each flight are depicted, visualising how their spread is affected by the different checks. A substantial increase in spread is observed only when the data from the 9 m mast is not used.

Table 4.3: Sensitivity of flux to different factors (see text for details). Unit of fluxes is $\mu\text{mol} \cdot \text{m}^{-2} \cdot \text{s}^{-1}$.

Night	No change	z + 2 m	z - 2 m	x _{CO₂+} 3 ppm	x _{CO₂-} 3 ppm	Whole flight	w/o 9 m mast	No subsid.
1	11.8	12.2 (+3 %)	10.6 (-10 %)	13.1 (+11 %)	10.5 (-11 %)	11.4 (-3 %)	10.8 (-8 %)	11.9 (+1 %)
2	12.3	12.7 (+3 %)	11.7 (-5 %)	13.1 (+7 %)	11.4 (-7 %)	11.9 (-3 %)	12.7 (+3 %)	12.4 (+1 %)

4 Using COCAP to estimate nocturnal fluxes

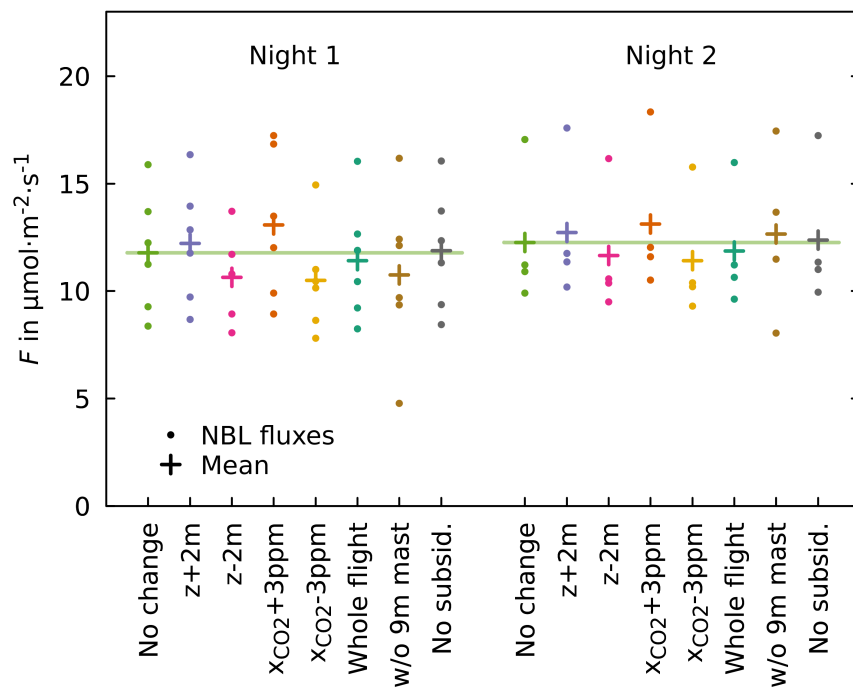


Figure 4.12: Sensitivity of flux to changes in calculation procedure. Dots denote the fluxes calculated for each flight, crosses mark the mean of these fluxes. The lines are visual aids to facilitate comparison to the mean flux of the normal (“No change”) procedure.

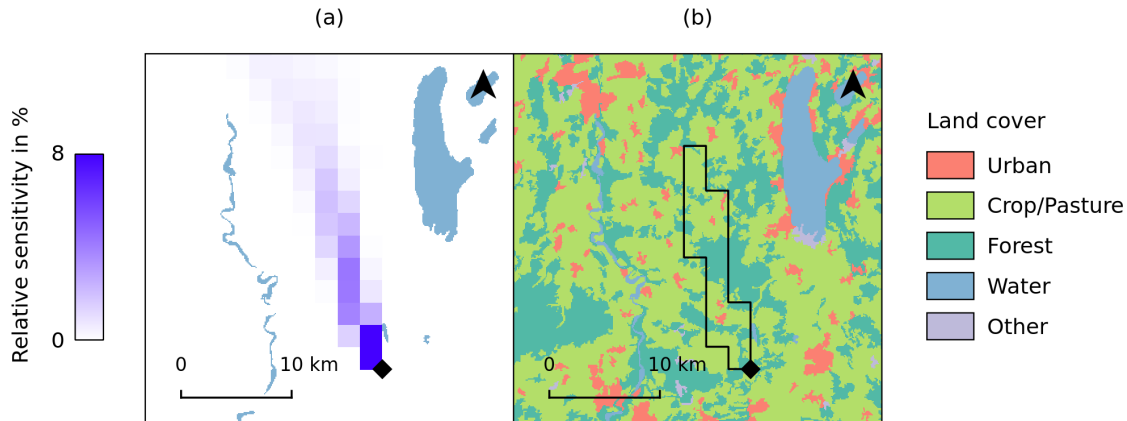


Figure 4.13: Footprint of an NBL budget at Fendt on 6 July 21:00 UTC. (a) Relative contribution of each grid cell to the total sensitivity of the budget to surface fluxes. Water bodies depicted for orientation. (b) Contour of all grid cells with a relative sensitivity of 1% or higher on top of a simplified land cover map (CORINE 2012 v18.5, European Environment Agency, EEA (2016)). The area observed is dominated by forests, pasture and crop land.

Overall, the results from the sensitivity checks indicate that the NBL method is robust against measurement uncertainty in the altitude and x_{CO_2} measurements, spatial heterogeneity of $x(t_0)$, disturbance of the NBL caused by the UAS and the effect of subsidence. It should be noted that the mean vertical wind extracted from the ECMWF IFS model was relatively small during the two nights of our measurements. Under different conditions, e.g. in a strong high pressure system, the effect of subsidence or lifting on the NBL budget could be much higher.

4.4.7 Flux footprint

An example flux footprint of an NBL budget is visualised in Figure 4.14.

The footprint depicted in Fig. 4.13 was calculated for a column of air passing Fendt on 6 July 2016 at 21:00 UTC, i.e. close to the time of flight 6. The 1% contour of the footprint encloses an area of 60 km^2 , which accounts for 60% of the total sensitivity. The land cover map suggests that the NBL budget represents mainly the respiration of forests, pasture and crop lands north of Fendt, with little contribution from urban areas.

The footprint depicted in Fig. 4.14 was calculated for a column of air passing Fendt on 9 July 2016 at 21:00 UTC, i.e. close to the time of flight 20. The 1% contour of the footprint encloses an area of 80 km^2 , which accounts for 70% of the total sensitivity. Again, the NBL budget is mainly influenced by forests, pasture and crop lands.

4 Using COCAP to estimate nocturnal fluxes

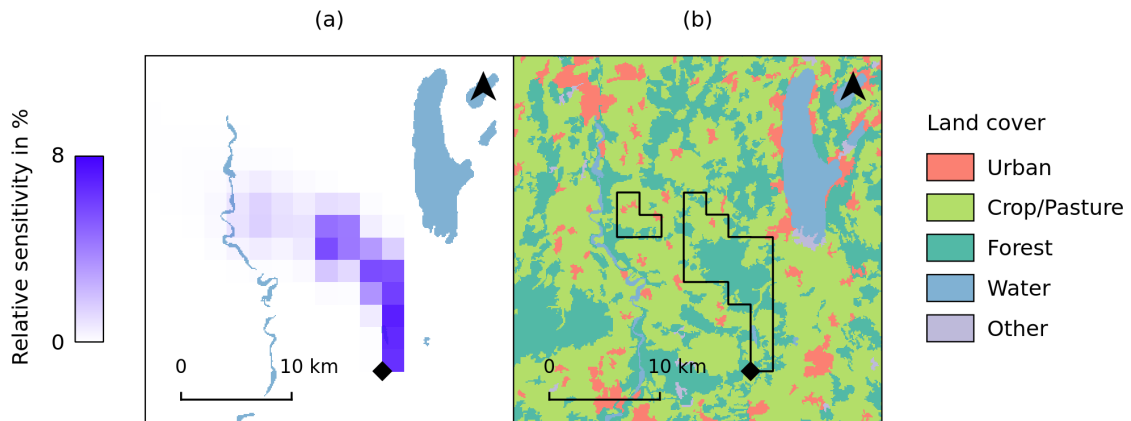


Figure 4.14: Same as Fig. 4.13, but for 9 July 21:00 UTC

The footprints for other times during the two nights are similar in size, i.e. on the order of 100 km^2 . They mostly cover the sector within 20 km north-west to north-east of Fendt.

We recognise that the relatively low spatial and temporal resolution of the ECMWF IFS meteorological model entails errors in the transport modelling. However, as our NBL budgets cover time scales of 1–7 hours and the footprints extend over many grid cells, sub-scale variability should play only a minor role. We are therefore confident that the model results provide a reasonable estimate of the region seen by the NBL budget method.

4.5 Summary of Chapter 4

To the best of our knowledge, we have for the first time created nocturnal boundary layer budgets that are based on trace gas measurements with a UAS. During two nights we repeatedly sampled the NBL with a multicopter carrying COCAP, a lightweight analyser designed for deployment on unmanned aircraft. Simultaneous measurement of CO_2 dry air mole fraction, air temperature, humidity and pressure allowed us to quantify the rate of accumulation of carbon dioxide in the NBL. By applying deconvolution we could improve the temporal resolution of the CO_2 measurements, thus achieving a higher vertical resolution of the profiles. We estimated the effect of subsidence or lifting on the NBL budgets with the help of weather forecast data and corrected the budgets accordingly. The respiration fluxes obtained from the NBL budgets are plausible in comparison to other flux measurements at the Fendt site, though at the high end of the range reported in the literature for sites with land cover and climatic conditions

similar to Fendt. A potential positive bias in the obtained fluxes could be caused by convergence of cool, CO₂-rich air at the floor of the valley in which Fendt is located. The current data set does not allow to confirm or rule out this effect. In a future campaign, however, simultaneous deployment of a second UAS on the elevated plateau west of the site could provide more insight, as downward transport of CO₂ should result in consistently lower fluxes obtained on the plateau.

We have investigated how the disturbance of the NBL caused by a multicopter influences in situ measurements. We found that while flying close to the ground, air from below the UAS can reach the sensors, causing a bias if the respective quantity has a non-zero gradient. To prevent this bias from affecting the NBL budget we replaced the airborne x_{CO_2} measurements taken at low height with stationary measurements from a 9 m mast. At greater height, some of our profiles exhibit a systematic difference between ascent and descent. During descent, the airborne sensors are moved into a volume of air that may have been disturbed by the downwash of the multicopter's rotors. Therefore, we use only data captured during ascent for NBL budgeting.

The robustness of our approach has been demonstrated by a sensitivity analysis. The largest uncertainty of the NBL budget is caused by spatial heterogeneity of the CO₂ dry air mole fraction in the late afternoon combined with the uncertainty of the CO₂ measurement. The estimated combined error in x_{CO_2} results in $\pm 11\%$ change of the mean of the fluxes obtained from the NBL budget for the first night. Using only data from the UAS and not from the 9 m mast increased the spread of the fluxes, but changed their mean by no more than 8%. This suggests that satisfactory NBL budgets can be created from UAS data even if no stationary measurements near the ground are available.

The region that influences an NBL budget has often not been reported in past studies. We improved on this situation by carrying out mesoscale modelling. While the driving meteorological data and the underlying topography do not resolve small structures at the scale of 1 km and below, our method gives at least an estimate of the region that influences the NBL budget. Under the conditions of our measurements the footprints had a size on the order of 100 km². In situ wind measurements would allow the validation of the meteorological data and possibly an improvement of the transport modelling. Such measurements could be taken by UAS without the need for additional sensors (Mayer et al., 2012, Neumann and Bartholmai, 2015).

5 Conclusions and outlook

We have developed COCAP, a compact carbon dioxide analyser for deployment on board unmanned aircraft. By including a fast and precise temperature stabilisation, by thorough calibration in an environmental chamber and by implementation of a field calibration procedure we ensured that COCAP delivers accurate measurements of CO₂ dry air mole fraction even under the fast changing environmental conditions encountered on a UAS during flight. We verified this robustness against external influences in various tests. If high-frequency noise is filtered out, a maximum CO₂ dry air mole fraction error of $1.2 \mu\text{mol} \cdot \text{mol}^{-1}$ in comparison to reference instruments was found, making COCAP suitable for a wide range of environmental studies.

COCAP is a self-contained package without any dependency on the carrier system, which makes deployment on various platforms simply a matter of physical mounting. The built-in GPS module not only provides position data, but also accurate time stamps, which facilitates integration of COCAP's data with other data streams.

Since the design of COCAP, newer versions of SenseAir's HPP sensor family have become available. They exhibit lower drift and lower noise at a slightly smaller form factor (Arzoumanian et al., 2016). The integration of these newer sensors into COCAP would be straightforward and is expected to further improve the accuracy of the x_{CO_2} measurements.

The technological approaches presented in this thesis are applicable to other measurement systems as well. Many sensors benefit from a stable temperature and we have shown how an effective temperature stabilisation can be achieved within the mass, size and power restrictions of a small UAS. Likewise, the presented method for obtaining a calibration curve can be applied to other gas sensors. Regular calibrations are important to ensure the accuracy of trace gas measurements and we have given an example how to implement them in a practicable way.

Flying a CO₂ analyser on small UASs opens up new possibilities in studying the carbon cycle. As a first application we have constrained the nocturnal carbon dioxide emissions of an ecosystem using the NBL budget method. The NBL budgets were calculated from a series of x_{CO_2} profiles measured by COCAP on board an unmanned aircraft during the course of two nights. Given the moderate cost of UASs and their minimal infrastructure requirements this innovation makes the NBL budget method for

5 Conclusions and outlook

the quantification of surface fluxes more accessible. The fluxes we obtained in our pilot study are plausible and insensitive to experimental uncertainties.

While we carried out our measurements with a multicopter, fixed-wing aircraft would also be capable platforms for NBL studies. The vortices generated by their wings are slower and spread out wider than the concentrated downwash produced by the rotors of a multicopter. Therefore they should cause less interference with the NBL soundings and could provide accurate measurements down to ground level. Additionally, their typically higher horizontal speed makes it easier to evade any disturbance that they create.

Another possibility to reduce the disturbance of measurements near the ground would be a different placement of the inlet. Given the asymmetric flow pattern below and above a multicopter's rotors (see Section 4.3.1), sampling from several rotor diameters above the UAS should reduce the artefacts caused by closed flow loops. However, even in the non-optimised setup the air displacement by the multicopter changed the NBL budgets by no more than 10 %.

Future NBL studies could employ multiple UASs simultaneously to quantify spatial heterogeneity and horizontal gradients in the CO₂ dry air mole fraction. Firstly, this supports the analysis of the uncertainty of the NBL-derived fluxes. Secondly, concurrent profiles could yield constraints for the net advection of CO₂. A similar approach could be used to estimate CO₂ emissions of cities, ideally by simultaneously deploying multiple UASs at different downwind locations. Furthermore, the strength of point sources like power plants or factories could be estimated by applying a mass balance technique as is commonly used in aircraft-based studies (Conley et al., 2017 and references therein). The main advantages of small UAS over manned aircraft in these applications is their full vertical coverage from the ground to several hundred meters height and their much lower acquisition and operating cost. As small unmanned aircraft are typically limited to a range between 1 and 10 km in a single flight, they are best suited for studying processes on the small end mesoscale and below. Their low air speed and high manoeuvrability enables them to sample the atmosphere with high spatial resolution. Equipped with an analyser for carbon dioxide, UASs could also become powerful validation tools for models of tracer dispersion on fine scales, e.g. inside street canyons. Small and lightweight sensors for other tracers such as methane would open up even more possibilities. Alternatively, compact time-resolved sampling systems (Andersen et al., 2018) or long flexible tubing (Broisy et al., 2017) can be used in connection with conventional ground-based instrumentation to measure a whole range of species.

Due to their unique capabilities and low cost, we foresee that the use of unmanned aircraft in the Earth sciences will significantly increase in the near future. We have shown how accurate measurements of the CO₂ dry air mole fraction can be taken on

board small UAS and we anticipate these platforms to play an important role in closing gaps in the observation of the carbon cycle.

Bibliography

- Acevedo, O. C., Moraes, O. L. L., Da Silva, R., Fitzjarrald, D. R., Sakai, R. K., Staebler, R. M., and Czikowsky, M. J.: Inferring Nocturnal Surface Fluxes from Vertical Profiles of Scalars in an Amazon Pasture, *Global Change Biology*, 10, 886–894, doi:10.1111/j.1529-8817.2003.00755.x, 2004.
- Allan, D. W.: Should the Classical Variance Be Used as a Basic Measure in Standards Metrology?, *IEEE Transactions on Instrumentation and Measurement*, IM-36, 646–654, doi:10.1109/TIM.1987.6312761, 1987.
- Andersen, T., Scheeren, B., Peters, W., and Chen, H.: A UAV-Based Active AirCore System for Measurements of Greenhouse Gases, *Atmospheric Measurement Techniques*, 11, 2683–2699, doi:10.5194/amt-11-2683-2018, 2018.
- Arzoumanian, E., Bastos, A., Gaynullin, B., Martin, H., Hjern, L., Laurent, O., and Vogel, F. R.: An Evaluation of Commercial NDIR Sensors for a Potential Use in Future Urban GHG Monitoring Systems, URL <https://agu.confex.com/agu/fm16/meetingapp.cgi/Paper/141542>, abstract B33H-0705 presented at 2016 Fall Meeting, AGU, San Francisco, Calif., 12-16 Dec, accessed March 2017, 2016.
- Aubinet, M.: Eddy Covariance CO₂ Flux Measurements in Nocturnal Conditions: An Analysis of the Problem, *Ecological Applications*, 18, 1368–1378, URL <http://www.jstor.org/stable/40062261>, 2008.
- Aubinet, M., Feigenwinter, C., Heinesch, B., Bernhofer, C., Canepa, E., Lindroth, A., Montagnani, L., Rebmann, C., Sedlak, P., and Van Gorsel, E.: Direct Advection Measurements Do Not Help to Solve the Night-Time CO₂ Closure Problem: Evidence from Three Different Forests, *Agricultural and Forest Meteorology*, 150, 655–664, doi:10.1016/j.agrformet.2010.01.016, 2010.
- Baldocchi, D. D.: Assessing the Eddy Covariance Technique for Evaluating Carbon Dioxide Exchange Rates of Ecosystems: Past, Present and Future, *Global Change Biology*, 9, 479–492, doi:10.1046/j.1365-2486.2003.00629.x, 2003.
- Berman, E. S. F., Fladeland, M., Liem, J., Kolyer, R., and Gupta, M.: Greenhouse Gas Analyzer for Measurements of Carbon Dioxide, Methane, and Water Vapor Aboard

Bibliography

- an Unmanned Aerial Vehicle, *Sensors and Actuators B: Chemical*, 169, 128–135, doi:10.1016/j.snb.2012.04.036, 2012.
- Brady, J. M., Stokes, M. D., Bonnardel, J., and Bertram, T. H.: Characterization of a Quadrotor Unmanned Aircraft System for Aerosol-Particle-Concentration Measurements, *Environmental Science & Technology*, 50, 1376–1383, doi:10.1021/acs.est.5b05320, 2016.
- Brewer, C. A.: ColorBrewer: Color Advice for Maps, URL <http://colorbrewer2.org>, 2017.
- Briffa, K. R., Jones, P. D., Schweingruber, F. H., and Osborn, T. J.: Influence of Volcanic Eruptions on Northern Hemisphere Summer Temperature over the Past 600 Years, *Nature*, 393, 450–455, doi:10.1038/30943, 1998.
- Brosy, C., Krampf, K., Zeeman, M., Wolf, B., Junkermann, W., Schäfer, K., Emeis, S., and Kunstmann, H.: Simultaneous Multicopter-Based Air Sampling and Sensing of Meteorological Variables, *Atmos. Meas. Tech.*, 10, 2773–2784, doi:10.5194/amt-10-2773-2017, 2017.
- Campioli, M., Malhi, Y., Vicca, S., Luysaert, S., Papale, D., Peñuelas, J., Reichstein, M., Migliavacca, M., Arain, M. A., and Janssens, I. A.: Evaluating the Convergence between Eddy-Covariance and Biometric Methods for Assessing Carbon Budgets of Forests, *Nature Communications*, 7, ncomms13717, doi:10.1038/ncomms13717, 2016.
- Chandrasekhar, R.: How to Write a Thesis: A Working Guide, URL http://www.student.uwa.edu.au/__data/assets/pdf_file/0007/1919239/How-to-write-a-thesis-A-working-guide.pdf, 2008.
- Chen, B., Black, T. A., Coops, N. C., Hilker, T., (Tony) Trofymow, J. A., and Morgenstern, K.: Assessing Tower Flux Footprint Climatology and Scaling Between Remotely Sensed and Eddy Covariance Measurements, *Boundary-Layer Meteorology*, 130, 137–167, doi:10.1007/s10546-008-9339-1, 2009.
- Chen, H., Fan, M., Kuzyakov, Y., Billen, N., and Stahr, K.: Comparison of Net Ecosystem CO₂ Exchange in Cropland and Grassland with an Automated Closed Chamber System, *Nutrient Cycling in Agroecosystems*, 98, 113–124, doi:10.1007/s10705-014-9600-6, 2014.
- Choularton, T. W., Gallagher, M. W., Bower, K. N., Fowler, D., Zahniser, M., and Kaye, A.: Trace Gas Flux Measurements at the Landscape Scale Using Boundary-Layer Budgets, *Philosophical Transactions of the Royal Society of London A: Mathematical, Physical and Engineering Sciences*, 351, 357–369, doi:10.1098/rsta.1995.0039, 1995.

- Ciais, P., Rayner, P., Chevallier, F., Bousquet, P., Logan, M., Peylin, P., and Ramonet, M.: Atmospheric Inversions for Estimating CO₂ Fluxes: Methods and Perspectives, *Climatic Change*, 103, 69–92, doi:10.1007/s10584-010-9909-3, 2010.
- Ciais, P., Sabine, C., Bala, G., Bopp, L., Brovkin, V., Canadell, J., Chhabra, A., DeFries, R., Galloway, J., Heimann, M., Jones, C., Le Quéré, C., Myneni, R., Piao, S., and Thornton, P.: Carbon and Other Biogeochemical Cycles, in: *ClimateChange 2013: The Physical Science Basis. Contribution of Working Group I to the Fifth Assessment Report of the Intergovernmental Panel on Climate Change*, edited by Stocker, T., Qin, D., Plattner, G.-K., Tignor, M., Allen, S., Boschung, J., Nauels, A., Xia, Y., Bex, V., and Midgley, P., Cambridge University Press, Cambridge, United Kingdom and New York, NY, USA, URL http://ipcc.ch/pdf/assessment-report/ar5/wg1/WG1AR5_Chapter06_FINAL.pdf, 2013.
- Clapeyron, B. P. E.: Mémoire sur la puissance motrice de la chaleur, *Journal de l'École Polytechnique*, XIV, 153–190, 1834.
- Collins, M., Knutti, R., Arblaster, J., Dufresne, J.-L., Fichet, T., Friedlingstein, P., Gao, X., Gutowski, W., Johns, T., Krinner, G., Shongwe, M., Tebaldi, C., Weaver, A., and Wehner, M.: Long-Term Climate Change: Projections, Commitments and Irreversibility, in: *Climate Change 2013: The Physical Science Basis. Contribution of Working Group I to the Fifth Assessment Report of the Intergovernmental Panel on Climate Change*, edited by Stocker, T., Qin, D., Plattner, G.-K., Tignor, M., Allen, S., Boschung, J., Nauels, A., Xia, Y., Bex, V., and Midgley, P., Cambridge University Press, Cambridge, United Kingdom and New York, NY, USA, URL http://ipcc.ch/pdf/assessment-report/ar5/wg1/WG1AR5_Chapter12_FINAL.pdf, 2013.
- Conley, S., Faloon, I., Mehrotra, S., Suard, M., Lenschow, D. H., Sweeney, C., Herndon, S., Schwietzke, S., Pétron, G., Pifer, J., Kort, E. A., and Schnell, R.: Application of Gauss's Theorem to Quantify Localized Surface Emissions from Airborne Measurements of Wind and Trace Gases, *Atmos. Meas. Tech.*, 10, 3345–3358, doi:10.5194/amt-10-3345-2017, 2017.
- Culf, A. D., Fisch, G., Malhi, Y., and Nobre, C. A.: The Influence of the Atmospheric Boundary Layer on Carbon Dioxide Concentrations over a Tropical Forest, *Agricultural and Forest Meteorology*, 85, 149–158, doi:10.1016/S0168-1923(96)02412-4, 1997.
- Culf, A. D., Fisch, G., Malhi, Y., Carvalho Costa, R., Nobre, A. D., de O. Marques Filho, A., Gash, J. H. C., and Grace, J.: Carbon Dioxide Measurements in the Nocturnal Boundary Layer over Amazonian Forest, *Hydrol. Earth Syst. Sci.*, 3, 39–53, doi:10.5194/hess-3-39-1999, 1999.

Bibliography

- Denmead, O., Raupach, M., Dunin, F., Cleugh, H., and Leuning, R.: Boundary Layer Budgets for Regional Estimates of Scalar Fluxes, *Global Change Biology*, 2, 255–264, doi:10.1111/j.1365-2486.1996.tb00077.x, 1996.
- Eaton, J. W., Bateman, D., Hauberg, S., and Wehbring, R.: GNU Octave Version 4.2.1 Manual: A High-Level Interactive Language for Numerical Computations, URL <https://www.gnu.org/software/octave/doc/v4.2.1/>, 2017.
- EEA: CLC 2012 — Copernicus Land Monitoring Service, URL <http://land.copernicus.eu/pan-european/corine-land-cover/clc-2012>, 2016.
- Egger, J., Bajrachaya, S., Heinrich, R., Kolb, P., Lämmlein, S., Mech, M., Reuder, J., Schäper, W., Shakya, P., Schween, J., and Wendt, H.: Diurnal Winds in the Himalayan Kali Gandaki Valley. Part III: Remotely Piloted Aircraft Soundings, *Monthly Weather Review*, 130, 2042–2058, doi:10.1175/1520-0493(2002)130<2042%3ADWITHK>2.0.CO%3B2, 2002.
- Fan, S., Gloor, M., Mahlman, J., Pacala, S., Sarmiento, J., Takahashi, T., and Tans, P.: A Large Terrestrial Carbon Sink in North America Implied by Atmospheric and Oceanic Carbon Dioxide Data and Models, *Science*, 282, 442–446, doi:10.1126/science.282.5388.442, 1998.
- Foken, T., Aubinet, M., and Leuning, R.: The Eddy Covariance Method, in: *Eddy Covariance*, Springer Atmospheric Sciences, pp. 1–19, Springer, Dordrecht, URL https://link.springer.com/chapter/10.1007/978-94-007-2351-1_1, 2012.
- Gerbig, C., Lin, J. C., Wofsy, S. C., Daube, B. C., Andrews, A. E., Stephens, B. B., Bakwin, P. S., and Grainger, C. A.: Toward Constraining Regional-Scale Fluxes of CO₂ with Atmospheric Observations over a Continent: 2. Analysis of COBRA Data Using a Receptor-Oriented Framework, *Journal of Geophysical Research: Atmospheres*, 108, 4757, doi:10.1029/2003JD003770, 2003.
- Gilmanov, T. G., Soussana, J. F., Aires, L., Allard, V., Ammann, C., Balzarolo, M., Barcza, Z., Bernhofer, C., Campbell, C. L., Cernusca, A., Cescatti, A., Clifton-Brown, J., Dirks, B. O. M., Dore, S., Eugster, W., Fuhrer, J., Gimeno, C., Gruenwald, T., Haszpra, L., Hensen, A., Ibrom, A., Jacobs, A. F. G., Jones, M. B., Lanigan, G., Laurila, T., Lohila, A., G. Manca, Marcolla, B., Nagy, Z., Pilegaard, K., Pinter, K., Pio, C., Raschi, A., Rogiers, N., Sanz, M. J., Stefani, P., Sutton, M., Tuba, Z., Valentini, R., Williams, M. L., and Wohlfahrt, G.: Partitioning European Grassland Net Ecosystem CO₂ Exchange into Gross Primary Productivity and Ecosystem Respiration Using Light Response Function Analysis, *Agriculture, Ecosystems & Environment*, 121, 93–120, doi:10.1016/j.agee.2006.12.008, 2007.

- Goulden, M. L., Munger, J. W., Fan, S.-M., Daube, B. C., and Wofsy, S. C.: Measurements of Carbon Sequestration by Long-Term Eddy Covariance: Methods and a Critical Evaluation of Accuracy, *Global Change Biology*, 2, 169–182, doi:10.1111/j.1365-2486.1996.tb00070.x, 1996.
- Gu, L., Falge, E. M., Boden, T., Baldocchi, D. D., Black, T. A., Saleska, S. R., Suni, T., Verma, S. B., Vesala, T., Wofsy, S. C., and Xu, L.: Objective Threshold Determination for Nighttime Eddy Flux Filtering, *Agricultural and Forest Meteorology*, 128, 179–197, doi:10.1016/j.agrformet.2004.11.006, 2005.
- Hartmann, D., Klein Tank, A., Rusticucci, M., Alexander, L., Brönnimann, S., Charabi, Y., Dentener, F., Dlugokencky, E., Easterling, D., Kaplan, A., Soden, B., Thorne, P., Wild, M., and Zhai, P.: Observations: Atmosphere and Surface, in: *Climate Change 2013: The Physical Science Basis. Contribution of Working Group I to the Fifth Assessment Report of the Intergovernmental Panel on Climate Change*, edited by Stocker, T., Qin, D., Plattner, G.-K., Tignor, M., Allen, S., Boschung, J., Nauels, A., Xia, Y., Bex, V., and Midgley, P., Cambridge University Press, Cambridge, United Kingdom and New York, NY, USA, URL http://ipcc.ch/pdf/assessment-report/ar5/wg1/WG1AR5_Chapter02_FINAL.pdf, 2013.
- Hayek, M. N., Wehr, R., Longo, M., Hutyra, L. R., Wiedemann, K., Munger, J. W., Bonal, D., Saleska, S. R., Fitzjarrald, D. R., and Wofsy, S. C.: A Novel Correction for Biases in Forest Eddy Covariance Carbon Balance, *Agricultural and Forest Meteorology*, 250-251, 90–101, doi:10.1016/j.agrformet.2017.12.186, 2018.
- Hummelgård, C., Bryntse, I., Bryzgalov, M., Henning, J.-A., Martin, H., Norén, M., and Rödjegård, H.: Low-Cost NDIR Based Sensor Platform for Sub-Ppm Gas Detection, *Urban Climate*, 14, Part 3, 342–350, doi:10.1016/j.uclim.2014.09.001, 2015.
- ICAO: Manual of the ICAO Standard Atmosphere: extended to 80 kilometres (262 500 feet), Third Edition, 1993.
- ICAO: Global Air Traffic Management Operational Concept, URL [https://www.icao.int/Meetings/anconf12/Document%20Archive/9854_cons_en\[1\].pdf](https://www.icao.int/Meetings/anconf12/Document%20Archive/9854_cons_en[1].pdf), 2005.
- International Bureau of Weights and Measures: The International System of Units (SI), STEDI MEDIA, Paris, 8th edn., URL <https://www.bipm.org/en/publications/si-brochure/>, 2006.
- IPCC: Summary for Policymakers, in: *Climate Change 2013: The Physical Science Basis. Contribution of Working Group I to the Fifth Assessment Report of the Intergovernmental Panel on Climate Change*, edited by Stocker, T., Qin, D., Plattner, G.-K.,

Bibliography

- Tignor, M., Allen, S., Boschung, J., Nauels, A., Xia, Y., Bex, V., and Midgley, P., Cambridge University Press, Cambridge, United Kingdom and New York, NY, USA, URL http://ipcc.ch/pdf/assessment-report/ar5/wg1/WG1AR5_SPM_FINAL.pdf, 2013.
- IPCC: Summary for Policymakers, in: *Climate Change 2014: Impacts, Adaptation, and Vulnerability. Part A: Global and Sectoral Aspects. Contribution of Working Group II to the Fifth Assessment Report of the Intergovernmental Panel on Climate Change*, edited by Field, C., Barros, V., Dokken, D., Mach, K., Mastrandrea, M., Bilir, T., Chatterjee, M., Ebi, K., Estrada, Y., Genova, R., Girma, B., Kissel, E., Levy, A., MacCracken, S., Mastrandrea, P., and White, L., Cambridge University Press, Cambridge, United Kingdom and New York, NY, USA, URL http://ipcc.ch/pdf/assessment-report/ar5/wg2/ar5_wgII_spm_en.pdf, 2014.
- Jeschag, W.: Untersuchung und Evaluation eines Echtzeitbetriebssystems für einen Datenlogger für atmosphärische Messungen auf unbemannten Fluggeräten, Master's thesis, Ernst-Abbe-Fachhochschule, Jena, URL <http://hdl.handle.net/11858/00-001M-0000-0026-AF63-9>, 2014.
- Joos, F. and Spahni, R.: Rates of Change in Natural and Anthropogenic Radiative Forcing over the Past 20,000 Years, *Proceedings of the National Academy of Sciences*, 105, 1425–1430, doi:10.1073/pnas.0707386105, 2008.
- Jung, M., Reichstein, M., and Bondeau, A.: Towards Global Empirical Upscaling of FLUXNET Eddy Covariance Observations: Validation of a Model Tree Ensemble Approach Using a Biosphere Model, *Biogeosciences*, 6, 2001–2013, doi:10.5194/bg-6-2001-2009, 2009.
- Khan, A., Schaefer, D., Tao, L., Miller, D. J., Sun, K., Zondlo, M. A., Harrison, W. A., Roscoe, B., and Lary, D. J.: Low Power Greenhouse Gas Sensors for Unmanned Aerial Vehicles, *Remote Sensing*, 4, 1355–1368, doi:10.3390/rs4051355, 2012.
- Kirtman, B., Power, S., Adedoyin, J., Boer, G., Bojariu, R., Camilloni, I., Doblas-Reyes, F., Fiore, A., Kimoto, M., Meehl, G., Prather, M., Sarr, A., Schär, C., Sutton, R., van Oldenborgh, G., Vecchi, G., and Wang, H.: Near-Term Climate Change: Projections and Predictability, in: *Climate Change 2013: The Physical Science Basis. Contribution of Working Group I to the Fifth Assessment Report of the Intergovernmental Panel on Climate Change*, edited by Stocker, T., Qin, D., Plattner, G.-K., Tignor, M., Allen, S., Boschung, J., Nauels, A., Xia, Y., Bex, V., and Midgley, P., Cambridge University Press, Cambridge, United Kingdom and New York, NY, USA, URL http://ipcc.ch/pdf/assessment-report/ar5/wg1/WG1AR5_Chapter11_FINAL.pdf, 2013.

- Knorr, W.: Annual and Interannual CO₂ Exchanges of the Terrestrial Biosphere: Process-based Simulations and Uncertainties, *Global Ecology and Biogeography*, 9, 225–252, doi:10.1046/j.1365-2699.2000.00159.x, 2000.
- Kopp, G. and Lean, J. L.: A New, Lower Value of Total Solar Irradiance: Evidence and Climate Significance, *Geophysical Research Letters*, 38, doi:10.1029/2010GL045777, 2011.
- Kovesi, P.: Good Colour Maps: How to Design Them, arXiv:1509.03700 [cs], URL <http://arxiv.org/abs/1509.03700>, 2015.
- Kutsch, W. L., Kolle, O., Rebmann, C., Knohl, A., Ziegler, W., and Schulze, E.-D.: Advection and Resulting CO₂ Exchange Uncertainty in a Tall Forest in Central Germany, *Ecological Applications*, 18, 1391–1405, URL <http://www.jstor.org/stable/40062263>, 2008.
- Laurent, O.: ICOS Atmospheric Station Specifications V1.2, URL <https://icos-atc.lsce.ipsl.fr/filebrowser/download/27251>, accessed April 2017, 2016.
- Leuning, R.: Measurements of Trace Gas Fluxes in the Atmosphere Using Eddy Covariance: WPL Corrections Revisited, in: *Handbook of Micrometeorology, Atmospheric and Oceanographic Sciences Library*, pp. 119–132, Springer, Dordrecht, doi:10.1007/1-4020-2265-4_6, URL https://link.springer.com/chapter/10.1007/1-4020-2265-4_6, 2004.
- Lin, J. C., Gerbig, C., Wofsy, S. C., Andrews, A. E., Daube, B. C., Davis, K. J., and Grainger, C. A.: A Near-Field Tool for Simulating the Upstream Influence of Atmospheric Observations: The Stochastic Time-Inverted Lagrangian Transport (STILT) Model, *Journal of Geophysical Research: Atmospheres*, 108, 4493, doi:10.1029/2002JD003161, 2003.
- Longdoz, B., Gross, P., and Granier, A.: Multiple Quality Tests for Analysing CO₂ Fluxes in a Beech Temperate Forest, *Biogeosciences*, 5, 719–729, doi:10.5194/bg-5-719-2008, 2008.
- Martin, C. R., Zeng, N., Karion, A., Dickerson, R. R., Ren, X., Turpie, B. N., and Weber, K. J.: Evaluation and Environmental Correction of Ambient CO₂ Measurements from a Low-Cost NDIR Sensor, *Atmos. Meas. Tech.*, 10, 2383–2395, doi:10.5194/amt-10-2383-2017, 2017.
- Masarie, K. A. and Tans, P. P.: Extension and Integration of Atmospheric Carbon Dioxide Data into a Globally Consistent Measurement Record, *Journal of Geophysical Research: Atmospheres*, 100, 11 593–11 610, doi:10.1029/95JD00859, 1995.

Bibliography

- Mayer, S., Hattenberger, G., Brisset, P., Jonassen, M. O., and Reuder, J.: A 'No-Flow-Sensor' Wind Estimation Algorithm for Unmanned Aerial Systems, *International Journal of Micro Air Vehicles*, pp. 15–29, doi:10.1260/1756-8293.4.1.15, 2012.
- McClatchey, R. A., Benedict, W. S., Clough, S. A., Burch, D., Calfee, R., Fox, K., Rothman, L., and Garing, J.: AFCRL Atmospheric Absorption Line Parameters Compilation, URL <http://hitran.org/media/refs/HITRAN-1973.pdf>, 1973.
- Miloshevich, L. M., Paukkunen, A., Vömel, H., and Oltmans, S. J.: Development and Validation of a Time-Lag Correction for Vaisala Radiosonde Humidity Measurements, *Journal of Atmospheric and Oceanic Technology*, 21, 1305–1327, doi:10.1175/1520-0426(2004)021<1305:DAVOAT>2.0.CO;2, 2004.
- Myhre, G., Shindell, D., Bréon, F.-M., Collins, W., Fuglestedt, J., Huang, J., Koch, D., Lamarque, J.-F., Lee, D., Mendoza, B., Nakajima, T., Robock, A., Stephens, G., Takemura, T., and Zhang, H.: Anthropogenic and Natural Radiative Forcing, in: *Climate Change 2013: The Physical Science Basis. Contribution of Working Group I to the Fifth Assessment Report of the Intergovernmental Panel on Climate Change*, edited by Stocker, T., Qin, D., Plattner, G.-K., Tignor, M., Allen, S., Boschung, J., Nauels, A., Xia, Y., Bex, V., and Midgley, P., Cambridge University Press, Cambridge, United Kingdom and New York, NY, USA, URL http://ipcc.ch/pdf/assessment-report/ar5/wg1/WG1AR5_Chapter08_FINAL.pdf, 2013.
- Neumann, P. P. and Bartholmai, M.: Real-Time Wind Estimation on a Micro Unmanned Aerial Vehicle Using Its Inertial Measurement Unit, Sensors and Actuators A: Physical, 235, 300–310, doi:10.1016/j.sna.2015.09.036, 2015.
- O'Keefe, A. and Deacon, D. A. G.: Cavity Ring-down Optical Spectrometer for Absorption Measurements Using Pulsed Laser Sources, *Review of Scientific Instruments*, 59, 2544–2551, doi:10.1063/1.1139895, 1988.
- Oppenheimer, C.: Climatic, Environmental and Human Consequences of the Largest Known Historic Eruption: Tambora Volcano (Indonesia) 1815, *Progress in Physical Geography: Earth and Environment*, 27, 230–259, doi:10.1191/0309133303pp379ra, 2003.
- Orlanski, I.: A Rational Subdivision of Scales for Atmospheric Processes, *Bulletin of the American Meteorological Society*, 56, 527–530, 1975.
- Pattey, E., Strachan, I. B., Desjardins, R. L., and Massheder, J.: Measuring Nighttime CO₂ Flux over Terrestrial Ecosystems Using Eddy Covariance and Nocturnal Boundary Layer Methods, *Agricultural and Forest Meteorology*, 113, 145–158, doi:10.1016/S0168-1923(02)00106-5, 2002.

- Peel, M. C., Finlayson, B. L., and McMahon, T. A.: Updated World Map of the Köppen-Geiger Climate Classification, *Hydrol. Earth Syst. Sci.*, 11, 1633–1644, doi:10.5194/hess-11-1633-2007, 2007.
- Pétron, G., Frost, G., Miller, B. R., Hirsch, A. I., Montzka, S. A., Karion, A., Trainer, M., Sweeney, C., Andrews, A. E., Miller, L., Kofler, J., Bar-Ilan, A., Dlugokencky, E. J., Patrick, L., Moore, C. T., Ryerson, T. B., Siso, C., Kolodzey, W., Lang, P. M., Conway, T., Novelli, P., Masarie, K., Hall, B., Guenther, D., Kitzis, D., Miller, J., Welsh, D., Wolfe, D., Neff, W., and Tans, P.: Hydrocarbon Emissions Characterization in the Colorado Front Range: A Pilot Study, *Journal of Geophysical Research: Atmospheres*, 117, D04 304, doi:10.1029/2011JD016360, 2012.
- Piedrahita, R., Xiang, Y., Masson, N., Ortega, J., Collier, A., Jiang, Y., Li, K., Dick, R. P., Lv, Q., Hannigan, M., and Shang, L.: The next Generation of Low-Cost Personal Air Quality Sensors for Quantitative Exposure Monitoring, *Atmos. Meas. Tech.*, 7, 3325–3336, doi:10.5194/amt-7-3325-2014, 2014.
- Reuder, J., Brisset, P., Jonassen, M., Müller, M., and Mayer, S.: SUMO: A Small Unmanned Meteorological Observer for Atmospheric Boundary Layer Research, *IOP Conference Series: Earth and Environmental Science*, 1, 012 014, doi:10.1088/1755-1315/1/1/012014, 2008.
- Savitzky, A. and Golay, M. J. E.: Smoothing and Differentiation of Data by Simplified Least Squares Procedures., *Analytical Chemistry*, 36, 1627–1639, doi:10.1021/ac60214a047, 1964.
- SCHOTT: Interference Filters & Special Filters, URL http://www.schott.com/d/advanced_optics/bffb1c3f-04d2-49fb-85b9-cdb6245e3d47/1.0/schott-interference-filters-and-special-filters-description-2015-eng.pdf, accessed January 2018, 2015.
- Shusterman, A. A., Teige, V. E., Turner, A. J., Newman, C., Kim, J., and Cohen, R. C.: The BERkeley Atmospheric CO₂ Observation Network: Initial Evaluation, *Atmos. Chem. Phys.*, 16, 13 449–13 463, doi:10.5194/acp-16-13449-2016, 2016.
- Siebicke, L., Hunner, M., and Foken, T.: Aspects of CO₂ Advection Measurements, *Theoretical and Applied Climatology*, 109, 109–131, doi:10.1007/s00704-011-0552-3, 2012.
- Spiess, T., Bange, J., Buschmann, M., and Vörsmann, P.: First Application of the Meteorological Mini-UAV 'M2AV', *Meteorologische Zeitschrift*, pp. 159–169, doi:10.1127/0941-2948/2007/0195, 2007.

Bibliography

- Statistisches Bundesamt (Destatis): Daten Aus Dem Gemeindeverzeichnis Kreisfreie Städte Und Landkreise Nach Fläche, Bevölkerung Und Bevölkerungsdichte, Gebietsstand 31.12.2017, URL https://www.destatis.de/DE/ZahlenFakten/LaenderRegionen/Regionales/Gemeindeverzeichnis/Administrativ/Aktuell/04Kreise.xlsx?__blob=publicationFile, 2018.
- Stein, A. F., Draxler, R. R., Rolph, G. D., Stunder, B. J. B., Cohen, M. D., and Ngan, F.: NOAA's HYSPLIT Atmospheric Transport and Dispersion Modeling System, *Bulletin of the American Meteorological Society*, 96, 2059–2077, doi:10.1175/BAMS-D-14-00110.1, 2015.
- Stull, R.: *An Introduction to Boundary Layer Meteorology*, Kluwer Academic Publishers, Dordrecht, 1988.
- Tohjima, Y., Katsumata, K., Morino, I., Mukai, H., Machida, T., Akama, I., Amari, T., and Tsunogai, U.: Theoretical and Experimental Evaluation of the Isotope Effect of NDIR Analyzer on Atmospheric CO₂ Measurement, *Journal of Geophysical Research: Atmospheres*, 114, D13 302, doi:10.1029/2009JD011734, 2009.
- Watai, T., Machida, T., Ishizaki, N., and Inoue, G.: A Lightweight Observation System for Atmospheric Carbon Dioxide Concentration Using a Small Unmanned Aerial Vehicle, *Journal of Atmospheric and Oceanic Technology*, 23, 700–710, doi:10.1175/JTECH1866.1, 2006.
- White, J. U.: Long Optical Paths of Large Aperture, *JOSA*, 32, 285–288, doi:10.1364/JOSA.32.000285, 1942.
- Wikipedia contributors: Wikipedia:Graphics Lab/Resources/QGIS/Create a Topographic Background, Wikipedia, URL https://en.wikipedia.org/w/index.php?title=Wikipedia:Graphics_Lab/Resources/QGIS/Create_a_topographic_background&oldid=526059852, 2012.
- Wilcox, R.: *Introduction to Robust Estimation and Hypothesis Testing*, Statistical Modeling and Decision Science, Academic Press, Boston, doi:10.1016/B978-0-12-386983-8.00003-2, URL <http://www.sciencedirect.com/science/book/9780123869838>, 2012.
- Wilson, K. B. and Baldocchi, D. D.: Comparing Independent Estimates of Carbon Dioxide Exchange over 5 Years at a Deciduous Forest in the Southeastern United States, *Journal of Geophysical Research: Atmospheres*, 106, 34 167–34 178, doi:10.1029/2001JD000624, 2001.

- Wilson, P.: *The Circuit Designer's Companion*, 3rd Edition, Newnes, Oxford, United Kingdom and Waltham, MA, USA, 3 edn., URL <http://proquest.tech.safaribooksonline.de/book/electrical-engineering/9780080971384>, 2011.
- Winderlich, J., Gerbig, C., Kolle, O., and Heimann, M.: Inferences from CO₂ and CH₄ Concentration Profiles at the Zotino Tall Tower Observatory (ZOTTO) on Regional Summertime Ecosystem Fluxes, *Biogeosciences*, 11, 2055–2068, doi:10.5194/bg-11-2055-2014, 2014.
- WMO: GLOBAL ATMOSPHERE WATCH MEASUREMENTS GUIDE, URL https://library.wmo.int/pmb_ged/wmo-td_1073.pdf, accessed November 2018, 2001.
- WMO: 18th WMO/IAEA Meeting on Carbon Dioxide, Other Greenhouse Gases and Related Tracers Measurement Techniques (GGMT-2015), URL https://library.wmo.int/opac/doc_num.php?explnum_id=3074, accessed May 2017, 2016.
- Wohlfahrt, G. and Galvagno, M.: Revisiting the Choice of the Driving Temperature for Eddy Covariance CO₂ Flux Partitioning, *Agricultural and Forest Meteorology*, 237–238, 135–142, doi:10.1016/j.agrformet.2017.02.012, 2017.
- Wohlfahrt, G., Anfang, C., Bahn, M., Haslwanter, A., Newesely, C., Schmitt, M., Drösler, M., Pfadenhauer, J., and Cernusca, A.: Quantifying Nighttime Ecosystem Respiration of a Meadow Using Eddy Covariance, Chambers and Modelling, *Agricultural and Forest Meteorology*, 128, 141–162, doi:10.1016/j.agrformet.2004.11.003, 2005.
- Wolf, B., Chwala, C., Fersch, B., Garvelmann, J., Junkermann, W., Zeeman, M. J., Angerer, A., Adler, B., Beck, C., Brosy, C., Brugger, P., Emeis, S., Dannenmann, M., De Roo, F., Diaz-Pines, E., Haas, E., Hagen, M., Hajsek, I., Jacobeit, J., and Jagdhuber, T.: THE SCALEX CAMPAIGN: Scale-Crossing Land Surface and Boundary Layer Processes in the TERENO- preAlpine Observatory, *Bulletin of the American Meteorological Society*, 98, 1217–1234, doi:10.1175/BAMS-D-15-00277.1, 2017.
- Yasuda, T., Yonemura, S., and Tani, A.: Comparison of the Characteristics of Small Commercial NDIR CO₂ Sensor Models and Development of a Portable CO₂ Measurement Device, *Sensors*, 12, 3641–3655, doi:10.3390/s120303641, 2012.
- Zeeman, M. J., Mauder, M., Steinbrecher, R., Heidbach, K., Eckart, E., and Schmid, H. P.: Reduced Snow Cover Affects Productivity of Upland Temperate Grasslands, *Agricultural and Forest Meteorology*, 232, 514–526, doi:10.1016/j.agrformet.2016.09.002, 2017.

Selbstständigkeitserklärung

Ich erkläre, dass ich die vorliegende Arbeit selbstständig und unter Verwendung der angegebenen Hilfsmittel, persönlichen Mitteilungen und Quellen angefertigt habe.

Ort, Datum

Unterschrift des Verfassers